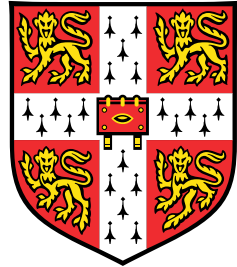


Swimming at low Reynolds number

slip boundaries and interacting filaments



Yi Man

Department of Applied Mathematics and Theoretical Physics
University of Cambridge

This dissertation is submitted for the degree of
Doctor of Philosophy

Trinity College

May 2017

Declaration

I hereby declare that except where specific reference is made to the work of others, the contents of this dissertation are original and have not been submitted in whole or in part for consideration for any other degree or qualification in this, or any other university. This dissertation is my own work and contains nothing which is the outcome of work done in collaboration with others, except as specified in the text and Acknowledgements.

Yi Man
May 2017

Acknowledgements

I would like to express my sincere gratitude to my supervisor Prof. Eric Lauga for the continuous support of my Ph.D study and research in the past six years, for his passion, patience, motivation, and immense knowledge. I could not have imagined having a better supervisor and mentor in my life. I would like to also thank all my friends in team Lauga for stimulating discussions and all the fun we have had together during my Ph.D. I would like to thank Cambridge Overseas Trust to provide scholarship to support me finish my study. Last but not the least, I would like to thank my parents for love and support.

Abstract

Biological microorganisms swim in different types of fluids using a range of diverse motions and are often found in complex geometries. Their study is a rich field full of outstanding problems. One aspect that has attracted a lot of attention is the role played by hydrodynamic interactions, including those between a cell and its fluid environment (fluid-cell), or between neighbouring cells (cell-cell). These interactions can affect dramatically the dynamics of these swimmers.

This dissertation investigates the dynamics of filaments interacting hydrodynamically with a fluid through slip boundary conditions or with other filaments and is composed of two separate parts. The first part of the thesis focuses on a single filament characterised by a slip boundary condition, which is a property displayed by many non-Newtonian fluids. I propose a waving sheet and a waving cylinder model to demonstrate a possible enhancement of swimming by such slip effect. The results are in good agreement with previous experimental and numerical studies. In subsequent work, I extend the classical slender-body theory to replace the no-slip boundary condition by a finite slip length.

The second part of the thesis addresses the nature of hydrodynamic interactions between filaments - a phenomenon that occurs widely in the biological world. By developing a new method for integrating hydrodynamic singularities between interacting filaments, I show how the force on the filament can be evaluated analytically. Using this result, I study the specific problem of bacterial flagellar bundling. This complex process is studied in two steps. Firstly, using a simpler geometry, I propose a model with elastic filaments to reveal the dynamics of bundling and unbundling. I then expand upon this to consider the full helical geometry of a bacterial flagellum, and develop a theoretical model for the pathway to synchronization. In each case, either by considering simple geometries or through the use of asymptotic methods, I capture in the model the main physical features and compare these to previous experimental and numerical results, thereby making important progress toward our understanding of the physics of flagellar bundling.

Table of contents

1	Introduction	1
1.1	Swimming in complex fluids: Slip boundaries	2
1.2	Hydrodynamically interacting filaments: Flagellar bundling	4
2	Phase-separation models for swimming enhancement in complex fluids	7
2.1	Swimming in a fluid with finite apparent slip length	9
2.1.1	Two dimensional waving sheet	9
2.1.2	Three-dimensional waving filament	13
2.2	Swimming in a two-fluid domain	18
2.2.1	Two dimensional waving sheet	18
2.2.2	Three dimensional waving filament	21
2.3	Discussion	25
3	Slip slender-body theory	27
3.1	Asymptotic expansion in logarithms	29
3.1.1	Set-up	29
3.1.2	Inner solution	31
3.1.3	Outer solution and matching	36
3.1.4	Force density on the body	39
3.2	Distribution of flow singularities for straight rods	40
3.2.1	Along the axis	40
3.2.2	Perpendicular to axis	43
3.3	Slender-body theory	46
3.4	Validation and comparison	50
3.4.1	Validation of slip SBT	50
3.4.2	Comparison with numerical results	51
3.5	Discussion	51

4 Hydrodynamic interactions between biological filaments	55
4.1 Long-wavelength integration	56
4.1.1 Set-up	56
4.1.2 Point moments (rotlets)	57
4.1.3 Point forces (stokeslets)	60
4.1.4 Dimensional results	62
4.2 An example of planar motion	63
4.3 Discussion	64
5 Bundling of elastic filaments from hydrodynamic interactions	67
5.1 Interactions between two elastic filaments	68
5.1.1 Set-up	68
5.1.2 Force balance	70
5.1.3 Kinematics	71
5.2 Calculation of elastic force density	71
5.2.1 Classical rod theory	71
5.2.2 Separation of time scales	72
5.2.3 Non-dimensionalisation	72
5.2.4 Twist equilibrium	73
5.2.5 Scalings	74
5.2.6 Tension	74
5.2.7 Orders of magnitude and final scalings	75
5.3 Calculation of hydrodynamic force density	76
5.3.1 Resistive-force theory	76
5.3.2 Hydrodynamic interactions	77
5.4 Long-wavelength bundling model	79
5.5 Bundling and unbundling of elastic filaments	81
5.5.1 Numerical procedure	81
5.5.2 Bundling of two filaments	82
5.5.3 N symmetric filaments	83
5.5.4 Asymmetric filaments	85
5.5.5 Unbundling	86
5.6 Crossing instability	86
5.6.1 Small Bu analysis and analytical ansatz	87
5.6.2 Two-dimensional model	89
5.6.3 Single model	90
5.7 Discussion	91

6 Synchronisation of two nearby helices	105
6.1 Hydrodynamic interactions between two helices	106
6.1.1 Set-up	106
6.1.2 Hydrodynamic force	108
6.1.3 Nondimensionalisation	108
6.2 Asymptotic analysis with small amplitude	109
6.2.1 Expand as orders of ε_b	109
6.2.2 Expand position vector	110
6.3 Expand hydrodynamic interaction term	112
6.3.1 Expand relative position vector R	112
6.3.2 Evaluate J ⁽⁰⁾	113
6.3.3 Evaluate J ⁽¹⁾	114
6.4 Evaluate torque and force	115
6.4.1 Torque	115
6.4.2 Force	117
6.5 Compare with numerics	122
6.6 Synchronisation with recovery torque	124
6.7 Discussion	125
7 Conclusion	127
References	131

Chapter 1

Introduction

Over the past few decades, problems on swimming at low Reynolds number, which is dominated by Stokes equation, have received significant attention, from both the physics and biological communities [127, 88, 108, 19, 17, 80]. As is now well known, the physics of swimming in Stokes flows is quite different from that of swimming on a human length scale. The oft-cited distinguishing property is the scallop theorem [108] which states that locomotion by a sequence of shape which is reciprocal (i.e., identical under a time-reversal symmetry) leads to zero net propulsion. So, for example, the flapping of the fins of a scuba diver does not work on small length scales. Biological organisms are able to circumvent the constraints of the theorem by deforming their bodies or appendages (flagella) in a wave-like fashion breaking the time-reversibility requirement [82, 78].

Theoretical studies on low Reynolds number swimming dates back to 1950's. Using a small-amplitude transverse planar wave immersed in viscous fluid, Taylor asymptotically expanded the no-slip boundary condition and calculated the leading order flow propelled by this idealized model swimmer [127]. Later, he used the same approach and extended the model to a more realistic three-dimensional waving cylinder with small amplitude [128]. Following this pioneering work, Hancock comes up with the idea of slender-body theory that the flow induced by a slender-body, which mathematically characterized by that the length L is much larger the breadth a , is asymptotically same as that due to an appropriate line distribution of hydrodynamic singularities [59]. The singularities 'stokeslet' and 'doublet' are also named in that paper. Slender-body theory has been vigorously developed during 1970's using matched asymptotics and uniform expansion [8, 31, 131, 70, 47, 65, 89]. The results allows us to more accurately quantify how the forces from the fluid affect the kinematics of organism with a wide range of geometries characterized by slenderness. In particular, Chwang and Wu studied the flow propelled by a helix, which quantitatively described how bacteria actuate their helical flagella [28].

Building on these classical works, recent study has addressed how to improve these classical models [91, 90], how to predict and measure the flow induced by microswimmers [136, 123, 36], and the crucial role that hydrodynamics has played in the evolution of the bacterial flagella [123]. Particularly, there are two questions in swimming that have been under much debate. One question is how complex fluids that present non-Newtonian rheology affect swimming. This is crucial because in reality microorganisms usually does not live in Newtonian fluids where most classical results have been derived. Extensive discussions emphasized on the interplay between different geometries of the swimmers and a variety of fluids such as viscoelastic fluids [114, 33, 37, 35], polymer solutions [99, 97, 87, 46], granular media [49, 105], etc. Another question which has received a lot of attention is the role played by hydrodynamic interactions, including interactions with surfaces [81, 14, 86, 48, 34, 36, 124, 94], external flows [120, 100, 115], complex fluids [143] and between cells [63, 74, 121]. One specific example is that many works have proved that hydrodynamic interactions can be an important cause leading to synchronization and coordination behavior between flagella or cilia [63, 71, 110, 57, 21].

In this thesis, I focus on the effects of complex fluids and hydrodynamic interactions and study two specific topics. In the first topic of complex fluids (Chapter. 2-3), I ask the question how slip boundary condition, which is widely shown in complex fluids such as polymer solutions, affects swimming. And in the second topic of hydrodynamic interactions (Chapter. 4-6), I derive a long-wavelength integration for interacting filaments and propose analytical models for flagellar bundling, which have been studied mainly by experiments and numerics before.

1.1 Swimming in complex fluids: Slip boundaries

Studies on cell motility in fluids typically focus on one of four types of cells – bacteria [11], spermatozoa [45], ciliates [15], and single-celled planktonic cells [54] – while recent effort considered larger, multi-cellular organisms [50]. In all cases, the biological environments that the microorganism encounter may be rheologically complex. For example, *Helicobacter pylori*, a bacterium that causes inflammation in the stomach, swims through gastric mucus to protect itself from the acidic environment [24]. Mammalian spermatozoa have to progress through highly-elastic cervical mucus, an important phase in reproductive process [68].

Extending our understanding of cell locomotion in Newtonian fluids to complex, gel-like or viscoelastic environments is a nontrivial task. One quintessential question, whether non-Newtonian stresses in a complex fluid help increase or decrease the swimming speed of the cell, remains in many ways an open problem.

For example, bacteria such as *Leptospira* and *Escherichia coli*, swim more rapidly in gel-like unbranched polymer solutions than in Newtonian fluids [13]. In contrast, for the nematode *Caenorhabditis elegans* undergoing undulatory swimming, the speed was observed to decrease in a slightly shear-thinning polymeric fluid with strong elastic stresses [116]. Similar disparities are observed experimentally for bio-inspired synthetic swimmers. Force-free rotating helices show a transition from hindered to enhanced swimming in constant-viscosity Boger fluids [93] while a cylindrical version of Taylor's swimming sheet displays both increase and decrease as a function of the rheology of the fluid [32]. In contrast, externally-actuated flexible-tail swimmers show a systematic increase of locomotion speeds in viscoelastic fluids [39].

Various numerical and theoretical studies have also addressed this problem, focusing on viscoelastic fluids following Oldroyd-B rheology. Small-amplitude asymptotic studies for waving swimmers with fixed shapes predicted a systematic decrease of swimming velocity [77, 44, 43]. Subsequent numerical work for finite waving sheets with large tail amplitude showed that an increase was possible for order one Deborah numbers [129]. Numerical simulations following the helical experiments in Ref. [93] confirmed the transition from slow small-amplitude swimming to fast large-amplitude locomotion [125]. Integral theorems for small-amplitude motion showed that the superposition of multiple waves could also lead to a enhancement transition for a range of Deborah numbers [79]. We thus see that theoretical, computational, and experimental studies showing both increases and decreases have been put forward, and the challenge is now to rigorously untangle the various physical (and sometimes, biological) effects. In particular, while we now understand how viscoelastic stresses are able to decrease swimming speeds, physical mechanisms leading to locomotion enhancement are less clear. Recently, the flexibility of the swimmer in response to complex stresses was shown to allow for an increase in the swimming speed [130, 114].

Instead of focusing on the non-Newtonian stresses in the fluid, I address effects of having a slip boundary condition on the surface. The slip effect is widely observed in complex fluids including polymer solution [7], capillary flow and porous medium [30] and particle immersed in electrolyte solution [76]. The slip can be caused by different reasons depending on various situations. For example the mechanism in polymer solution is due to a phase-separation near the boundary, which generates a thin layer of low concentration solution that leads to apparent slip, more details will be included in Chapter 2. While for the particle immersed in electrolyte solutions, the flow-induced streaming electric field can create an apparent slip velocity, which is called electroosmotic flow [76].

Inspired by the classical works decades ago, Taylor's swimming waves [127, 128] and slender-body theory [31, 88], I derive the flow and mobility relation with slip boundary

condition. The derivation with geometry of waving sheet and cylinder will be illustrated in Chapter. 2, which proposes the apparent slip due to a phase-separation particularly in polymer solutions as a new mechanism for enhanced swimming. In Chapter. 3, I consider the general slender body geometry and extend the classical results including local drag theory and slender-body theory in 1970's to slip cases.

1.2 Hydrodynamically interacting filaments: Flagellar bundling

Biological world is in rich with filamentous structures. Inside cells, polymeric filaments of microtubules, actin, and intermediate filaments fill the eukaryotic cytoplasm [4] and provide it with its mechanical structure [16]. Outside cells, the motion of flagella and cilia allow cells to generate propulsive forces [12, 18, 82] and induce flows critical to human health [118, 40]. In all cases, these biological filaments are immersed in a viscous fluid in which they move at low Reynolds number, be it due to their polymerisation, to fluctuations and thermal forces, or to the action of molecular motors [17].

Since at low Reynolds number, the flows induced locally by the motion of filaments relative to a background fluid have a slow spatial decay as $\sim 1/r$ [88, 2], we thus expect nonlocal hydrodynamic interactions to be important [51]. For example, hydrodynamic coupling has been proved by a few models that plays an crucial role in emergence of metachronal waves generated by cilia array [56, 135, 134, 103]. While for algal flagella, experiment showed that hydrodynamic interactions can lead to synchronisation of nearby filaments [21].

One particularly interesting phenomenon involving hydrodynamic interactions at the scale of a single cell is the bundling and unbundling of bacterial flagella [95]. While many bacteria have only one flagellum, most well-studied pathogenic bacteria possess multiple flagella, and are referred to as “peritrichous” bacteria (Fig. 1.1). Such bacteria are propelled from behind by a bundle of helical flagella, for example the well-studied *Escherichia coli* (*E. coli*) [12], *Salmonella typhimurium* [95], or *Halobacterium Salinarium* [75].

Comparing to significant experimental and computational advances [71, 72, 109, 110], theoretical studies have not been able yet to derive simplified models allowing it capture, from first principle, the essence of the dynamics of the bundling and unbundling process. The reason is that integrating long-ranged hydrodynamic interactions between filaments has long been recognised as a challenging problem, and one where the theoretical approach has consisted of either full numerical simulations or very simplified analysis. For example numerical methods has been developed to tackle the integration including slender-body theory [65, 57, 132], boundary elements to implement boundary integral formulations [67], the

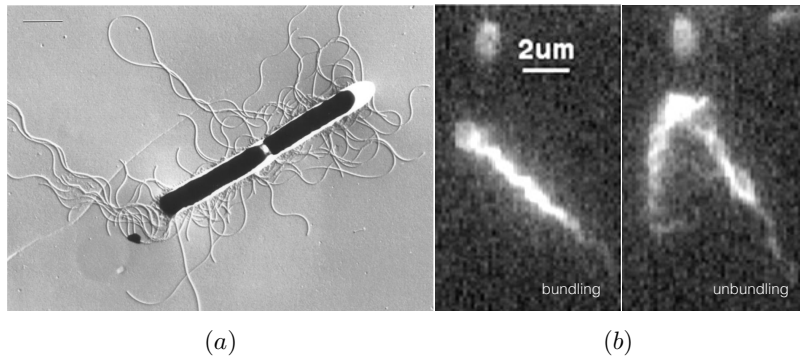


Fig. 1.1 (a) two *Bacillus subtilis* cells [29] (courtesy of C. Dombrowski and R.E. Goldstein, University of Cambridge) (b) illustration of bundling and unbundling dynamics of bacterial flagellar filaments of *E. coli* [133]. Panel (b) reproduced from Turner et al. (2000) Real-time imaging of fluorescent flagellar filaments, *J. Bacteriol.*, **182**, 2793-2801, Copyright 2000 Society of Microbiology.

immersed boundary method [92, 139], regularized flow singularities [41] and particle-based methods [140, 111].

While these computational approaches allow to address complex geometries and dynamics, the difficulty of integrating long-range hydrodynamic interactions have prevented analytical approaches to provide insight beyond simplified setups. The two most popular approaches consist in replacing the dynamics in three dimensions by a two-dimensional problem for which the analysis may be easier to carry out [127, 38], or by focusing on far-field hydrodynamic interactions and ignoring the geometrical details of near-field hydrodynamics, a popular approach to study synchronisation of flagella and cilia [135, 58, 103, 134, 52, 42, 9].

In realistic biological situations, three-dimensional filaments are not far from each other, but in fact are often found in the opposite, near-field, limit where their separation distance is much smaller than their length. This is illustrated in Fig. 1a with three examples relevant to cell motility: synchronizing flagella of spermatozoa; bundle of bacterial flagellar filaments; epithelium cilia. In order to capture the dynamics of these interacting filaments, new analytical tools are thus required.

In order to give a full analytical description of the problem, I first focus on the central issue, the long-ranged hydrodynamic interactions between two filaments, in Chapter 4. Arising from the real biological geometries, I consider three characterised length scales, radius of single filament a , separation between two filaments h and total length of each filament L . Considering the experimental measurements of these lengths, in theory a length separation can be reasonably assumed as $a \ll h \ll L$. Taking advantage of this length separation, I asymptotically derive the leading order force exerted by the interacting flow. This result is very

general and is capable to be applied to a wide range of problems in biological physics. Using this analytical tool, I move on to the specific problem of flagellar bundling and build an elastic-filaments model in Chapter. 5. This initial model is well-studied due to its simplicity and extends to rich observations in dynamics. Building on this, I continue to consider more realistic synchronisation model with helical geometry, which is an important feature neglected in my initial model. The asymptotic measurement of forces and torques and a recovery-torque model for synchronisation are illustrated in Chapter. 6.

Chapter 2

Phase-separation models for swimming enhancement in complex fluids

For a variety of complex fluids with a microstructure dispersed in a solvent, in particular polymeric fluids and suspensions, the presence of a boundary leads to static phase separation at equilibrium: the concentration of the solute drops near the wall which is covered instead by a thin solvent layer [7]. In the case of rigid suspensions, purely excluded-volume interactions lead to solvent-rich regions near the surface, and the effect is larger for Brownian particles for which the presence of a wall breaks the geometrical isotropy [7]. In the case of polymers, random coils would be distorted if too close to the wall, and thus they are driven by entropy away from the boundary.

In all cases, the solvent-rich fluid near the surface has a viscosity much smaller than that of the bulk fluid. As seen in many situations, in particular flows in capillary tubes and in porous media [30], this difference in viscosity leads to apparent slip when a flow is set up, which is best illustrated in the case of a shear flow (Fig. 2.1b): If shear is imposed in a fluid with a thin-viscosity layer, the difference in viscosities will lead to a difference in shear rates, and as a result the flow in the high-viscosity bulk will not extrapolate to zero on the solid surface, but below it, indicating an overall decrease of stresses acting on the surface. The fictitious distance below the surface where the fluid velocity in the top fluid goes to zero is the (positive) apparent slip length. Microscopically, the no-slip condition is of course not violated, but given that the typical thickness of the solvent layer is much smaller than the other, macroscopic length scales in the problem of interest, the no-slip boundary condition appears not to hold for the bulk fluid.

There are two classical ways to theoretically model apparent slip in complex fluids. The first model is to simply replace the no-slip boundary condition on the surface by one which the tangential velocity is allowed to slip. Experimentally-measured slip length has

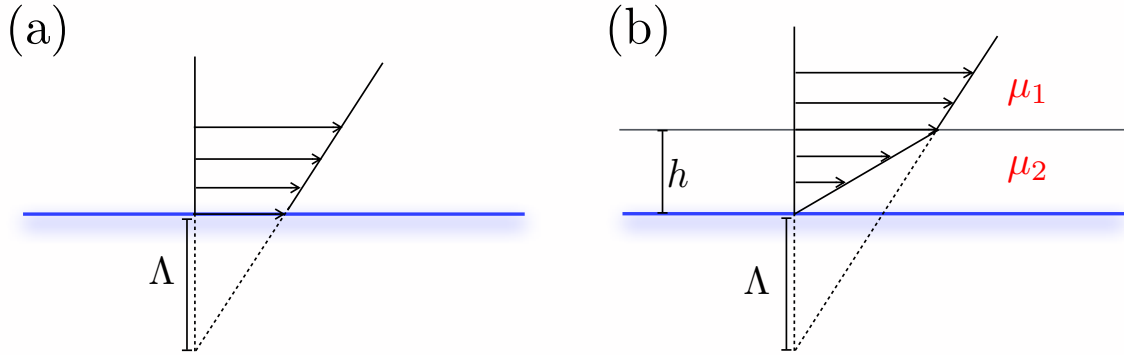


Fig. 2.1 The two models of apparent slip due to phase separation considered in this paper; (a): a single-phase continuum fluid with a finite apparent slip length Λ ; (b): a two-fluid domain with viscosity μ_1 in the bulk and a thin low-viscosity layer of thickness h and viscosity $\mu_2 < \mu_1$.

been shown to depend, sometimes in a complex manner, on the shear stress at the wall [122, 141, 5, 30]. The assumption usually done is to adopt Navier's slip length model [102] and assume that the slip velocity at the wall is linearly proportional to the wall shear rate, with a proportionality constant with unit of length, called the slip length, and which we will denote Λ in this work [119]. As noted above, the slip length measures the (fictitious) distance below the boundary where the velocity would extrapolate to zero, and it is zero in the case of a no-slip boundary (Fig. 2.1a). A second procedure to model phase separation is to explicitly assume the presence of two fluid layers. The top layer, semi-infinite, has bulk viscosity μ_1 , while the bottom layer near the surface has a finite thickness h and lower viscosity $\mu_2 < \mu_1$ (Fig. 2.1b). For a shear flow in this unidirectional setup, the velocity in the thin layer satisfies the no-slip boundary condition while that the flow in the bulk fluid extrapolates to zero at the equivalent apparent slip length $\Lambda = (\mu_1/\mu_2 - 1)h$.

In this chapter I consider these two different physical models of phase separation and investigate their consequences on waving locomotion. In §2.1 I first examine the model with a finite apparent slip length, and apply it to two canonical setups for low-Reynolds number locomotion, namely the small-amplitude swimming of a flexible sheet [127] and that of a flexible filament [128]. In §2.2 I then consider the same two setups in the situation where the phase-separated fluid is modeled as a two-fluid layer. In all cases I am able to derive the swimming speed for each swimmer analytically and compare it to the case for the homogenous Newtonian fluid with a no-slip boundary condition. I demonstrate that the phase separation leads to a systematic enhancement of the swimming speed, and suggest that

this might play a role in the recently-measured swimming enhancement at low-Reynolds numbers.

2.1 Swimming in a fluid with finite apparent slip length

In the first section I assume that the phase separation in the fluid can be adequately captured by an effective slip length Λ acting on a Newtonian fluid satisfying the Stokes equations

$$\nabla p = \mu \nabla^2 \mathbf{u}, \quad \nabla \cdot \mathbf{u} = 0. \quad (2.1)$$

On a fluid-solid boundary S , the jump in normal velocity is zero by mass conservation while the jump in tangential velocity is proportional to the local shear rate. If the velocity in the fluid is denoted \mathbf{u} , these boundary conditions can be mathematically expressed as

$$[\mathbf{n} \cdot \mathbf{u}]|_S = 0, \quad (2.2a)$$

$$[\mathbf{n} \times \mathbf{u}]|_S = 2\Lambda(\mathbf{n} \times (\mathbf{E} \cdot \mathbf{n}))|_S, \quad (2.2b)$$

where $[...]$ is used to denote a jump, \mathbf{n} is the normal to the boundary, \mathbf{E} is the symmetric rate-of-strain tensor (i.e. the symmetric part of the velocity gradient tensor), and Λ the slip length.

2.1.1 Two dimensional waving sheet

First I consider a two-dimensional swimmer in the form of flexible sheet self-propelling in the fluid by passing waves of normal deformation. This is the classical setup originally proposed by Taylor [127], and the material points of the sheet, (x_s, y_s) , are assumed to vary in space and time as a simple traveling wave of deformation

$$y_s = b \sin k(x - ct), \quad x_s = x, \quad (2.3)$$

where b is the wave amplitude, k the wave number and c the wave speed along the x direction (see notation in Fig. 2.2). I solve the problem assuming that the amplitude is small compared to the wavelength, and thus consider the asymptotic limit where $\varepsilon = bk$ is a small dimensionless number. Nondimensionalizing the equations using k^{-1} as relevant length and $\omega^{-1} \equiv (kc)^{-1}$ as intrinsic time scale, the wave deformation becomes

$$\bar{y}_s = \varepsilon \sin(\bar{x} - \bar{t}) \equiv \varepsilon \sin \xi, \quad (2.4)$$

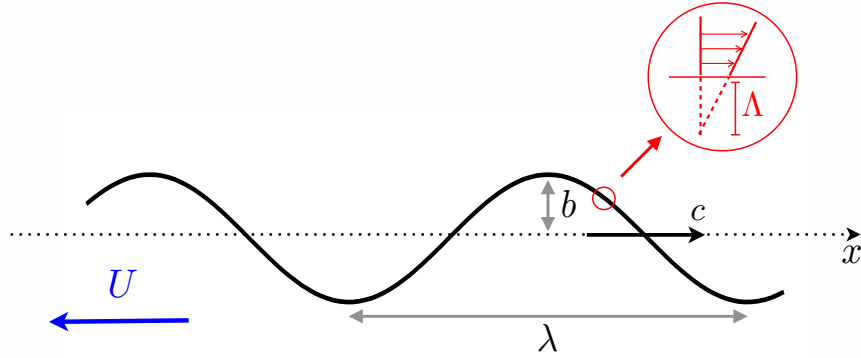


Fig. 2.2 Geometry of the two-dimensional waving sheet setup in a fluid with finite slip length. Here b denotes the small waving amplitude, λ the wavelength, and c the wave speed along the x direction. The sheet is assumed to swim with speed U in the negative x direction. The small circle zooms in on a portion of the swimmer surface and illustrates the presence of a finite slip length Λ .

and for convenience we drop the “bars” in what follows.

The velocity of material points on the sheet is thus given by

$$\mathbf{u}_s = (0, -\varepsilon \cos \xi). \quad (2.5)$$

Applying Eq. (2.2), on the surface of the swimmer we have

$$(\mathbf{n} \cdot \mathbf{u})|_{(x_s, y_s)} = \mathbf{n} \cdot \mathbf{u}_s, \quad (2.6a)$$

$$(\mathbf{n} \times \mathbf{u})|_{(x_s, y_s)} = 2\bar{\Lambda}(\mathbf{n} \times (\mathbf{E} \cdot \mathbf{n}))|_{(x_s, y_s)} + \mathbf{n} \times \mathbf{u}_s, \quad (2.6b)$$

with a normal vector \mathbf{n} explicitly given as $(1 + \varepsilon^2 \cos^2 \xi)^{-\frac{1}{2}} [-\varepsilon \cos \xi, 1]$, and where $\bar{\Lambda} \equiv k\Lambda$ is the nondimensionalized slip length. Here let us keep the “bar” notation for the slip length to ensure that the final result is formally dimensionless.

In order to solve for the Stokes equations in the fluid, Eq. (2.1), I employ a streamfunction ψ such that the velocity components of $\mathbf{u} = [u, v]$ are defined as $u = \frac{\partial \psi}{\partial y}$ and $v = -\frac{\partial \psi}{\partial x}$. The

boundary condition, Eq. (2.6), then becomes

$$\varepsilon \cos \xi \frac{\partial \psi}{\partial y}(x, \varepsilon \sin \xi) + \frac{\partial \psi}{\partial x}(x, \varepsilon \sin \xi) = \varepsilon \cos \xi, \quad (2.7a)$$

$$\begin{aligned} \varepsilon \cos \xi \frac{\partial \psi}{\partial x}(x, \varepsilon \sin \xi) - \frac{\partial \psi}{\partial y}(x, \varepsilon \sin \xi) &= \bar{\Lambda}(1 + \varepsilon^2 \cos^2 \xi)^{-\frac{1}{2}} \left\{ (1 - \varepsilon^2 \cos^2 \xi) \right. \\ &\quad \left[\frac{\partial^2 \psi}{\partial x^2}(\xi, \varepsilon \sin \xi) - \frac{\partial^2 \psi}{\partial y^2}(\xi, \varepsilon \sin \xi) \right] \\ &\quad \left. + 4\varepsilon \cos \xi \frac{\partial^2 \psi}{\partial x \partial y}(\xi, \varepsilon \sin \xi) \right\} + \varepsilon^2 \cos^2 \xi. \end{aligned} \quad (2.7b)$$

The Stokes equation, Eq. (2.1), transforms into the biharmonic equation for ψ [84]

$$\nabla^4 \psi = 0. \quad (2.8)$$

In order to obtain the asymptotic solution for the swimming velocity, I expand the stream-function in powers of ε by

$$\psi = \varepsilon \psi^{(1)} + \varepsilon^2 \psi^{(2)} + \varepsilon^3 \psi^{(3)} + \dots \quad (2.9)$$

Denoting the velocity of the swimming sheet as $-U \mathbf{e}_x$ in a quiescent fluid, we move in the swimming frame and thus the velocity at infinity is given by $\mathbf{u}(y \rightarrow \infty) = U \mathbf{e}_x$.

Since ψ satisfies the biharmonic equation, and is equal to Uy at infinity, I construct the general solution as [27]

$$\psi^{(1)} = V_1^{(1)} + U^{(1)}y, \quad (2.10a)$$

$$\psi^{(2)} = V_1^{(2)} + V_2^{(2)} + U^{(2)}y, \quad (2.10b)$$

where

$$V_n = (A_n + B_n y) e^{-ny} \sin n\xi + (C_n + D_n y) e^{-ny} \cos n\xi. \quad (2.11)$$

At first order in ε , Eq. (2.7) becomes

$$\frac{\partial \psi^{(1)}}{\partial x}(x, 0) = \cos \xi, \quad (2.12a)$$

$$-\frac{\partial \psi^{(1)}}{\partial y}(x, 0) = \bar{\Lambda} \left(\frac{\partial^2 \psi^{(1)}}{\partial x^2} - \frac{\partial^2 \psi^{(1)}}{\partial y^2} \right) \Big|_{(x, 0)}. \quad (2.12b)$$

Substituting Eq. (2.10) into the equation above, we obtain $A_1^{(1)} = B_1^{(1)} = 1$, $C_1^{(1)} = D_1^{(1)} = 0$ and $U^{(1)} = 0$. The streamfunction at first order is

$$\psi^{(1)} = (1+y)e^{-y} \sin \xi, \quad (2.13)$$

which is the same as the no-slip case. This can be rationalized by noting that the first-order shear rate is given by

$$\left(\frac{\partial^2 \psi^{(1)}}{\partial x^2} - \frac{\partial^2 \psi^{(1)}}{\partial y^2} \right) \Big|_{(x,0)} = (-2ye^{-y} \sin \xi) \Big|_{(x,0)} = 0, \quad (2.14)$$

which makes the problem equivalent to the no-slip case.

As no propulsion occurs at order ε , one needs to carry the calculation to order two in order to obtain the leading-order swimming speed. At order ε^2 , the boundary conditions are

$$\left(\cos \xi \frac{\partial \psi^{(1)}}{\partial y} + \frac{\partial \psi^{(2)}}{\partial x} + \sin \xi \frac{\partial^2 \psi^{(1)}}{\partial x \partial y} \right) \Big|_{(x,0)} = 0, \quad (2.15a)$$

$$\begin{aligned} \left(\cos \xi \frac{\partial \psi^{(1)}}{\partial x} - \frac{\partial \psi^{(2)}}{\partial y} - \sin \xi \frac{\partial^2 \psi^{(1)}}{\partial y^2} \right) \Big|_{(x,0)} &= \bar{\Lambda} \left\{ \left(\frac{\partial^2 \psi^{(2)}}{\partial x^2} - \frac{\partial^2 \psi^{(2)}}{\partial y^2} \right) + \right. \\ &\quad \left. \sin \xi \left(\frac{\partial^3 \psi^{(1)}}{\partial x^2 \partial y} - \frac{\partial^3 \psi^{(1)}}{\partial y^3} \right) \right. \\ &\quad \left. + 4 \cos \xi \frac{\partial^2 \psi^{(1)}}{\partial x \partial y} \right\} \Big|_{(x,0)} + \frac{1}{2} + \frac{1}{2} \cos 2\xi. \end{aligned} \quad (2.15b)$$

Substituting the expansions for the streamfunction into this condition, we obtain

$$U^{(2)} = \frac{1}{2} + \bar{\Lambda}. \quad (2.16)$$

Comparing this result with the no-slip case, and coming back to the dimensional variables we finally have

$$\frac{U^{(2)}}{U_{\text{no-slip}}^{(2)}} = 1 + 2k\Lambda. \quad (2.17)$$

Since the slip length is always positive, we obtain in this first situation that the swimming speed is always enhanced by apparent slip.

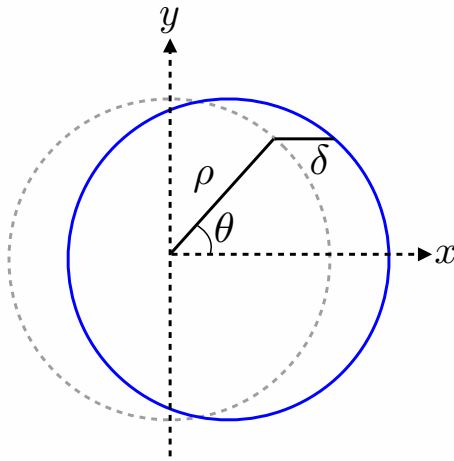


Fig. 2.3 Deformation with amplitude δ in the circular cross-section of a three-dimensional waving filament of radius ρ . The blue solid line represents the current position of the filament and the gray dashed line the average location of the cross section.

2.1.2 Three-dimensional waving filament

Now I apply the same apparent-slip model to the case of a three-dimensional waving filament, the geometry of which is shown in Fig. 2.3 [128]. I consider a cylindrical filament of radius ρ deforming as a traveling wave in the (x, z) plane where z is along the filament axis and x is perpendicular to it. I denote by δ the amplitude of the filament deformation in the x direction.

The location of the material points on the surface of the filament, using cartesian coordinate centered on the average location of the cylinder (see Fig. 2.3), is given by

$$\mathbf{r}_s = (\delta + \rho \cos \theta) \mathbf{x} + \rho \sin \theta \mathbf{y} + z \mathbf{z}, \quad \delta = b \sin k(z + ct), \quad (2.18)$$

where δ is the distribution of waving amplitudes along z direction, ρ the filament radius, k the wave number, and c the wave speed. Here again we assume that the amplitude is small compared to the wavelength, and compute the result in the limit where $\varepsilon = bk$ is small.

Nondimensionalizing the equations similarly to the previous section, then the surface of cylindrical filament described as

$$\mathbf{r}_s = (\delta + \bar{\rho} \cos \theta) \mathbf{x} + \bar{\rho} \sin \theta \mathbf{y} + z \mathbf{z}, \quad \delta = \varepsilon \sin(z + t) = \varepsilon \sin s, \quad (2.19)$$

and here again we keep the “bar” notation for the dimensionless radius, $\bar{\rho} = k\rho$. Similarly to the two-dimensional case, the velocity on the boundary satisfies the conditions

$$(\mathbf{n} \cdot \mathbf{u})|_{(\delta + \bar{\rho} \cos \theta, \bar{\rho} \sin \theta, z)} = \varepsilon \cos s \cos \theta, \quad (2.20a)$$

$$(\mathbf{n} \times \mathbf{u})|_{(\delta + \bar{\rho} \cos \theta, \bar{\rho} \sin \theta, z)} = 2\bar{\Lambda}\{\mathbf{n} \times (\mathbf{E} \cdot \mathbf{n})\}|_{(\delta + \bar{\rho} \cos \theta, \bar{\rho} \sin \theta, z)} - \varepsilon \sin \theta \cos s \quad (2.20b)$$

Since the inextensibility condition contributes to the dynamics at orders higher than two [128], the vector normal to the surface is \mathbf{e}_r at the order relevant for this calculation. Then the velocity can be expanded around the average position as

$$\begin{aligned} \mathbf{u}(\delta + \bar{\rho} \cos \theta, \bar{\rho} \sin \theta, z) &\approx [\mathbf{u} + \mathbf{x} \cdot (\nabla \mathbf{u}) \varepsilon \sin s]|_{r=\bar{\rho}} \\ &= \left\{ u + \varepsilon \sin s \left[\frac{\partial u}{\partial r} \cos \theta - \left(\frac{1}{r} \frac{\partial u}{\partial \theta} - \frac{v}{r} \right) \sin \theta \right] \right\} \Big|_{r=\bar{\rho}} \mathbf{e}_r \\ &+ \left\{ v + \varepsilon \sin s \left[\frac{\partial v}{\partial r} \cos \theta - \left(\frac{u}{r} + \frac{1}{r} \frac{\partial v}{\partial \theta} \right) \sin \theta \right] \right\} \Big|_{r=\bar{\rho}} \mathbf{e}_\theta \quad (2.21) \\ &+ \left\{ w + \varepsilon \sin s \left[\frac{\partial w}{\partial r} \cos \theta - \frac{1}{r} \frac{\partial w}{\partial \theta} \sin \theta \right] \right\} \Big|_{r=\bar{\rho}} \mathbf{e}_z. \end{aligned}$$

Expanding the velocity in the fluid, \mathbf{u} , asymptotically in powers of ε ,

$$\mathbf{u} = \varepsilon \mathbf{u}^{(1)} + \varepsilon^2 \mathbf{u}^{(2)} + \dots, \quad (2.22)$$

and substituting the expansion and Eq. (2.21) into the boundary condition, that at first order,

$$u^{(1)}(\bar{\rho}, \theta, z) = \cos s \cos \theta, \quad (2.23a)$$

$$v^{(1)}(\bar{\rho}, \theta, z) = \bar{\Lambda} \left(\frac{\partial v^{(1)}}{\partial r} - \frac{v^{(1)}}{r} + \frac{1}{r} \frac{\partial u^{(1)}}{\partial \theta} \right) \Big|_{(r=\bar{\rho})} - \sin \theta \cos s, \quad (2.23b)$$

$$w^{(1)}(\bar{\rho}, \theta, z) = \bar{\Lambda} \left(\frac{\partial w^{(1)}}{\partial r} + \frac{\partial u^{(1)}}{\partial z} \right) \Big|_{(r=\bar{\rho})}. \quad (2.23c)$$

Solving for the fluid velocity using separation of variables we get

$$u^{(1)} = u_q(r) \cos \theta \cos s, \quad v^{(1)} = v_q(r) \sin \theta \cos s, \quad w^{(1)} = w_q(r) \cos \theta \sin s, \quad (2.24)$$

while the first-order boundary conditions are simplified to

$$u_q(\bar{\rho}) = 1, \quad (2.25a)$$

$$v_q(\bar{\rho}) = \bar{\Lambda} \left[v'_q(\bar{\rho}) - \frac{v_q(\bar{\rho})}{\bar{\rho}} - \frac{1}{\bar{\rho}} \right] - 1, \quad (2.25b)$$

$$w_q(\bar{\rho}) = \bar{\Lambda} [w'_q(\bar{\rho}) - 1]. \quad (2.25c)$$

Similarly to the original problem treated by Taylor in the case of a no-slip filament [128], the radial dependence of the velocity is given by a combination of modified Bessel functions as

$$u_q(r) = BK_2(r) + CK_0(r) + ArK_1(r) + EI_2(r) + FI_0(r) + DrI_1(r), \quad (2.26a)$$

$$v_q(r) = BK_2(r) - CK_0(r) + EI_2(r) - FI_0(r), \quad (2.26b)$$

$$\begin{aligned} w_q(r) = & BK_1(r) + CK_1(r) + A[rK_0(r) - K_1(r)] - EI_1(r) - FI_1(r) \\ & - D[rI_0(r) - I_1(r)], \end{aligned} \quad (2.26c)$$

with a minus sign in Eq. 2.26c coming from different properties between solution of the first and second kind. For the boundary conditions at infinity, we have $D = E = F = 0$ and the other three unknown constants A, B, C can be obtained by plugging Eq. (2.26) into Eq. (2.25). Writing C as $C = C_{\text{nu}}/C_{\text{de}}$, I obtain the following lengthy (but analytical) expressions

$$C_{\text{nu}} = \bar{\rho}K_1(\bar{\rho})^2 - 2\bar{\rho}K_0(\bar{\rho})K_2(\bar{\rho}) + 2K_1(\bar{\rho})K_2(\bar{\rho}) + \bar{\Lambda} \left[-\frac{\bar{\rho}}{2}K_0(\bar{\rho})K_1(\bar{\rho}) \right. \quad (2.27a)$$

$$\left. - K_0(\bar{\rho})K_2(\bar{\rho}) + 2K_1(\bar{\rho})^2 + \left(\frac{4}{\bar{\rho}} - \frac{5}{2}\bar{\rho} \right) K_1(\bar{\rho})K_2(\bar{\rho}) + K_2(\bar{\rho})^2 \right]$$

$$+ \bar{\Lambda}^2 \left[2K_0(\bar{\rho})K_1(\bar{\rho}) - 2\bar{\rho}K_1(\bar{\rho})^2 + \frac{6}{\bar{\rho}}K_0(\bar{\rho})K_2(\bar{\rho}) \right.$$

$$\left. - 6K_1(\bar{\rho})K_2(\bar{\rho}) + \frac{2}{\bar{\rho}}K_2(\bar{\rho})^2 \right],$$

$$C_{\text{de}} = -2\bar{\rho}K_0(\bar{\rho})^2K_2(\bar{\rho}) + 2K_0(\bar{\rho})K_1(\bar{\rho})K_2(\bar{\rho}) + \bar{\rho}K_0(\bar{\rho})K_1(\bar{\rho})^2 + \bar{\rho}K_1(\bar{\rho})^2K_2(\bar{\rho}) \quad (2.27b)$$

$$+ \bar{\Lambda} \left[-\frac{\bar{\rho}}{2}K_0(\bar{\rho})^2K_1(\bar{\rho}) + 2\bar{\rho}K_1(\bar{\rho})^3 + 2K_0(\bar{\rho})K_1(\bar{\rho})^2 + K_0(\bar{\rho})K_2(\bar{\rho})^2 \right.$$

$$\left. - K_0(\bar{\rho})^2K_2(\bar{\rho}) + 4K_1(\bar{\rho})^2K_2(\bar{\rho}) + \frac{\bar{\rho}}{2}K_1(\bar{\rho})K_2(\bar{\rho})^2 \right]$$

$$+ \left(\frac{4}{\bar{\rho}} - 2\bar{\rho} \right) K_0(\bar{\rho})K_1(\bar{\rho})K_2(\bar{\rho}) \left. \right] + \bar{\Lambda}^2 \left[2K_0(\bar{\rho})^2K_1(\bar{\rho}) + \frac{6}{\bar{\rho}}K_0(\bar{\rho})^2K_2(\bar{\rho}) \right.$$

$$\left. + \frac{2}{\bar{\rho}}K_0(\bar{\rho})K_2(\bar{\rho})^2 + 2K_1(\bar{\rho})K_2(\bar{\rho})^2 \right],$$

$$B = \frac{1}{C_{de}} \left\{ -\bar{\rho} K_1(\bar{\rho})^2 + \bar{\Lambda} \left[-\frac{5}{2} \bar{\rho} K_0(\bar{\rho}) K_1(\bar{\rho}) - \frac{\bar{\rho}}{2} K_1(\bar{\rho}) K_2(\bar{\rho}) \right] - 2\bar{\Lambda}^2 \bar{\rho} K_1(\bar{\rho})^2 \right\}, \quad (2.28)$$

and

$$A = \frac{1}{C_{de}} \left\{ 2K_1(\bar{\rho}) K_2(\bar{\rho}) + \bar{\Lambda} \left[2K_1(\bar{\rho})^2 + 3K_0(\bar{\rho}) K_2(\bar{\rho}) + \frac{4}{\bar{\rho}} K_1(\bar{\rho}) K_2(\bar{\rho}) + K_2(\bar{\rho})^2 \right] + \bar{\Lambda}^2 \left[2K_0(\bar{\rho}) K_1(\bar{\rho}) + \frac{6}{\bar{\rho}} K_0(\bar{\rho}) K_2(\bar{\rho}) + 2K_1(\bar{\rho}) K_2(\bar{\rho}) + \frac{2}{\bar{\rho}} K_2(\bar{\rho})^2 \right] \right\}. \quad (2.29)$$

According to Eq. (2.24), the time-averaged swimming speed $w^{(1)}$ is zero, and as expected I thus need to consider the problem at order ε^2 .

Following the slip boundary conditions, the z -component of the flow at order two, $w^{(2)}$, satisfies on the boundary

$$\begin{aligned} \left. \left(w^{(2)} + w'_q \cos^2 \theta \sin^2 s + \frac{1}{r} w_q \sin^2 \theta \sin^2 s \right) \right|_{r=\bar{\rho}} &= \bar{\Lambda} \left\{ \frac{\partial w^{(2)}}{\partial r} + \frac{\partial u^{(2)}}{\partial z} \right. \\ &\quad + \sin^2 s \left[(w''_q - u'_q) \cos^2 \theta \right. \\ &\quad \left. - \frac{1}{r} \left(\frac{w_q}{r} - w'_q + u_q + v_q \right) \sin^2 \theta \right] \\ &\quad \left. + \cos^2 s \left[u'_q \cos^2 \theta + \frac{u_q + v_q}{r} \sin^2 \theta \right] \right\} \Big|_{r=\bar{\rho}}. \end{aligned} \quad (2.30)$$

Averaging this equation in time and along the azimuthal direction, explicitly the swimming velocity, $U^{(2)}$, is written as

$$\begin{aligned} 4U^{(2)} &= w'_q(\bar{\rho}) + \frac{w_q(\bar{\rho})}{\bar{\rho}} - \bar{\Lambda} \left[w''_q - \frac{1}{\bar{\rho}} \left(\frac{w_q}{\bar{\rho}} - w'_q \right) \right] \Big|_{r=\bar{\rho}} \\ &= \left[\frac{2}{\bar{\rho}} K_1(\bar{\rho}) - K_2(\bar{\rho}) - \bar{\Lambda} K_1(\bar{\rho}) \right] B + \left[\frac{2}{\bar{\rho}} K_1(\bar{\rho}) - K_2(\bar{\rho}) - \bar{\Lambda} K_1(\bar{\rho}) \right] C \\ &\quad + \left\{ 2K_0(\bar{\rho}) - \bar{\rho} K_1(\bar{\rho}) - \frac{2}{\bar{\rho}} K_1(\bar{\rho}) + K_2(\bar{\rho}) + \bar{\Lambda} [5K_1(\bar{\rho}) - \bar{\rho} K_2(\bar{\rho})] \right\} A. \end{aligned} \quad (2.31)$$

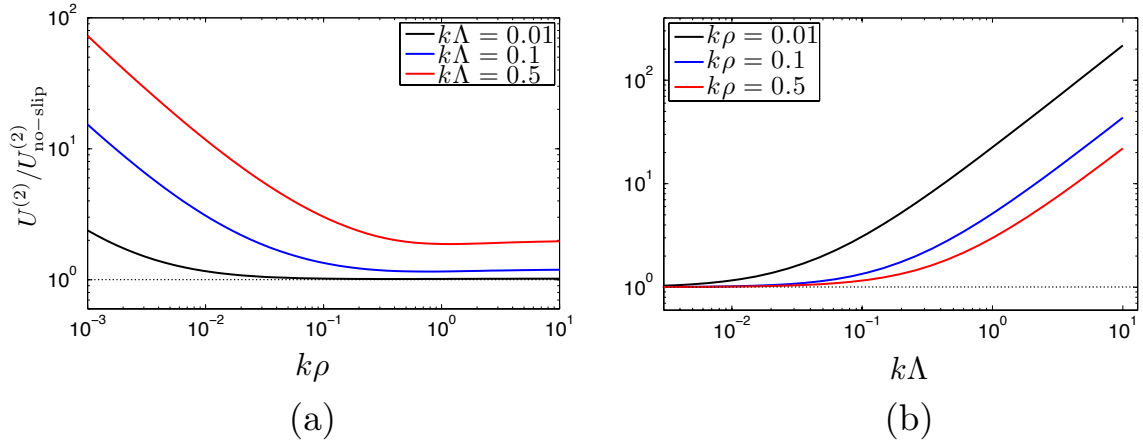


Fig. 2.4 Ratio of the swimming velocity in the case of slip to the no-slip value, $U^{(2)}/U_{\text{no-slip}}^{(2)}$. (a): Dependence on the dimensionless filament radius, $k\rho$, for three wave numbers ($k\Lambda = 0.01, 0.1$ and 0.5); (b): Dependence on the dimensionless wave number (with $k\rho = 0.01, 0.1$ and 0.5).

The result in Eq. (2.31) can also be evaluated in the no-slip case by simply setting $\bar{\Lambda} = 0$, and let us recover Taylor's result, namely

$$U_{\text{no-slip}}^{(2)} = \frac{\bar{\rho} K_1(\bar{\rho})^2 K_2(\bar{\rho}) - \bar{\rho} K_0(\bar{\rho}) K_2(\bar{\rho})^2}{-2\bar{\rho} K_0(\bar{\rho}) K_1(\bar{\rho})^2 + 4\bar{\rho} K_0(\bar{\rho})^2 K_2(\bar{\rho}) - 4K_0(\bar{\rho}) K_1(\bar{\rho}) K_2(\bar{\rho}) - 2\bar{\rho} K_1(\bar{\rho})^2 K_2(\bar{\rho})}. \quad (2.32)$$

The ratio between the swimming speed in the slip case to that in the no-slip situation, $U^{(2)}/U_{\text{no-slip}}^{(2)}$, is plotted in Fig. 2.4 as a function of the dimensionless filament radius (Fig. 2.4a) and the dimensionless wave number (Fig. 2.4b). As in the two-dimensional situation, the presence of slip is seen to always lead to faster swimming than in the no-slip case, and here the effect can be potentially very large (the applicability of these results to recent experiments is discussed in §2.3). In Fig. 2.4 we see that the swimming speed increases monotonically when either the length scale of the swimmer cross section (ρ) or the typical length scale of the waving motion, k^{-1} becomes smaller than the slip length. In the opposite limit, the no-slip result, Eq. (2.32), is recovered when all length scales are much larger than Λ .

We further note that it is possible to compute the swimming speed for small slip length as a power expansion in $k\Lambda$ (i.e. $\bar{\Lambda}$), $U^{(2)} = U_0^{(2)} + (k\Lambda)U_1^{(2)} + \dots$, with $U_0^{(2)}$ being the no-slip swimming speed. When $k\rho$ (i.e. $\bar{\rho}$) increases to infinity, the radius of the cylinder becomes much larger than any other length scale, and we recover $U_1^{(2)}/U_0^{(2)} = 2$, leading to $U^{(2)}/U_{\text{no-slip}}^{(2)} = 1 + 2k\Lambda$, which as expected agrees with the results for the two-dimensional sheet.

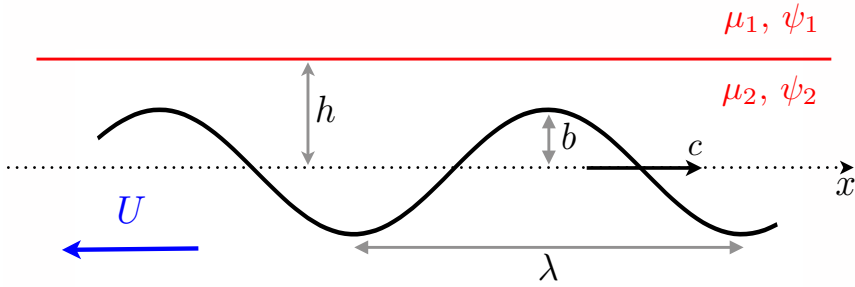


Fig. 2.5 Geometry of two-dimensional waving sheet swimming in a two-fluid domain. The bulk fluid has viscosity μ_1 and the thin layer near the swimmer, of mean thickness h , has viscosity $\mu_2 < \mu_1$. The two streamfunctions in the fluids are denoted ψ_1 and ψ_2 . The interface between the two fluids is assumed to remain flat.

I conclude by pointing out that although the calculation above was carried out in the case of planar waving deformation, similar algebra would govern swimming by propagating helical waves [?], and in that case ρ would be the radius of the helical flagellum, or that of the bundle of flagella in the case of bacteria with multiple flagellar filaments such as *E. coli*.

2.2 Swimming in a two-fluid domain

In the previous section, I modelled the influence of phase separation as due to a finite apparent slip length, and showed that it leads to a systematic enhancement of the swimming speeds. In order to provide an alternative microscopic physical picture, instead I consider in this section a second model where ncludes explicitly the presence of a low-viscosity layer near the surface of the swimmer, and I apply it to the two canonical swimmers (waving sheet and filament) considered in the previous section.

2.2.1 Two dimensional waving sheet

I first consider the swimming sheet setup shown in Fig. 2.5. The fluid is composed of two domains: the bulk fluid has viscosity μ_1 while the thin layer near the swimmer has a smaller viscosity μ_2 ($\mu_1 > \mu_2$). The average distance between the sheet and the fluid-fluid interface, which is the thickness of the low-viscosity layer, is denoted h and assumed to remain constant (this assumption is discussed in §2.3). All other notation are similar to the ones in §2.1.1. Following the same nondimensionalization, we now have the no-slip boundary conditions on the sheet

$$\frac{\partial \psi_2}{\partial y}(x, \varepsilon \sin \xi) = 0, \quad \frac{\partial \psi_2}{\partial x}(x, \varepsilon \sin \xi) = -\varepsilon \cos \xi, \quad (2.33)$$

while at infinity we have the unknown swimming speed

$$\frac{\partial \psi_1}{\partial y}(x, \infty) = -U, \quad \frac{\partial \psi_1}{\partial x}(x, \infty) = 0. \quad (2.34)$$

At the flat interface between the two fluids, continuity of velocities is

$$\frac{\partial \psi_1}{\partial y}(x, \bar{h}) = \frac{\partial \psi_2}{\partial y}(x, \bar{h}), \quad \frac{\partial \psi_1}{\partial x}(x, \bar{h}) = \frac{\partial \psi_2}{\partial x}(x, \bar{h}) = 0, \quad (2.35)$$

and here again, keep the “bar” notation for the thickness $\bar{h} \equiv kh$. Together with continuity of tangential stresses, which is written as

$$\left(\frac{\partial^2 \psi_1}{\partial y^2} - \frac{\partial^2 \psi_1}{\partial x^2} \right) \Big|_{(x, \bar{h})} = \beta \left(\frac{\partial^2 \psi_2}{\partial y^2} - \frac{\partial^2 \psi_2}{\partial x^2} \right) \Big|_{(x, \bar{h})}, \quad (2.36)$$

where β denotes the ratio of viscosities, $\beta = \mu_2/\mu_1 < 1$.

As in §2.1.1 I solve the problem as a perturbation expansion in ε . The general periodic solution for to the biharmonic equation which vanishes at infinity is obtained by separation of variables as

$$V_n = (a_n y + b_n) \sin n\xi e^{-ny} + (c_n y + d_n) \cos n\xi e^{-ny}, \quad (2.37)$$

which we use to expand ψ_1 as

$$\psi_1 = \varepsilon \psi_1^{(1)} + \varepsilon^2 \psi_1^{(2)} + \dots \quad (2.38)$$

with

$$\psi_1^{(m)} = -U^{(m)} y + V_1^{(m)} + \dots + V_m^{(m)}. \quad (2.39)$$

Similarly, in the second domain expand ψ_2 as

$$\psi_2 = \varepsilon \psi_2^{(1)} + \varepsilon^2 \psi_2^{(2)} + \dots \quad (2.40)$$

$$\psi_2^{(m)} = W_1^{(m)} + \dots + W_m^{(m)} + \chi^{(m)} y^2 + \eta^{(m)} y, \quad (2.41)$$

where W_n is the general periodic solution for to the biharmonic equation in a finite domain obtained by separation of variables

$$W_n = [(A_n y + B_n) \sin n\xi + (C_n y + D_n) \cos n\xi] \sinh ny \\ + [(E_n y + F_n) \sin n\xi + (G_n y + H_n) \cos n\xi] \cosh ny. \quad (2.42)$$

Expanding the boundary conditions around $y = 0$, I obtain at first order

$$(on\ sheet) \quad \frac{\partial \psi_2^{(1)}}{\partial y}(x, 0) = 0, \frac{\partial \psi_2^{(1)}}{\partial x}(x, 0) = -\cos \xi \quad (2.43a)$$

$$(on\ interface) \quad \frac{\partial \psi_1^{(1)}}{\partial y}(x, \bar{h}) = \frac{\partial \psi_2^{(1)}}{\partial y}(x, \bar{h}), \frac{\partial \psi_1^{(1)}}{\partial x}(x, \bar{h}) = \frac{\partial \psi_2^{(1)}}{\partial x}(x, \bar{h}) = 0 \quad (2.43b)$$

$$\left(\frac{\partial^2 \psi_1^{(1)}}{\partial y^2} - \frac{\partial^2 \psi_1^{(1)}}{\partial x^2} \right) \Big|_{(x, \bar{h})} = \beta \left(\frac{\partial^2 \psi_2^{(1)}}{\partial y^2} - \frac{\partial^2 \psi_2^{(1)}}{\partial x^2} \right) \Big|_{(x, \bar{h})} \quad (2.43c)$$

$$(at\ infinity) \quad \frac{\partial \psi_1^{(1)}}{\partial y}(x, \infty) = -U^{(1)}, \frac{\partial \psi_1^{(1)}}{\partial x}(x, \infty) = 0. \quad (2.43d)$$

Substituting these boundary conditions into the general solution the coefficients at first order are

$$U^{(1)} = \chi^{(1)} = \eta^{(1)} = c_1^{(1)} = d_1^{(1)} = C_1^{(1)} = D_1^{(1)} = 0, \quad (2.44a)$$

$$a_1^{(1)} = \frac{\beta \bar{h} e^{\bar{h}} \sinh \bar{h}}{\sinh^2 \bar{h} - \bar{h}^2 + \beta (\sinh \bar{h} \cosh \bar{h} - \bar{h})}, \quad (2.44b)$$

$$b_1^{(1)} = \frac{-\beta \bar{h}^2 e^{\bar{h}} \sinh \bar{h}}{\sinh^2 \bar{h} - \bar{h}^2 + \beta (\sinh \bar{h} \cosh \bar{h} - \bar{h})}, \quad (2.44c)$$

$$A_1^{(1)} = \frac{\sinh^2 \bar{h} + \beta (\sinh \bar{h} \cosh \bar{h})}{\sinh^2 \bar{h} - \bar{h}^2 + \beta (\sinh \bar{h} \cosh \bar{h} - \bar{h})}, \quad (2.44d)$$

$$B_1^{(1)} = \frac{\sinh \bar{h} \cosh \bar{h} + \bar{h} + \beta \cosh^2 \bar{h}}{\sinh^2 \bar{h} - \bar{h}^2 + \beta (\sinh \bar{h} \cosh \bar{h} - \bar{h})}. \quad (2.44e)$$

At second order, the boundary conditions become

$$(on\ sheet) \quad \frac{\partial \psi_2^{(2)}}{\partial y}(x, 0) + \sin \xi \frac{\partial^2 \psi_2^{(1)}}{\partial y^2}(x, 0) = 0, \quad (2.45a)$$

$$(on\ interface) \quad \frac{\partial \psi_1^{(2)}}{\partial y}(x, \bar{h}) = \frac{\partial \psi_2^{(2)}}{\partial y}(x, \bar{h}), \quad (2.45b)$$

$$\left(\frac{\partial^2 \psi_1^{(2)}}{\partial y^2} - \frac{\partial^2 \psi_1^{(2)}}{\partial x^2} \right) \Big|_{(x, \bar{h})} = \beta \left(\frac{\partial^2 \psi_2^{(2)}}{\partial y^2} - \frac{\partial^2 \psi_2^{(2)}}{\partial x^2} \right) \Big|_{(x, \bar{h})}, \quad (2.45c)$$

leading to the second-order swimming speed as

$$U^{(2)} = -\eta^{(2)} = A_1^{(1)} - \frac{1}{2}, \quad (2.46)$$

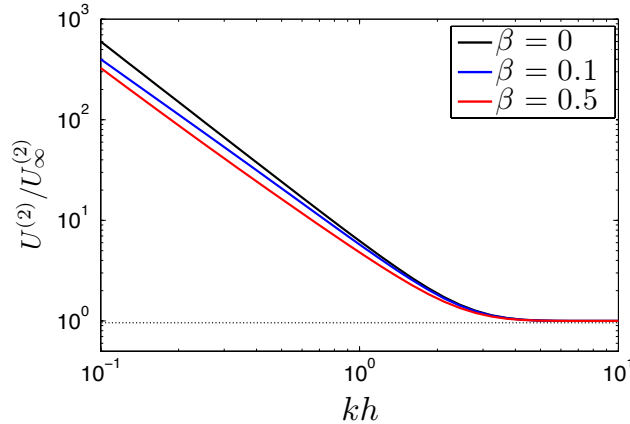


Fig. 2.6 Ratio between the swimming velocity in the two-fluid domain, $U^{(2)}$, and the velocity in the presence of a single fluid, $U_{\infty}^{(2)}$, as a function of the dimensionless distance between the swimmer and the interface, kh , for three values of the viscosity ratio: $\beta = 0, 0.1$ and 0.5 .

and therefore

$$U^{(2)} = \frac{1}{2} + \frac{\bar{h}^2 + \beta \bar{h}}{\sinh^2 \bar{h} - \bar{h}^2 + \beta (\sinh \bar{h} \cosh \bar{h} - \bar{h})}. \quad (2.47)$$

In Eq. (2.47), the first term is the one-fluid classical result of Taylor ($U_{\infty}^{(2)} = 1/2$, recovered when $\bar{h} \rightarrow \infty$) and the second fraction is always positive since $\bar{h} > 0$. As a consequence the swimming speed for a waving sheet in a two-fluid domain is always faster than in a homogeneous Newtonian fluid.

The ratio $U^{(2)}/U_{\infty}^{(2)}$ is displayed in Fig. 2.6 as a function of the dimensionless distance to the interface, kh (i.e. \bar{h}). I observe that the increase of the swimming speed can become very large when the thickness of the low-shear layer is smaller than the wavelength of the swimmer. Also we see that the overall conclusions and speed ratios are rather insensitive to the exact value of the viscosity ratio, β .

2.2.2 Three dimensional waving filament

In this final section, I extend the two-fluid scenario to the case of three-dimensional waving filaments. In this case, the geometry of the cross-section, shown in Fig. 2.7, is analogous to the one addressed in §2.1.2 with the added ingredient that we now have two fluids. The thin, low-viscosity layer, has mean thickness h and dynamic viscosity μ_2 while the bulk has viscosity $\mu_1 > \mu_2$. All other notation are similar to the ones used in §2.1.2.

On the surface of the filament (dimensionless form), $\mathbf{r}_s = (\delta + \bar{\rho} \cos \theta) \mathbf{x} + \bar{\rho} \sin \theta \mathbf{y} + z \mathbf{z}$, the distribution of surface velocities is $\mathbf{u}_2(\delta + \bar{\rho} \cos \theta, \theta, z) = \varepsilon \cos s \mathbf{x}$, which can be written

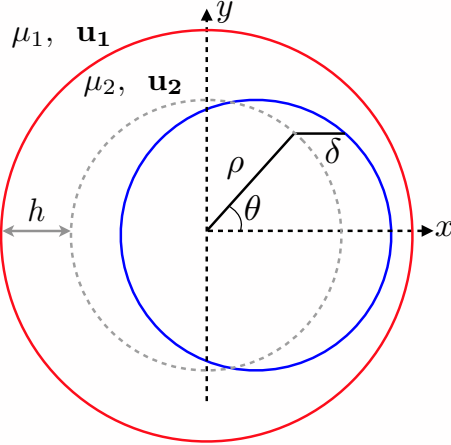


Fig. 2.7 Waving motion of amplitude δ in the circular cross-section of a three-dimensional waving filament of radius ρ in a two-fluid domain. The solid blue line (inside) indicates the instantaneous position of the filament, the dashed gray line the average location of the cross section, while the solid red line (outside) shows the interface between the thin low-viscosity layer (mean thickness h ; dynamic viscosity μ_2) and the bulk fluid ($\mu_1 > \mu_2$).

in polar coordinates as

$$u_2(\delta + \bar{\rho} \cos \theta, \theta, z) = \varepsilon \cos \theta \cos s, \quad v_2(\delta + \bar{\rho} \cos \theta, \theta, z) = -\varepsilon \sin \theta \cos s. \quad (2.48)$$

Expanding the velocity components around the averaged position of the surface Eq. (2.21), at first order

$$u_2^{(1)}(\bar{\rho}, \theta, z) = \cos \theta \cos s, \quad v_2^{(1)}(\bar{\rho}, \theta, z) = -\sin \theta \cos s, \quad w_2^{(1)}(\bar{\rho}, \theta, z) = 0. \quad (2.49)$$

I assume that the interface $r = \bar{h} + \bar{\rho} \equiv l$ undergoes no radial motion and apply continuity of the tangential components of velocities and traction leading to the conditions

$$u_1^{(1)}(l, \theta, z) = u_2^{(1)}(l, \theta, z) = 0, \quad (2.50a)$$

$$v_1^{(1)}(l, \theta, z) = v_2^{(1)}(l, \theta, z), \quad w_1^{(1)}(l, \theta, z) = w_2^{(1)}(l, \theta, z), \quad (2.50b)$$

$$\left. \left(\frac{\partial w_1^{(1)}}{\partial r} + \frac{\partial u_1^{(1)}}{\partial z} \right) \right|_{r=l} = \beta \left. \left(\frac{\partial w_2^{(1)}}{\partial r} + \frac{\partial u_2^{(1)}}{\partial z} \right) \right|_{r=l}, \quad (2.50c)$$

$$\left. \left[r \frac{\partial(v_1^{(1)}/r)}{\partial r} + \frac{1}{r} \frac{\partial u_1^{(1)}}{\partial \theta} \right] \right|_{r=l} = \beta \left. \left[r \frac{\partial(v_2^{(1)}/r)}{\partial r} + \frac{1}{r} \frac{\partial u_2^{(1)}}{\partial \theta} \right] \right|_{r=l}, \quad (2.50d)$$

where, as in §2.2.1, β denotes the ratio of viscosity, $\beta = \mu_2/\mu_1 < 1$.

Using separation of variables,

$$u_1^{(1)} = u_{1q}(r) \cos \theta \cos s, \quad v_1^{(1)} = v_{1q}(r) \sin \theta \cos s, \quad w_1^{(1)} = w_{1q}(r) \cos \theta \sin s, \quad (2.51a)$$

$$u_2^{(1)} = u_{2q}(r) \cos \theta \cos s, \quad v_2^{(1)} = v_{2q}(r) \sin \theta \cos s, \quad w_2^{(1)} = w_{2q}(r) \cos \theta \sin s, \quad (2.51b)$$

and substituting Eq. (2.51) into the Eq. (2.50), the boundary conditions become

$$u_{2q}(\bar{\rho}) = 1, \quad v_{2q}(\bar{\rho}) = -1, \quad w_{2q}(\bar{\rho}) = 0, \quad (2.52a)$$

$$u_{1q}(l) = u_{2q}(l) = 0, \quad v_{1q}(l) = v_{2q}(l), \quad w_{1q}(l) = w_{2q}(l), \quad (2.52b)$$

$$w'_{1q}(l) - u_{1q}(l) = \beta [w'_{2q}(l) - u_{2q}(l)], \quad (2.52c)$$

$$v'_{1q}(l) - \frac{v_{1q}(l)}{l} - \frac{u_{1q}(l)}{l} = \beta \left[v'_{2q}(l) - \frac{v_{2q}(l)}{l} - \frac{u_{2q}(l)}{l} \right]. \quad (2.52d)$$

Then using the general solution in Eq. (2.26), with coefficients A_1, B_1, C_1 for fluid #1, ensuring the correct decay in the far field, and coefficients A_2, B_2, C_2, D, E, F for fluid #2.

Substituting this general solution into the boundary conditions in Eq. (2.52), a linear system with 9 coefficients is,

$$\bar{\rho}K_1(\bar{\rho})A_2 + K_2(\bar{\rho})B_2 + K_0(\bar{\rho})C_2 + \bar{\rho}I_1(\bar{\rho})D + I_2(\bar{\rho})E + I_0(\bar{\rho})F = 1, \quad (2.53a)$$

$$K_2(\bar{\rho})B_2 - K_0(\bar{\rho})C_2 + I_2(\bar{\rho})E - I_0(\bar{\rho})F = -1, \quad (2.53b)$$

$$[\bar{\rho}K_0(\bar{\rho}) - K_1(\bar{\rho})]A_2 + K_1(\bar{\rho})B_2 + K_1(\bar{\rho})C_2 - [\bar{\rho}I_0(\bar{\rho}) + I_1(\bar{\rho})]D \\ - I_1(\bar{\rho})E - I_1(\bar{\rho})F = 0, \quad (2.53c)$$

$$lK_1(l)A_1 + K_2(l)B_1 + K_0(l)C_1 = 0, \quad (2.53d)$$

$$lK_1(l)A_2 + K_2(l)B_2 + K_0(l)C_2 + lI_1(l)D + I_2(l)E + I_0(l)F = 0, \quad (2.53e)$$

$$K_2(l)B_1 - K_0(l)C_1 - K_2(l)B_2 + K_0(l)C_2 - I_2(l)E + I_0(l)F = 0, \quad (2.53f)$$

$$[lK_0(l) - K_1(l)]A_1 + K_1(l)B_1 + K_1(l)C_1 - [lK_0(l) - K_1(l)]A_2 - K_1(l)B_2 - K_1(l)C_2 \\ + [lI_0(l) + I_1(l)]D + I_1(l)E + I_1(l)F = 0, \quad (2.53g)$$

$$\left[2K_0(l) - 2lK_1(l) + \frac{K_1(l)}{l} \right] A_1 + \left[\frac{K_1(l)}{l} - 2K_2(l) \right] B_1 - \left[2K_0(l) - \frac{K_1(l)}{l} \right] C_1 \\ - \beta \left[2K_2(l) - 2lK_1(l) + \frac{K_1(l)}{l} \right] A_2 - \beta \left[\frac{K_1(l)}{l} - 2K_2(l) \right] + \beta \left[2K_0(l) + \frac{K_1(l)}{l} \right] C_2 \\ + \beta \left[2I_0(l) + 2lI_1(l) - \frac{I_1(l)}{l} \right] D + \beta \left[\frac{I_1(l)}{l} + 2I_2(l) \right] E + \beta \left[2I_0(l) - \frac{I_1(l)}{l} \right] F = 0, \quad (2.53h) \\ - K_1(l)A_1 - K_3(l)B_1 + K_1(l)C_1 + \beta [K_1(l)A_2 + K_3(l)B_2 - K_1(l)C_2 \\ + I_1(l)D - I_3(l)E + I_1(l)F] = 0, \quad (2.53i)$$

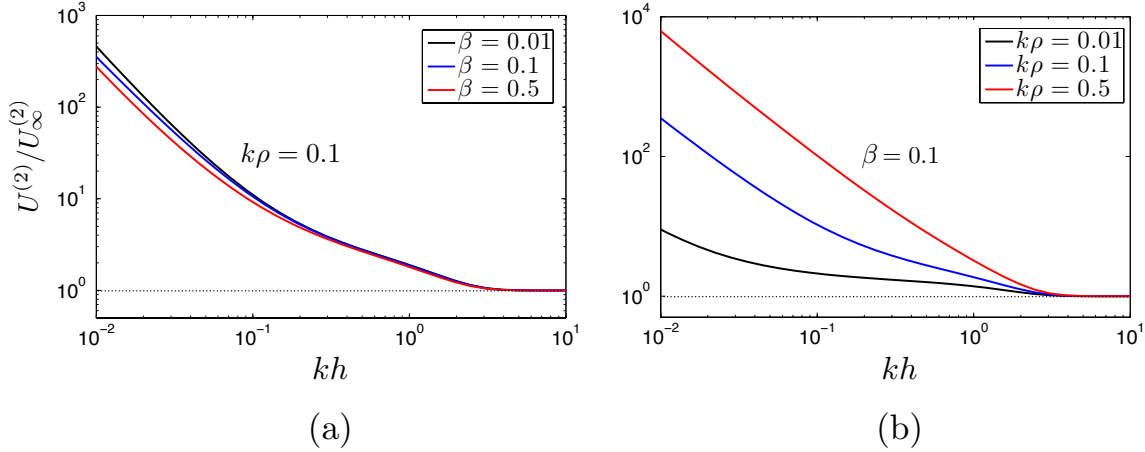


Fig. 2.8 Ratio between the swimming velocity in the two-fluid domain, $U^{(2)}$, and that obtained in the case of a single Newtonian fluid, $U_\infty^{(2)}$, as a function of the mean dimensionless distance between the cylindrical filament and the fluid interface, kh ; (a): the dimensionless radius is fixed, $k\rho = 0.1$, and three values of viscosity ratios are considered ($\beta = 0.01, 0.1$ and 0.5); (b): fixed viscosity ratio ($\beta = 0.1$), and three different values of dimensionless radius ($k\rho = 0.01, 0.1$ and 0.5).

which can be easily inverted numerically.

The last step consists in moving to next order and computing the swimming speed. This is done similarly to the case with a finite slip length, and we apply Eq. (2.30) with $\Lambda = 0$. The average of $w_2^{(2)}$ on the filament is the swimming speed, $U^{(2)}$, is

$$U^{(2)} = \frac{1}{4} \left[w'_{2q}(\bar{\rho}) + \frac{w_{2q}(\bar{\rho})}{\bar{\rho}} \right], \quad (2.54)$$

which can be evaluated as

$$\begin{aligned} U^{(2)} = & \frac{1}{4} \left\{ -B_2 K_0(\bar{\rho}) - C_2 K_0(\bar{\rho}) + A_2 [3K_0(\bar{\rho}) - \bar{\rho} K_1(\bar{\rho})] \right. \\ & \left. - EI_0(\bar{\rho}) - FI_0(\bar{\rho}) - D [3I_0(\bar{\rho}) + \bar{\rho} I_1(\bar{\rho})] \right\}. \end{aligned} \quad (2.55)$$

In Fig. 2.8 I plot the ratio between the swimming speed of the filament in the two-fluid domain, $U^{(2)}$, and that obtained in the case of a simple fluid, $U_\infty^{(2)}$, for a range of values of the dimensionless radius ($k\rho$, i.e. $\bar{\rho}$) and viscosity ratio (β). The results are reminiscent of the ones shown in Fig. 2.6 for the two-dimensional case. The swimming speed is always increased by the presence of a second fluid, potentially by order of magnitude when the wavelength of the swimmer and its radius are large compared to the thickness of the low-viscosity layer.

2.3 Discussion

In this chapter, I presented a physical mechanism for the locomotion enhancement of microscopic swimmers in a complex fluid. The physical idea is that phase-separation near the surface of the swimmer leads to the presence of a low viscosity layer which promotes slip and decreases viscous friction. As a way to intuitively rationalize the results in our paper, we note – as is well known – that the locomotion in a fluid is governed by the ratio between the drag coefficients for the motion relative to the fluid perpendicular to and along the surface of the swimmer [83]. The presence of a fluidic interface, or of a finite slip length, affects normal hydrodynamic forces only weakly but leads to a systematic decrease of tangential viscous forces, and hence should always lead to faster swimming, as observed here. In a different context, but with some physical similarities, swimmers also always enhance their swimming speed in a network of polymer molecules [97] and in a porous medium [87].

Beyond the traditional geometrical assumptions made in this work which are similar to a number of classical studies (namely solving the swimming problems for small amplitude motion and perfectly sinusoidal waveforms), one severe restriction of our two-fluid approach is the assumption that the interface between the two fluids remains flat. This is akin to saying that the time scale of the waving motion is much faster than the time scale for the readjustment of the interface, which is a reasonable assumption only for large fluid viscosities. That flat interface then provides an effective confinement to the swimmer, which is known to enhance locomotion [113]. A more sophisticated physicochemical model including molecular details of the phase separation would be required to solve for the dynamics of the thin film and to untangle the relative importance of viscosity difference vs. confinement in the increase of the swimming speed.

What are the quantitative predictions of our models? In two dimensions, the speed of a two-dimensional infinite swimming sheet is increased by $1 + 2k\Lambda$ for the swimming with wave number k . Slip lengths of polymer solutions, Λ , have been measured in the range $0.1 - 10 \mu\text{m}$ [101]. For a microswimmer with wavelength $\lambda = 2\pi/k \approx 10 \mu\text{m}$ [83], the swimming speed can then be increased by $O(10\%)$ up to by one order of magnitude. In the three-dimensional case, I also obtained the increased speed shown in Fig. 2.4, which is consistent with the two-dimensional situation. Considering the same wavelength, and for a filament with radius $\rho = 150 \text{ nm}$ (so with dimensionless radius $k\rho \approx 0.1$), the predicted enhancement ranges from $O(30\%)$ up to by forty times of the speed in the Newtonian fluid.

In the second model, I used a two-fluids domain to describe wall depletion. In both two- and three-dimensions, when the wall depletion layer is very thin, the enhancement can be very large. A recent experiment by Gagnon, Shen and Arratia [46] considered the locomotion of the nematode *C. elegans* in concentrated polymer solutions and showed that the swimming

speed can be increased significantly, by up to 65%. Is my model consistent with this result? The thickness of the low-viscosity layer in concentrated polymer solutions is a complex function of mean diameter of the particles and the concentration but can be estimated using the empirical formula [66]

$$\frac{h}{D_p} = 1 - \frac{\phi}{\phi_m}, \quad (2.56)$$

where D_p is the mean diameter of the particles, ϕ the particle volume fraction, and ϕ_m the maximum packing fraction. The diameter of the particle (Xanthan gum in the experiment of Ref. [46]) is about 200 μm . For semi-concentrated solution, ϕ/ϕ_m is 0.4, while for a concentrated solution the value is 0.8, so the slip layer thickness is around 120 μm and 40 μm respectively. The wavelength of the swimming worm is $2\pi/k \approx 1 \text{ mm}$, and the dimensionless diameter $k\rho$ is about 0.1. When the ratio of the viscosities β changes from 0.01 to 0.5, the enhancement predicted by our model is about 90 – 98%, which is less than a factor of two away from the experimental results, and indicates that our simplified approach captures the essential physics of the swimming enhancement.

Chapter 3

Slip slender-body theory

Although the swimming sheet model is simple enough, it is still not very realistic for its limitation of small deformation. People thus think about the geometry that can more generally represent biological structures including the flagellar filaments, cilia, microtubules, etc. By observing all these shapes, it is natural to consider a slender geometry that the character length L is much larger than the breadth a . Solving the flow disturbed by an arbitrary slender body would not be trivia. We know that the analytical solution of Stokes equation can be derived only in a few situations. For example Stokes calculated the problem that an isolated sphere translating in a viscous fluid [126], and Oberbeck extended the problem to the spheroid case [104], which can give the solution for a special case of slender body with straight centerline.

However, the idea of slender-body theory (SBT) allowed us calculate the flow asymptotically. The idea is came up with by Hancock [59] stating that taking advantage of slenderness ($a \ll L$), the flow induced by the translating motion is asymptotically the same as that due to an appropriate line distribution of Stokelets. Stokeslet represents the flow induced by a single point force [59, 73, 55]. Using this idea, Hancock and Gray introduced resistive force theory (RFT) which states that the local force is proportional with the local velocity [59, 53]. If considering directions tangential and perpendicular with the body, mathematically RFT is described as

$$f_{\parallel} = -\xi_{\parallel} u_{\parallel}, \quad f_{\perp} = -\xi_{\perp} u_{\perp}, \quad (3.1)$$

where $\xi_{\parallel, \perp}$ are local drag coefficients asymptotically satisfies

$$\xi_{\perp} \approx 2\xi_{\parallel}. \quad (3.2)$$

This relation illustrates the physical origin that triggers swimming at low Reynolds number. The anisotropy in drag allows the body to create force not align with the direction of

movement, which leads to the possibility to generate non-zero time-averaged propulsion [82]. Flowing this idea, more systematical methods of SBT were vigorously developed during 1970's [8, 31, 131, 70, 47, 65, 88]. Here we review two important methods illustrated by Cox and Lighthill.

Cox solved the flow by matching the inner solution that is close to the filament and the outer solution far away from it. Inner solution is locally the two dimensional flow induced by a cylinder, which diverges logarithmically according to Stokes' paradox [85], while outer solution is the flow induced by a line distribution of Stokeslets and Dipoles which diverges as $1/r$. Comparing the forms of inner and outer solution, the full solution is expanded logarithmically as the order of $\ln(L/a)$ and can be systematically derived order by order.

Since Cox's SBT gives the series solution that converges logarithmically, which is slow, more terms are necessary to be included for accurate result. Another method which is less rigorous but easier to implement is provided by Lighthill. He measured the flow at each point by separating the filament into a local region around that point with length scale of $2q$ satisfying $a \ll q \ll L$ and a non-local region outside. In the local region, the flow is induced by both stokeslets and dipoles, while in the non-local region, it is stokeslets only. This set-up is intuitively correct since dipoles decay as r^{-2} which is much faster than stokeslets. By adding up the local and non-local results, the velocity of the centerline is independent with the choices of this intermediate length q , which is described as

$$\mathbf{U}(s) = \frac{\mathbf{f}_\perp}{4\pi\mu} + \frac{1}{8\pi\mu} \int_{|\Delta|>a\sqrt{e}/2} \mathbf{f} \cdot \left(\frac{\mathbf{I}}{R} + \frac{\mathbf{R}\mathbf{R}}{R^3} \right) d\Delta. \quad (3.3)$$

\mathbf{f} is the local strength of stokeslets and \mathbf{f}_\perp is its normal component. Comparing to the expansion of logarithmic terms, his formulation is easier to implement to numerics, though it is only valid to order of $\sqrt{a/L}$ [82].

All of these classical results illustrated above are valid for no-slip boundary condition. To study the locomotion in some complex environments with slip effect, discussions of the situations with slip boundary condition are thus required. Using Navier slip boundary condition as explained in the previous chapter, the study of slip was initiated from a sphere, with which the drag coefficient was calculated theoretically by Basset [1]. When it comes to spheroid or ellipsoid, the derivation becomes less straightforward than those for no-slip cases, leading to numerical measurements of resistant coefficients for rotation [62, 142, 26] and translation motion [69, 25]. Recently, Sherwood theoretically studied the geometry of a disk with zero thickness [117].

In this chapter I analytically derive the classical results of resistant coefficients and SBT with Navier slip boundary condition. In §3.1 I first calculate the flow through asymptotic

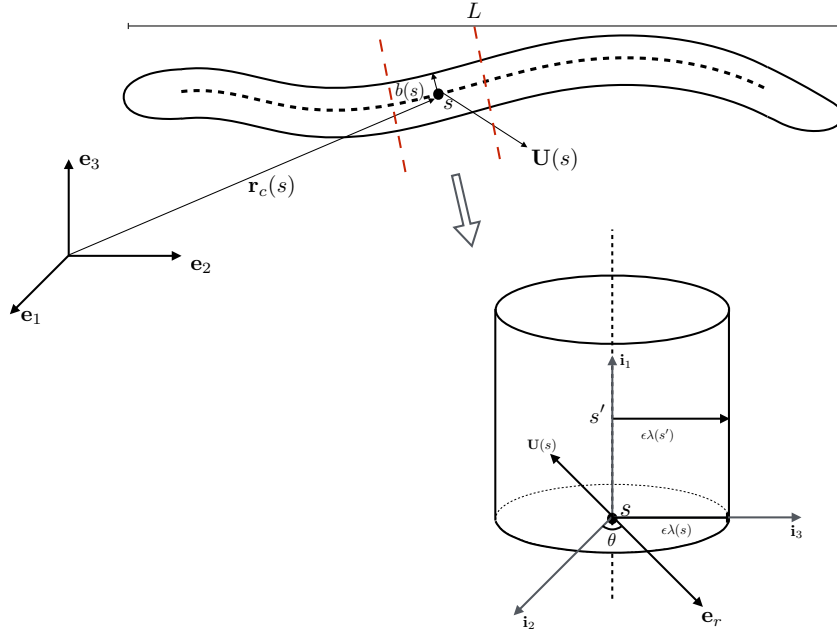


Fig. 3.1 Geometry of slender body, with total length L , and radius $b(s)$ changing along the centerline $\mathbf{r}_c(s)$. The centerline moves with velocity $\mathbf{U}(s)$. Two frames are defined in this set-up; \mathbf{e}_j is the cartesian coordinate and \mathbf{i}_j is the local cartesian coordinate. The small number ϵ is defined as the ratio of the breadth to length b/L , λ is the local radius rescaled by ϵ .

expansion in logarithms, and therefore extend Cox's SBT to slip case. Then in §3.2, I move back to a simpler geometry of a straight rod and calculate the tangential and normal resistant coefficients of translating motions. Next in §3.3 I follow Lighthill's method and derive an easily implemented form of SBT. At last in §3.4, I compare my results with the numerical evaluations [69, 25] and demonstrate a good agreement in between.

3.1 Asymptotic expansion in logarithms

3.1.1 Set-up

I consider a slender body with centerline $\mathbf{r}_c(s)$, s is the arc length. Let us assume the cross section of the body is circular, with radius $b(s)$ changing with arc length. The total length is L , which is much larger than the radius $L \ll b$. The geometry is shown in FIG. 3.1. If the radial direction is \mathbf{e}_r , the surface of the body is described as

$$\mathbf{r}_c(s) + b(s)\mathbf{e}_r(s). \quad (3.4)$$

The centerline translates with velocity $\mathbf{U}(s)$, which induces the flow field \mathbf{u} that satisfies Stokes equation

$$\mu \nabla^2 \mathbf{u} = \nabla p, \quad \nabla \cdot \mathbf{u} = 0. \quad (3.5)$$

On the filament surface, Navier's slip boundary condition [102] is applied, with which the normal velocity is continuous with that of the surface, while the tangential velocity has a jump proportional to stress. The proportional coefficient is slip length Λ depending on the flow environment and the surface material. For example, in polymer solutions, slip length has been measured in the range $0.1 - 10 \mu\text{m}$, which is also affected by the concentration [101]. Here I assume Λ is constant and the mathematical description of the boundary condition is

$$\mathbf{u}(\mathbf{r} = \mathbf{r}_c + b\mathbf{e}_r) = \mathbf{U} + 2\Lambda(\mathbf{I} - \mathbf{e}_r\mathbf{e}_r) \cdot \mathbf{E} \cdot \mathbf{e}_r, \quad (3.6)$$

where \mathbf{E} is the strain rate evaluated near the surface. According to the slenderness assumption $b \ll L$, I define a small number ε which is the aspect ratio of the body

$$\varepsilon = b_0/L, \quad (3.7)$$

where b_0 is the characteristic radius (for example we can choose the maximum radius along the centerline).

Next let us nondimensionalise variables with length scale L and characteristic velocity U_0 (magnitude of the disturbance velocity).

$$s = L\bar{s}, \quad b = L\varepsilon\lambda, \quad \mathbf{U} = U_0\bar{\mathbf{U}}, \quad p = \frac{\mu U_0}{L}\bar{p}, \quad \Lambda = L\bar{\Lambda}, \quad (3.8)$$

where $\lambda(s)$ is the rescaled radius of unit order. Substitute dimensionless variables into Eq. 3.5 and 3.6, equations becomes

$$\bar{\nabla}^2 \bar{\mathbf{u}} = \bar{\nabla} \bar{p}, \quad \bar{\nabla} \cdot \bar{\mathbf{u}} = \mathbf{0}. \quad (3.9)$$

with boundary condition

$$\bar{\mathbf{u}}(\bar{\mathbf{r}} = \bar{\mathbf{r}}_c + \varepsilon\lambda\mathbf{e}_r) = \bar{\mathbf{U}} + 2\bar{\Lambda}(\mathbf{I} - \mathbf{e}_r\mathbf{e}_r) \cdot \bar{\mathbf{E}} \cdot \mathbf{e}_r \quad (3.10a)$$

$$\bar{\mathbf{u}}(\bar{r} = \infty) = \mathbf{0}. \quad (3.10b)$$

For convenience, we drop off all the 'bars', following calculations will be all in dimensionless form.

3.1.2 Inner solution

First I consider the flow close the filament at point s , which is locally two dimensional flow induced by a cylinder. As shown in FIG. 3.1, I first build a local Cartesian frame $[\mathbf{i}_1, \mathbf{i}_2, \mathbf{i}_3]$, where \mathbf{i}_1 is the direction alone the axis and \mathbf{i}_2 is chosen in the plane expanded by \mathbf{i}_1 and \mathbf{U} . This assumption is only for the purpose of simplifying the calculation, with which \mathbf{U} only has two components which can be written as

$$\mathbf{U}(s) = U_1 \mathbf{i}_1 + U_2 \mathbf{i}_2. \quad (3.11)$$

Another local frame needed is the cylindrical coordinates $[\mathbf{e}_r, \mathbf{e}_\theta, \mathbf{e}_z]$, where $\mathbf{e}_z = \mathbf{i}_1$. Along the center, the radius changes as the order of ε , so first we expand the flow in orders of ε ,

$$\mathbf{u} = \mathbf{u}^{(0)} + \varepsilon \mathbf{u}^{(1)} + \dots \quad (3.12a)$$

$$p = p^{(0)} + \varepsilon p^{(1)} + \dots \quad (3.12b)$$

Substitute into Eq. 3.9, the leading order equation is

$$\nabla^2 \mathbf{u}^{(0)} = \nabla p^{(0)}, \quad \nabla \cdot \mathbf{u}^{(0)} = \mathbf{0}. \quad (3.13)$$

Then I introduce a position vector relative to the centerline $\hat{\mathbf{r}}$,

$$\hat{\mathbf{r}} = \mathbf{r} - \mathbf{r}_c(s'), \quad (3.14)$$

substitute it into Eq. 3.10, the surface is represented by $\hat{\mathbf{r}} = \varepsilon \lambda \mathbf{e}_r$ and the boundary condition becomes

$$\mathbf{u}(\hat{\mathbf{r}} = \varepsilon \lambda(s') \mathbf{e}_r) = \mathbf{U}(s') + 2\Lambda [\mathbf{I} - \mathbf{e}_r(s') \mathbf{e}_r(s')] \cdot \mathbf{E}(s') \cdot \mathbf{e}_r(s') \quad (3.15)$$

Note that I use s' to denote an arbitrary point at centerline while s is the fixed point at which I need to derive the flow. Since the body is long and slender, it is not surprising to assume that the variables change slowly along the centerline, with the variation same order of the length. With this assumption, the variables including the radius λ , velocity \mathbf{U} , strain rate \mathbf{E}

and the radial direction \mathbf{e}_r can be Taylor-expanded around point s ,

$$\lambda(s') = \lambda(s) + O(\varepsilon), \quad (3.16a)$$

$$\mathbf{U}(s') = \mathbf{U}(s) + O(\varepsilon), \quad (3.16b)$$

$$\mathbf{E}(s') = \mathbf{E}(s) + O(\varepsilon), \quad (3.16c)$$

$$\mathbf{e}_r(s') = \mathbf{e}_r(s) + O(\varepsilon). \quad (3.16d)$$

Substitute into Eq. 3.15, the leading order of the boundary condition is

$$\mathbf{u}^{(0)}(\varepsilon\lambda(s), \theta, s') = \mathbf{U}(s) + 2\Lambda[\mathbf{I} - \mathbf{e}_r(s)\mathbf{e}_r(s)] \cdot \mathbf{E}^{(0)}(s) \cdot \mathbf{e}_r(s), \quad (3.17)$$

writing it in cylindrical coordinates

$$u_r^{(0)}(\varepsilon\lambda(s), \theta, s') = U_2 \cos \theta, \quad (3.18a)$$

$$u_\theta^{(0)}(\varepsilon\lambda(s), \theta, s') = -U_2 \sin \theta + \Lambda \left[r \frac{\partial}{\partial r} \left(\frac{u_\theta^{(0)}}{r} \right) + \frac{1}{r} \frac{\partial u_r^{(0)}}{\partial \theta} \right], \quad (3.18b)$$

$$u_z^{(0)}(\varepsilon\lambda(s), \theta, s') = U_1 + \Lambda \left[\frac{\partial u_z^{(0)}}{\partial r} + \frac{\partial u_r^{(0)}}{\partial z} \right]. \quad (3.18c)$$

Since $u_i^{(0)}$ are assumed as the same order while r is order of ε , so that we claim the strain rate along the radial direction should be much larger than that in axial direction, which is

$$\frac{\partial u_r^{(0)}}{\partial z} \ll \frac{\partial u_z^{(0)}}{\partial r}. \quad (3.19)$$

Using this relation the boundary condition can be further simplified to

$$u_r^{(0)}(\varepsilon\lambda(s), \theta, s') = U_2 \cos \theta, \quad (3.20a)$$

$$u_\theta^{(0)}(\varepsilon\lambda(s), \theta, s') = -U_2 \sin \theta + \Lambda \left[r \frac{\partial}{\partial r} \left(\frac{u_\theta^{(0)}}{r} \right) + \frac{1}{r} \frac{\partial u_r^{(0)}}{\partial \theta} \right], \quad (3.20b)$$

$$u_z^{(0)}(\varepsilon\lambda(s), \theta, s') = U_1 + \Lambda \frac{\partial u_z^{(0)}}{\partial r}. \quad (3.20c)$$

Next let us consider the conservation equation that $\nabla \mathbf{u}^{(0)} = 0$. Since $\frac{\partial u_z^{(0)}}{\partial z} \ll \frac{\partial u_r^{(0)}}{\partial r}$, the term related to z can be neglected so that the stream function ψ is introduced as

$$u_r^{(0)} = \frac{1}{r} \frac{\partial \psi}{\partial \theta}, \quad u_\theta^{(0)} = -\frac{\partial \psi}{\partial r}. \quad (3.21)$$

Substitute into $\nabla \mathbf{u}^{(0)} = 0$, ψ satisfies a biharmonic equation that

$$\nabla^4 \psi = 0. \quad (3.22)$$

Considering the boundary condition at infinity in Eq. 3.10(b) the solution is assumed with form [31]

$$\psi(r, \theta) = (Ar \ln r + Br + Cr^{-1}) \sin \theta + (\alpha r \ln r + \beta r + \gamma r^{-1}) \cos \theta, \quad (3.23)$$

where A, B, C, α, β and γ are constant coefficients. Substitute into Eq. 3.21, the flow field is

$$u_r^{(0)} = (A \ln r + B + Cr^{-2}) \cos \theta - (\alpha \ln r + \beta + \gamma r^{-2}) \sin \theta, \quad (3.24a)$$

$$u_\theta^{(0)} = -[A(\ln r + 1) + B - Cr^{-2}] \sin \theta - [\alpha(\ln r + 1) + \beta - \gamma r^{-2}] \cos \theta. \quad (3.24b)$$

And we calculate the strain rate $\mathbf{E}^{(0)}$ with components

$$r \frac{\partial}{\partial r} \left(\frac{u_\theta^{(0)}}{r} \right) = (Ar^{-1} \ln r + Br^{-1} - 3Cr^{-3}) \sin \theta, \quad (3.25a)$$

$$+ (\alpha r^{-1} \ln r + \beta r^{-1} - 3\gamma r^{-3}) \cos \theta, \quad (3.25b)$$

$$\frac{1}{r} \frac{\partial u_r^{(0)}}{\partial \theta} = -(Ar^{-1} \ln r + Br^{-1} + Cr^{-3}) \sin \theta \quad (3.25c)$$

$$- (\alpha r^{-1} \ln r + \beta r^{-1} + \gamma r^{-3}) \cos \theta. \quad (3.25d)$$

Substitute Eq. 3.24 and 3.25 into Eq. 3.20(a)(b), we obtain a linear system of coefficients A, B, C, α, β and γ ,

$$A \ln \varepsilon \lambda + B + C(\varepsilon \lambda)^{-2} = U_2, \quad (3.26a)$$

$$\alpha \ln \varepsilon \lambda + \beta + \gamma(\varepsilon \lambda)^{-2} = 0, \quad (3.26b)$$

$$A(\ln \varepsilon \lambda + 1) + B - C(\varepsilon \lambda)^{-2} = U_2 + 4\Lambda C(\varepsilon \lambda)^{-3}, \quad (3.26c)$$

$$\alpha(\ln \varepsilon \lambda + 1) + \beta - \gamma(\varepsilon \lambda)^{-2} = 4\Lambda \gamma(\varepsilon \lambda)^{-3}. \quad (3.26d)$$

Define a ratio

$$\chi = \frac{\varepsilon\lambda}{2(\varepsilon\lambda + 2\Lambda)}, \quad (3.27)$$

and solve the system by canceling A and α , other coefficients are

$$B = U_2 - (\ln \varepsilon\lambda + \chi)A, \quad (3.28a)$$

$$C = (\varepsilon\lambda)^2 \chi A, \quad (3.28b)$$

$$\beta = -(\ln \varepsilon\lambda + \chi)\alpha, \quad (3.28c)$$

$$\gamma = (\varepsilon\lambda)^2 \chi \alpha. \quad (3.28d)$$

Substitute Eq. 3.28 into Eq. 3.24, the inner flow is

$$\begin{aligned} u_r^{(0)} &= A \left[\ln \frac{r}{\varepsilon\lambda} - \chi + \chi(\varepsilon\lambda)^2 r^{-2} \right] \cos \theta \\ &\quad - \alpha \left[\ln \frac{r}{\varepsilon\lambda} - \chi + \chi(\varepsilon\lambda)^2 r^{-2} \right] \sin \theta + U_2 \cos \theta, \end{aligned} \quad (3.29a)$$

$$\begin{aligned} u_\theta^{(0)} &= -A \left[\ln \frac{r}{\varepsilon\lambda} + 1 - \chi - \chi(\varepsilon\lambda)^2 r^{-2} \right] \sin \theta \\ &\quad - \alpha \left[\ln \frac{r}{\varepsilon\lambda} + 1 - \chi - \chi(\varepsilon\lambda)^2 r^{-2} \right] \cos \theta - U_2 \sin \theta. \end{aligned} \quad (3.29b)$$

We still need to calculate the axial velocity u_z which satisfies

$$\nabla^2 u_z = \frac{1}{\mu} \frac{\partial p}{\partial z}. \quad (3.30)$$

Since $\frac{\partial p}{\partial z} \ll \frac{\partial p}{\partial r}$, the right hand side can be treated as zero and $u_z^{(0)}$ satisfies a harmonic equation. If we separate the motion into a normal motion and an axisymmetric motion. As the normal motion leads to zero velocity on z direction, $u_z^{(0)}$ should only be contributed by axisymmetric motion, and the axial velocity is only a function of r . Combing all these conditions, the axial component has the form

$$u_z^{(0)} = D \ln r + E, \quad (3.31)$$

Where D and E are new coefficients relating to axial field. Substitute Eq. 3.31 back to boundary condition along the axial direction in Eq. 3.20(c), $u_z^{(0)}$ is solved as

$$u_z^{(0)} = D \left(\ln \frac{r}{\varepsilon\lambda} + \frac{\Lambda}{\varepsilon\lambda} \right) + U_1. \quad (3.32)$$

Finally I have three coefficients A , α and D . Observing the form of solution, the singular terms diverge logarithmically near the filament, which is consistent with the argument of two dimensional flow. The form of inner solution naturally leads to the expansion in logarithms. The coefficients are thus expanded as orders of $1/\ln \varepsilon$,

$$A = \frac{A^{(1)}}{\ln \varepsilon} + \frac{A^{(2)}}{\ln^2 \varepsilon} + \dots \quad (3.33a)$$

$$\alpha = \frac{\alpha^{(1)}}{\ln \varepsilon} + \frac{\alpha^{(2)}}{\ln^2 \varepsilon} + \dots \quad (3.33b)$$

$$D = \frac{D^{(1)}}{\ln \varepsilon} + \frac{D^{(2)}}{\ln^2 \varepsilon} + \dots \quad (3.33c)$$

Also let us expand $\mathbf{u}^{(0)}$ as

$$u_r^{(0)} = u_r^{(00)} + \frac{1}{\ln \varepsilon} u_r^{(01)} + \dots \quad (3.34a)$$

$$u_\theta^{(0)} = u_\theta^{(00)} + \frac{1}{\ln \varepsilon} u_\theta^{(01)} + \dots \quad (3.34b)$$

$$u_z^{(0)} = u_z^{(00)} + \frac{1}{\ln \varepsilon} u_z^{(01)} + \dots \quad (3.34c)$$

Substitute Eq. 3.33 and 3.34 into Eq. 3.29 and 3.32, the leading order of the flow is solved as

$$u_r^{(00)} = -[A^{(1)} - U_2] \cos \theta + \alpha^{(1)} \sin \theta, \quad (3.35a)$$

$$u_\theta^{(00)} = [A^{(1)} - U_2] \sin \theta + \alpha^{(1)} \cos \theta, \quad (3.35b)$$

$$u_z^{(00)} = -D^{(1)} + U_1. \quad (3.35c)$$

Next order solution ($O(1/\ln \varepsilon)$) is

$$u_r^{(01)} = \left[A^{(1)} \left(\ln \frac{r}{\lambda} - \chi \right) - A^{(2)} \right] \cos \theta - \left[\alpha^{(1)} \left(\ln \frac{r}{\lambda} - \chi \right) - \alpha^{(2)} \right] \sin \theta, \quad (3.36a)$$

$$u_\theta^{(01)} = - \left[A^{(1)} \left(\ln \frac{r}{\lambda} + 1 - \chi \right) - A^{(2)} \right] \sin \theta - \left[\alpha^{(1)} \left(\ln \frac{r}{\lambda} + 1 - \chi \right) - \alpha^{(2)} \right] \cos \theta, \quad (3.36b)$$

$$u_z^{(01)} = D^{(1)} \left(\ln \frac{r}{\lambda} + \frac{\Lambda}{\varepsilon \lambda} \right) - D^{(2)}. \quad (3.36c)$$

Higher order terms can be derived systematically. Note that the leading order is same as that in Ref. [31], slip length appears in the term of order of $1/\ln \varepsilon$.

3.1.3 Outer solution and matching

Next I consider the flow far away from the body, which is induced by a line of stokeslets. Denote the outer flow $\hat{\mathbf{u}}$, the velocity around point s is

$$\hat{\mathbf{u}}(s) = \frac{1}{8\pi} \int_0^1 \mathbf{f}(s') \cdot \left(\frac{\mathbf{I}}{R} + \frac{\mathbf{R}\mathbf{R}}{R^3} \right) ds', \quad (3.37)$$

where

$$\mathbf{R} = \mathbf{r}(s) + r\mathbf{e}_r(s) - \mathbf{r}(s'), \quad R = |\mathbf{R}|, \quad (3.38)$$

and \mathbf{f} is the point force exerted by the body on the fluid. Now the question is to obtain the force density along the centerline. Before giving the result, we look at the force density and the corresponding induced singular field. For the general form of constant force density

$$\mathbf{f} = f_1 \mathbf{i}_1 + f_2 \mathbf{i}_2 + f_3 \mathbf{i}_3, \quad (3.39)$$

the singular part of the flow would be

$$-\left(\frac{f_1}{2\pi} \mathbf{i}_1 + \frac{f_2}{4\pi} \mathbf{i}_2 + \frac{f_3}{4\pi} \mathbf{i}_3 \right) \ln r. \quad (3.40)$$

I already calculated the flow field in Eq. 3.29 and 3.31, consider the relation between the force and the velocity, the singular part of velocity is

$$(D\mathbf{i}_1 + A\mathbf{i}_2 - \alpha\mathbf{i}_3) \ln r, \quad (3.41)$$

and the corresponding point force density should be

$$\mathbf{f} = -2\pi D\mathbf{i}_1 - 4\pi A\mathbf{i}_2 + 4\pi\alpha\mathbf{i}_3. \quad (3.42)$$

Consider that if the thickness of the filament tends to be zero, the flow field will be undisturbed leading to zero velocity. Matching with Eq. 3.35, coefficients $A^{(1)}$, $\alpha^{(1)}$ and $D^{(1)}$ are evaluated as

$$A^{(1)} = U_2, \quad \alpha^{(1)} = 0, \quad D^{(1)} = U_1. \quad (3.43)$$

Expand $\hat{\mathbf{u}}$ and \mathbf{f} as orders of $\frac{1}{\ln \varepsilon}$,

$$\hat{\mathbf{u}} = \frac{\hat{\mathbf{u}}^{(1)}}{\ln \varepsilon} + \frac{\hat{\mathbf{u}}^{(2)}}{\ln^2 \varepsilon} + \dots \quad (3.44a)$$

$$\mathbf{f} = \frac{\mathbf{f}^{(1)}}{\ln \varepsilon} + \frac{\mathbf{f}^{(2)}}{\ln^2 \varepsilon} + \dots \quad (3.44b)$$

and combine Eq. 3.42 and 3.43, the leading order force density is

$$\mathbf{f}^{(1)} = -2\pi U_1 \mathbf{i}_1 - 4\pi U_2 \mathbf{i}_2. \quad (3.45)$$

Substitute Eq. 3.44 and 3.45 into Eq. 3.37, the leading order integration is

$$\hat{\mathbf{u}}^{(1)} = -\frac{1}{4} \int_0^1 [U_1(s') \mathbf{i}_1(s') + 2U_2(s') \mathbf{i}_2(s')] \cdot \left(\frac{\mathbf{I}}{R} + \frac{\mathbf{R}\mathbf{R}}{R^3} \right) ds' \quad (3.46)$$

In order to evaluate Eq. 3.46, we separate it into nonlocal and local regions with an intermediate length δ which satisfies $\varepsilon \ll \delta \ll 1$,

$$\hat{\mathbf{u}}^{(1)} = \hat{\mathbf{u}}_{NL}^{(1)} + \hat{\mathbf{u}}_L^{(1)}. \quad (3.47)$$

Since the integral kernel diverges at $s' = s$ where $R \sim \varepsilon$, the leading order should be contributed by the local integration, in which the force can be Taylor-expanded as

$$\mathbf{f}^{(1)}(s') = \mathbf{f}^{(1)}(s) + O(\Delta), \quad (3.48)$$

where $\Delta = s - s'$. Then the force can be treated as a constant and pulled out of the integration.

$$\begin{aligned} \hat{\mathbf{u}}_L^{(1)} &= \frac{1}{8\pi} \int_{s-\delta}^{s+\delta} \mathbf{f}^{(1)}(s') \cdot \left(\frac{\mathbf{I}}{R} + \frac{\mathbf{R}\mathbf{R}}{R^3} \right) ds' \\ &= \frac{\mathbf{f}^{(1)}(s)}{8\pi} \cdot \int_{s-\delta}^{s+\delta} \left(\frac{\mathbf{I}}{R} + \frac{\mathbf{R}\mathbf{R}}{R^3} \right) ds' + o(1). \end{aligned} \quad (3.49)$$

Change integration variable to Δ and substitute Eq. 3.38 into Eq. 3.49, the integration becomes

$$\begin{aligned}\mathbf{J} &= \int_{s-\delta}^{s+\delta} \left(\frac{\mathbf{I}}{R} + \frac{\mathbf{RR}}{R^3} \right) ds' \\ &= \int_{-\delta}^{\delta} \frac{\mathbf{I}}{\sqrt{\Delta^2 + r^2}} + \frac{\Delta^2 \mathbf{e}_z \mathbf{e}_z + 2r\Delta \mathbf{e}_r \mathbf{e}_z + r^2 \mathbf{e}_r \mathbf{e}_r}{(\Delta^2 + r^2)^{\frac{3}{2}}} d\Delta.\end{aligned}\quad (3.50)$$

Using the integration results,

$$\int_{-\delta}^{\delta} \frac{1}{\sqrt{\Delta^2 + r^2}} d\Delta = 2 \ln \frac{2\delta}{r} + o(1), \quad (3.51a)$$

$$\int_{-\delta}^{\delta} \frac{r^2}{(\Delta^2 + r^2)^{\frac{3}{2}}} d\Delta = 2 + o(1), \quad (3.51b)$$

the local integration is evaluated as

$$\begin{aligned}\mathbf{J} &= \left(4 \ln \frac{2\delta}{r} - 2 \right) \mathbf{i}_1 \mathbf{i}_1 + \left(2 \ln \frac{2\delta}{r} + 2 \cos^2 \theta \right) \mathbf{i}_2 \mathbf{i}_2 + \left(2 \ln \frac{2\delta}{r} + 2 \sin^2 \theta \right) \mathbf{i}_3 \mathbf{i}_3 \\ &\quad + 2 \sin \theta \cos \theta \mathbf{i}_2 \mathbf{i}_3 + 2 \sin \theta \cos \theta \mathbf{i}_3 \mathbf{i}_2 + o(1).\end{aligned}\quad (3.52)$$

Substitute Eq. 3.45 into Eq. 3.49, the local flow is

$$\hat{\mathbf{u}}_L^{(1)} = -\frac{1}{4} (U_1 \mathbf{i}_1 + 2U_2 \mathbf{i}_2) \cdot \mathbf{J}. \quad (3.53)$$

Then substitute Eq. 3.52 into Eq. 3.53 and include the non-local integration. The leading order (order of $1/\ln \varepsilon$) of the outer field written in components is

$$\hat{u}_1^{(1)} = \left(\frac{1}{2} - \ln \frac{2\delta}{r} \right) U_1 + \hat{\mathbf{u}}_{NL}^{(1)} \cdot \mathbf{i}_1, \quad (3.54a)$$

$$\hat{u}_2^{(1)} = - \left(\ln \frac{2\delta}{r} + \cos^2 \theta \right) U_2 + \hat{\mathbf{u}}_{NL}^{(1)} \cdot \mathbf{i}_2, \quad (3.54b)$$

$$\hat{u}_3^{(1)} = - \sin \theta \cos \theta U_2 + \hat{\mathbf{u}}_{NL}^{(1)} \cdot \mathbf{i}_3. \quad (3.54c)$$

To match with the inner solution we transfer Eq. 3.54 to cylindrical coordinates using

$$u_r = u_2 \cos \theta + u_3 \sin \theta, \quad (3.55a)$$

$$u_\theta = -u_2 \sin \theta + u_3 \cos \theta, \quad (3.55b)$$

$$u_z = u_1. \quad (3.55c)$$

Then the components in cylindrical coordinates are

$$\hat{u}_r^{(1)} = \left[-\left(\ln \frac{2\delta}{r} + 1 \right) U_2 + \hat{\mathbf{u}}_{NL}^{(1)} \cdot \mathbf{i}_2 \right] \cos \theta + \left[\hat{\mathbf{u}}_{NL}^{(1)} \cdot \mathbf{i}_3 \right] \sin \theta, \quad (3.56a)$$

$$\hat{u}_\theta^{(1)} = \left[\hat{\mathbf{u}}_{NL}^{(1)} \cdot \mathbf{i}_3 \right] \cos \theta + \left[-\left(\ln \frac{2\delta}{r} \right) U_2 - \hat{\mathbf{u}}_{NL}^{(1)} \cdot \mathbf{i}_2 \right] \sin \theta, \quad (3.56b)$$

$$\hat{u}_z^{(1)} = \left(\frac{1}{2} - \ln \frac{2\delta}{r} \right) U_1 + \hat{\mathbf{u}}_{NL}^{(1)} \cdot \mathbf{i}_1. \quad (3.56c)$$

Now we can compare the order $1/\ln \epsilon$ term in outer solution with that inner solution in Eq. 3.36. Substitute Eq. 3.43 into Eq. 3.36, inner solution is rewritten as

$$u_r^{(01)} = \left[\left(\ln \frac{r}{\lambda} - \chi \right) U_2 - A^{(2)} \right] \cos \theta + \alpha^{(2)} \sin \theta, \quad (3.57a)$$

$$u_\theta^{(01)} = \alpha^{(2)} \cos \theta + \left[-\left(\ln \frac{r}{\lambda} + 1 - \chi \right) U_2 + A^{(2)} \right] \sin \theta, \quad (3.57b)$$

$$u_z^{(01)} = \left(\ln \frac{r}{\lambda} + \frac{\Lambda}{\epsilon \lambda} \right) U_1 - D^{(2)}. \quad (3.57c)$$

Compare Eq. 3.56 with Eq. 3.57, the coefficients $A^{(2)}$, $\alpha^{(2)}$ and $D^{(2)}$ are evaluated as

$$A^{(2)} = \left(\ln \frac{2\delta}{\lambda} + 1 - \chi \right) U_2 - \hat{\mathbf{u}}_{NL}^{(1)} \cdot \mathbf{i}_2, \quad (3.58a)$$

$$\alpha^{(2)} = \hat{\mathbf{u}}_{NL}^{(1)} \cdot \mathbf{i}_3, \quad (3.58b)$$

$$D^{(2)} = \left(\ln \frac{2\delta}{\lambda} + \frac{\Lambda}{\epsilon \lambda} - \frac{1}{2} \right) U_1 - \hat{\mathbf{u}}_{NL}^{(1)} \cdot \mathbf{i}_1. \quad (3.58c)$$

3.1.4 Force density on the body

Now we have obtained the velocity field and then measure the force on the body. Considering Eq. 3.42, which is the force density exerted by the body, the force on the body exerted by the flow \mathbf{f}^* is

$$\mathbf{f}^*(s) = -\mathbf{f}(s) = 2\pi D\mathbf{i}_1 + 4\pi A\mathbf{i}_2 - 4\pi \alpha \mathbf{i}_3. \quad (3.59)$$

Expand \mathbf{f}^* in logarithms

$$\mathbf{f}^* = \frac{\mathbf{f}^{*(1)}}{\ln \epsilon} + \frac{\mathbf{f}^{*(2)}}{\ln^2 \epsilon} + O\left(\frac{1}{\ln^3 \epsilon}\right), \quad (3.60)$$

and substitute Eq. 3.43 and Eq. 3.58 into Eq. 3.60, the first two orders are evaluated as

$$\frac{\mathbf{f}^{*(1)}}{2\pi} = \mathbf{U} \cdot [2\mathbf{I} - \mathbf{t}\mathbf{t}], \quad (3.61a)$$

$$\begin{aligned} \frac{\mathbf{f}^{*(2)}}{2\pi} &= \left[\left(\ln \frac{2\delta}{\lambda} \right) \mathbf{U} - \hat{\mathbf{u}}_{NL}^{(1)} \right] \cdot [2\mathbf{I} - \mathbf{t}\mathbf{t}] \\ &\quad + \mathbf{U} \cdot \left[2(1-\chi)\mathbf{I} + \left(2\chi + \frac{\Lambda}{\varepsilon\lambda} - \frac{5}{2} \right) \mathbf{t}\mathbf{t} \right], \end{aligned} \quad (3.61b)$$

where \mathbf{t} is the tangential vector that $\mathbf{t} = \mathbf{i}_1 = \frac{d\mathbf{r}_c(s)}{ds}$, and $\hat{\mathbf{u}}_{NL}^{(1)}$ is the non-local integration which is

$$\begin{aligned} \hat{\mathbf{u}}_{NL}^{(1)} &= \frac{1}{8\pi} \int_0^{s-\delta} + \int_{s+\delta}^1 \mathbf{f}_1(s') \cdot \left(\frac{\mathbf{I}}{R} + \frac{\mathbf{R}\mathbf{R}}{R^3} \right) ds' \\ &= -\frac{1}{4} \int_0^{s-\delta} + \int_{s+\delta}^1 \mathbf{U} \cdot [2\mathbf{I} - \mathbf{t}\mathbf{t}] \cdot \left(\frac{\mathbf{I}}{R} + \frac{\mathbf{R}\mathbf{R}}{R^3} \right) ds'. \end{aligned} \quad (3.62)$$

This is final result of the SBT I derived with Navier slip boundary condition. Comparing to orginal result in Ref. [31], the slip length Λ only show up from the second order. Slip length becomes important when χ is of order one, so that λ is order of ε . So this derivation is valid when slip length is the same order of the radius.

3.2 Distribution of flow singularities for straight rods

In this section, I consider a special case of a translating rod. By assuming constant force density, the flow can be calculated directly. I will discuss two cases that the rod translates along the direction parallel (Fig. 3.3(a)) and normal (Fig. 3.3(b)) to the axis respectively.

3.2.1 Along the axis

First I consider a rod translating along the axis, which is shown in Fig. 3.3(a), and the centerline moves with velocity

$$\mathbf{U} = U_{\parallel} \mathbf{e}_z, \quad (3.63)$$

where \mathbf{e}_z is the axial direction vector. Note that if there is no explaination the notation is consistent with that in the last section. Due to the axisymmetry, the slip boundary condition

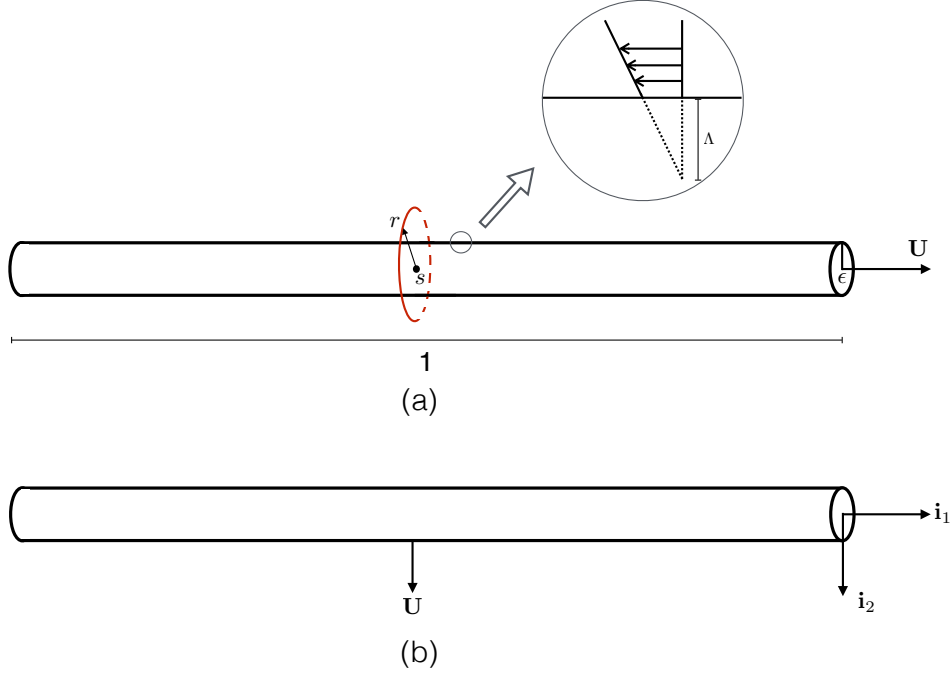


Fig. 3.2 Rod translates with slip boundary condition along the axis (a) and along the direction perpendicular to the axis (b).

would be

$$u_r(s, \varepsilon\lambda(s)) = 0 \quad (3.64a)$$

$$u_z(s, \varepsilon\lambda(s)) = U_{||} + \Lambda \frac{\partial u_z}{\partial r} \Big|_{r=\varepsilon\lambda(s)}. \quad (3.64b)$$

I first assume constant force density that

$$\mathbf{f} = f_{||} \mathbf{e}_z, \quad (3.65)$$

then the flow field induced by this force density would be

$$\mathbf{u}(s, r) = \frac{f_{||}}{8\pi} \mathbf{e}_z \cdot \int_0^1 \left(\frac{\mathbf{I}}{R} + \frac{\mathbf{R}\mathbf{R}}{R^3} \right) ds' \quad (3.66)$$

Substitute integration result in Eq. 3.52, we have

$$\mathbf{u}(s, r) = \frac{f_{||}}{4\pi} \left[2 \ln \frac{2\sqrt{s(1-s)}}{r} - 1 + o(1) \right] \mathbf{e}_z. \quad (3.67)$$

Next we consider the boundary condition in Eq. 3.64 and calculate the strain rate term

$$\frac{\partial u_z}{\partial r} = -\frac{f_{\parallel}}{2\pi r}, \quad (3.68)$$

and on the boundary it satisfies

$$\frac{f_{\parallel}}{4\pi} \left[2 \ln \frac{2\sqrt{s(1-s)}}{\varepsilon \lambda(s)} - 1 \right] = U_{\parallel} - \Lambda \frac{f_{\parallel}}{2\pi \varepsilon \lambda(s)}. \quad (3.69)$$

Then the force density is linear with the velocity which has relation

$$f_{\parallel} = \frac{4\pi U_{\parallel}}{2 \ln \frac{2\sqrt{s(1-s)}}{\varepsilon \lambda(s)} - 1 + \frac{2\Lambda}{\varepsilon \lambda(s)}}. \quad (3.70)$$

Here we see that the result is conflict with our assumption that the force density is constant. Although it is not accurate solution, we can still discuss how it varies along the centerline. If the magnitude changes slowly enough, the result will still be asymptotically valid. I choose the radius in the center as the length scale of the radius, so we have

$$\lambda\left(\frac{1}{2}\right) = 1. \quad (3.71)$$

As I assume the radius changes slowly along the centerline, or can be alternatively illustrated as that the variation of the radius is the same order of the total length, we can expand the force density around the center point,

$$f_{\parallel} = \frac{4\pi U_{\parallel}}{2 \ln \frac{1}{\varepsilon} - 1 + \frac{2\Lambda}{\varepsilon}} \left[1 - \left(s - \frac{1}{2}\right) \frac{2\lambda' \left(\frac{1}{2}\right) \left(1 - \frac{\Lambda}{\varepsilon}\right)}{2 \ln \frac{1}{\varepsilon} - 1 + \frac{2\Lambda}{\varepsilon}} + O\left(\left(s - \frac{1}{2}\right)^2\right) \right]. \quad (3.72)$$

For symmetric shape, for example spheroid or cylinder, we have $\lambda'(1/2) = 0$, then

$$f_{\parallel} = \frac{4\pi U_{\parallel}}{2 \ln \frac{1}{\varepsilon} - 1 + \frac{2\Lambda}{\varepsilon}} \left[1 + O\left(\left(s - \frac{1}{2}\right)^2\right) \right]. \quad (3.73)$$

As $(s - 1/2)^2 \leq 0.25$, we say the value of force density varies slowly along the body, and the force density is approximately

$$f_{\parallel} = \frac{4\pi U_{\parallel}}{2 \ln \frac{1}{\varepsilon} - 1 + \frac{2\Lambda}{\varepsilon}}. \quad (3.74)$$

3.2.2 Perpendicular to axis

In the second problem, I consider the normal translation with velocity

$$\mathbf{U} = U_{\perp} \mathbf{i}_2. \quad (3.75)$$

The slip boundary condition is

$$u_r(s, \varepsilon\lambda(s)) = U_{\perp} \cos \theta \quad (3.76a)$$

$$u_{\theta}(s, \varepsilon\lambda(s)) = -U_{\perp} \sin \theta + \Lambda \left[r \frac{\partial}{\partial r} \left(\frac{u_{\theta}}{r} \right) + \frac{1}{r} \frac{\partial u_r}{\partial \theta} \right] \Big|_{r=\varepsilon\lambda(s)}. \quad (3.76b)$$

Similarly I first assume constant force density,

$$\mathbf{f}_{\perp} = f_{\perp} \mathbf{i}_2, \quad (3.77)$$

and the flow would be

$$\mathbf{u}_s(s, r, \theta) = \frac{f_{\perp}}{8\pi} \mathbf{i}_2 \cdot \int_0^1 \left(\frac{\mathbf{I}}{R} + \frac{\mathbf{R}\mathbf{R}}{R^3} \right) ds'. \quad (3.78)$$

Note that different from the axial translation case, we will see that the flow induced by the stokeslets can not be matched with boundary condition, dipole is thus needed. So here I use 's' to denote velocity induced by the stokeslets. Substitute the integration result in Eq. 3.52, we obtain

$$\begin{aligned} \mathbf{u}_s(s, r, \theta) &= \frac{f_{\perp}}{8\pi} \left[\left(2 \ln \frac{2\sqrt{s(1-s)}}{r} + 2 \cos^2 \theta \right) \mathbf{i}_2 + 2 \sin \theta \cos \theta \mathbf{i}_3 \right] \\ &= \frac{f_{\perp}}{4\pi} \left[\ln \frac{2\sqrt{s(1-s)}}{r} \mathbf{i}_2 + \cos \theta \mathbf{e}_r \right]. \end{aligned} \quad (3.79)$$

The induced flow field is not aligned along the direction of \mathbf{i}_2 , so we need to include dipoles to match the boundary condition. Following the same procedure, assume the dipole

density is constant

$$\mathbf{g} = g\mathbf{i}_2, \quad (3.80)$$

then the flow is integrated as

$$\mathbf{u}_d(s, r, \theta) = \frac{g}{4\pi} \mathbf{i}_2 \cdot \int_0^1 \left(\frac{\mathbf{I}}{R^3} - \frac{3\mathbf{R}\mathbf{R}}{R^5} \right) ds'. \quad (3.81)$$

Then substitute Eq. 3.38 into Eq. 3.81 and change integration variable with Δ , the integration becomes

$$\begin{aligned} \mathbf{K} &= \int_0^1 \left(\frac{\mathbf{I}}{R^3} - \frac{3\mathbf{R}\mathbf{R}}{R^5} \right) ds' \\ &\sim \int_{s-1}^s \left(\frac{\mathbf{I}}{R^3} - \frac{3\mathbf{R}\mathbf{R}}{R^5} \right) d\Delta \\ &\sim \int_{s-1}^s \left(\frac{\mathbf{I}}{(\Delta^2 + r^2)^{\frac{3}{2}}} - 3 \frac{\Delta^2 \mathbf{e}_z \mathbf{e}_z + r^2 \mathbf{e}_r \mathbf{e}_r}{(\Delta^2 + r^2)^{\frac{5}{2}}} \right) d\Delta. \end{aligned} \quad (3.82)$$

Calculate the integrals

$$\int_{s-1}^s \frac{1}{(\Delta^2 + r^2)^{\frac{3}{2}}} d\Delta \sim \frac{2}{r^2}, \quad (3.83a)$$

$$\int_{s-1}^s \frac{r^2}{(\Delta^2 + r^2)^{\frac{5}{2}}} d\Delta \sim \frac{4}{3r^2}, \quad (3.83b)$$

and substitute it into Eq. 3.82, we obtain

$$\begin{aligned} r^2 \mathbf{K} &= (2 - 4 \cos^2 \theta) \mathbf{i}_2 \mathbf{i}_2 + (2 - 4 \sin^2 \theta) \mathbf{i}_3 \mathbf{i}_3 \\ &\quad - 4 \sin \theta \cos \theta \mathbf{i}_2 \mathbf{i}_3 - 4 \sin \theta \cos \theta \mathbf{i}_3 \mathbf{i}_2 + o(1). \end{aligned} \quad (3.84)$$

Substitute Eq. 3.84 into Eq. 3.81, the dipole induced velocity is

$$\mathbf{u}_d(s, r, z) = \frac{g}{2\pi r^2} [\mathbf{i}_2 - 2 \cos \theta \mathbf{e}_r]. \quad (3.85)$$

Next combine Eq. 3.79 and 3.85, we can cancel the unwanted component on the radial direction. Assume the net field is

$$\mathbf{u}_\perp = \mathbf{u}_s + \mathbf{u}_d, \quad (3.86)$$

and consider the boundary condition in Eq. 3.76. Calculate the components in cylindrical coordinates

$$u_r = \frac{\cos \theta}{4\pi} \left[f_{\perp} \left(\ln \frac{2\sqrt{s(1-s)}}{r} + 1 \right) - \frac{2g}{r^2} \right], \quad (3.87a)$$

$$u_{\theta} = -\frac{\sin \theta}{4\pi} \left[f_{\perp} \ln \frac{2\sqrt{s(1-s)}}{r} + \frac{2g}{r^2} \right] \quad (3.87b)$$

and the strain rate terms

$$r \frac{\partial}{\partial r} \left(\frac{u_{\theta}}{r} \right) = \frac{\sin \theta}{4\pi r} \left[f_{\perp} \left(\ln \frac{2\sqrt{s(1-s)}}{r} + 1 \right) + \frac{6g}{r^2} \right], \quad (3.88a)$$

$$\frac{1}{r} \frac{\partial u_r}{\partial \theta} = -\frac{\sin \theta}{4\pi r} \left[f_{\perp} \left(\ln \frac{2\sqrt{s(1-s)}}{r} + 1 \right) - \frac{2g}{r^2} \right]. \quad (3.88b)$$

Substitute Eq. 3.87 and 3.88 into Eq. 3.76, we obtain

$$f_{\perp} \left(\ln \frac{2\sqrt{s(1-s)}}{\varepsilon \lambda(s)} + 1 \right) - \frac{2g}{\varepsilon^2 \lambda^2(s)} = 4\pi U_{\perp} \quad (3.89a)$$

$$-\left[f_{\perp} \ln \frac{2\sqrt{s(1-s)}}{\varepsilon \lambda(s)} + \frac{2g}{\varepsilon^2 \lambda^2(s)} \right] = -4\pi U_{\perp} + \frac{8\Lambda g}{\varepsilon^3 \lambda^3(s)}. \quad (3.89b)$$

Solve for g and f_{\perp} , we obtain that g is linear with the force density as

$$g = \frac{\varepsilon^3 \lambda^3}{4(\varepsilon \lambda + 2\Lambda)} f_{\perp} = \frac{\chi \varepsilon^2 \lambda^2}{2} f_{\perp} \quad (3.90)$$

to match the boundary condition and the force density is

$$f_{\perp} = \frac{4\pi U_{\perp}}{\ln \frac{2\sqrt{s(1-s)}}{\varepsilon \lambda(s)} + 1 - \chi(s)}. \quad (3.91)$$

Again the solution here is conflict with the assumption of constant force density. With the same approach of expansion, we can prove that the force changes slowly along the centerline. I assume $\lambda(1/2) = 1$ and expand the force around the point, and the force density is approximately

$$f_{\perp} = \frac{4\pi U_{\perp}}{\ln \frac{1}{\varepsilon} + 1 - \frac{\varepsilon}{2(\varepsilon + 2\Lambda)}}, \quad (3.92)$$

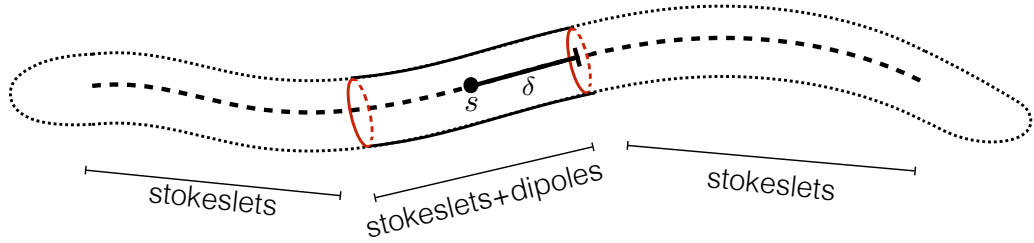


Fig. 3.3 Lighthill's singularity construction for the slender-body theory of flagellar hydrodynamics. To evaluate the flow near the point s , the body is separated into inner and outer region by an intermediate length δ which satisfies $a \ll \delta \ll L$. The flow is presented by that induced by a line distribution of stokeslets along the whole centerline and dipoles only in the inner region.

which is a constant. As discussed before, slip becomes important when it the slip length has the same scale with the radius, then I define a ratio of the slip length to ε ,

$$\gamma = \frac{\Lambda}{\varepsilon}, \quad (3.93)$$

which is order 1 according to the assumption. Combine with Eq. 3.74 and 3.92, and introduce the resistance coefficients ξ_{\parallel} and ξ_{\perp} , we obtain the resistive force theory with Navier slip condition that

$$f^*_{\parallel} = -\xi_{\parallel} U_{\parallel}, \quad f^*_{\perp} = -\xi_{\perp} U_{\perp}, \quad (3.94)$$

where f^* represents the force exerted by flow on the rod. The coefficients are

$$\xi_{\parallel} = \frac{2\pi}{\ln \frac{1}{\varepsilon} - \frac{1}{2} + \gamma}, \quad (3.95a)$$

$$\xi_{\perp} = \frac{4\pi}{\ln \frac{1}{\varepsilon} + \frac{1}{2} + \frac{2\gamma}{1+2\gamma}}. \quad (3.95b)$$

Compare Eq. 3.95 with Lighthill's result in Ref. [88], the resistant coefficient is a function of the γ . In the case of zero slip length, $\gamma = 0$, it is consistent with the Lighthill's.

3.3 Slender-body theory

In the previous section, I have obtained the relation between the dipole density and force density to match the boundary condition. Using this relation in Eq. 3.90 I derive Lighthill's SBT [89] for slip in this section. The idea is to consider an arbitrary slender body and choose

an intermediate length δ that satisfies $\varepsilon \ll \delta \ll 1$. Define that the inner region is $|\Delta| \leq \delta$, and the outer region $|\Delta| > \delta$. The velocity of the filament is induced from stokelets and dipoles with relation in Eq. 3.90. Let us see the orders of velocity in two regions respectively. In the inner region, the velocity induced by the stokelets is $O(1/\ln \varepsilon)$ and the velocity induced by the dipoles is $O(1)$. In the outer region, the velocity from stokeslets is $O(1/\ln \delta)$ while from dipoles it is $O\left(\frac{\varepsilon^2}{\delta^2}\right)$. If we keep all the terms as large as order 1, then we consider a line of stokeslets along the whole centerline and dipoles with density linear with that of force (Eq. 3.90) only in the inner region. Consider the slip boundary condition in Eq. 3.6, mathematical interpretation of the velocity is

$$\mathbf{U} = \mathbf{U}^I + \mathbf{U}^O, \quad (3.96a)$$

$$\mathbf{U}^I = [\mathbf{u}_s^I + \mathbf{u}_d^I - 2\Lambda(\mathbf{I} - \mathbf{e}_r \mathbf{e}_r) \cdot (\mathbf{E}_s^I + \mathbf{E}_d^I) \cdot \mathbf{e}_r] |_{r=\varepsilon\lambda(s)}, \quad (3.96b)$$

$$\mathbf{U}^O = [\mathbf{u}_s^O - 2\Lambda(\mathbf{I} - \mathbf{e}_r \mathbf{e}_r) \cdot \mathbf{E}_s^O \cdot \mathbf{e}_r] |_{r=\varepsilon\lambda(s)}, \quad (3.96c)$$

in which the upper indices 'I' and 'O' represents the inner and outer regions, and the lower indices 's' and 'd' indicate the velocities or strain rates induced from stokeslets and dipoles. The velocity and strain rates are represented by the integrals

$$\begin{aligned} \mathbf{u}_s^I &= \int_{|\Delta| \leq \delta} \frac{\mathbf{f}}{8\pi} \cdot \left(\frac{\mathbf{I}}{R} + \frac{\mathbf{R}\mathbf{R}}{R^3} \right) d\Delta, \\ \mathbf{u}_d^I &= \int_{|\Delta| \leq \delta} \frac{\mathbf{g}}{4\pi} \cdot \left(\frac{\mathbf{I}}{R^3} - \frac{3\mathbf{R}\mathbf{R}}{R^5} \right) d\Delta, \\ \mathbf{u}_s^O &= \int_{|\Delta| > \delta} \frac{\mathbf{f}}{8\pi} \cdot \left(\frac{\mathbf{I}}{R} + \frac{\mathbf{R}\mathbf{R}}{R^3} \right) d\Delta, \\ \mathbf{E}_{s,d}^I &= \frac{\nabla \mathbf{u}_{s,d}^I + (\nabla \mathbf{u}_{s,d}^I)^T}{2}, \quad \mathbf{E}_s^O = \frac{\nabla \mathbf{u}_s^O + (\nabla \mathbf{u}_s^O)^T}{2}. \end{aligned}$$

What is important in this description is that, different from no slip case, the velocity of the body is not equal to the fluid velocity near the surface, so that we cannot directly use the fluid velocity to represent the body motion. Instead, we need to subtract the slip velocity which is proportional to the stress according to Eq. 3.6.

I first calculate the velocity induced by inner region. Consider Eq. 3.90 and assume constant force density

$$\mathbf{f} = f_{\parallel} \mathbf{i}_1 + f_{\perp} \mathbf{i}_2, \quad (3.97a)$$

$$\mathbf{g} = \frac{\chi \varepsilon^2 \lambda^2}{2} f_{\perp} \mathbf{i}_2. \quad (3.97b)$$

Substitute integration results in Eq. 3.52 and 3.84 into Eq. 3.96b, we have

$$\begin{aligned}\mathbf{u}_s^I &= \frac{f_{\parallel}}{4\pi} \left(2 \ln \frac{2\delta}{r} - 1 \right) \mathbf{i}_1 + \frac{f_{\perp}}{4\pi} \left[\left(\ln \frac{2\delta}{r} + \cos^2 \theta \right) \mathbf{i}_2 + \sin \theta \cos \theta \mathbf{i}_3 \right], \\ \mathbf{u}_d^I &= \frac{g}{2\pi r^2} \left[(1 - 2 \cos^2 \theta) \mathbf{i}_2 - 2 \sin \theta \cos \theta \mathbf{i}_3 \right].\end{aligned}$$

Then the components of the total flow $\mathbf{u}_s^I + \mathbf{u}_d^I$ in cylindrical coordinates are

$$u_z = \frac{f_{\parallel}}{4\pi} \left(\ln \frac{2\delta}{r} - 1 \right) \quad (3.98a)$$

$$u_r = \frac{f_{\perp} \cos \theta}{4\pi} \left(\ln \frac{2\delta}{r} + 1 - \chi \frac{\varepsilon^2 \lambda^2}{r^2} \right) \quad (3.98b)$$

$$u_{\theta} = -\frac{f_{\perp} \sin \theta}{4\pi} \left(\ln \frac{2\delta}{r} + \chi \frac{\varepsilon^2 \lambda^2}{r^2} \right). \quad (3.98c)$$

Separate the velocity along the axial and normal directions

$$\mathbf{U}^I = U_{\parallel} \mathbf{i}_1 + U_{\perp} \mathbf{i}_2, \quad (3.99)$$

and write the U_{\parallel} and U_{\perp} with cylindrical components of $\mathbf{u}_s^I + \mathbf{u}_d^I$, we have

$$U_{\parallel} = \left[u_z - \Lambda \frac{\partial u_z}{\partial r} \right] \Big|_{r=\varepsilon\lambda(s)} \quad (3.100a)$$

$$U_{\perp} = \sqrt{u_r^2 + \left[u_{\theta} - \Lambda \left(r \frac{\partial}{\partial r} \left(\frac{u_{\theta}}{r} \right) + \frac{1}{r} \frac{\partial u_r}{\partial \theta} \right) \right]^2} \Big|_{r=\varepsilon\lambda(s)}. \quad (3.100b)$$

Substitute Eq. 3.98 into Eq. 3.100, we have

$$U_{\parallel} = \frac{f_{\parallel}}{4\pi} \left(2 \ln \frac{2\delta}{\varepsilon\lambda} - 1 + \frac{2\Lambda}{\varepsilon\lambda} \right) \quad (3.101a)$$

$$U_{\perp} = \frac{f_{\perp}}{4\pi} \left(\ln \frac{2\delta}{\varepsilon\lambda} + 1 - \chi \right). \quad (3.101b)$$

By introducing a new parameter

$$q(s) = \frac{1}{2} \varepsilon \lambda(s) e^{\frac{1}{2} - \frac{\Lambda}{\varepsilon \lambda(s)}}, \quad (3.102)$$

we can write Eq. 3.101 as

$$U_{\parallel} = \frac{f_{\parallel}}{2\pi} \ln \frac{\delta}{q}, \quad (3.103a)$$

$$U_{\perp} = \frac{f_{\perp}}{8\pi} \left(3 - 2\chi - \frac{2\Lambda}{\varepsilon\lambda} \right) + \frac{f_{\perp}}{4\pi} \ln \frac{\delta}{q}. \quad (3.103b)$$

Substitute into Eq. 3.99 and consider the inverse result of Eq. 3.84, the inner velocity can be written as the integration form

$$\mathbf{U}^I(s) = \frac{\mathbf{f}_{\perp}}{8\pi} \left(3 - 2\chi - \frac{2\Lambda}{\varepsilon\lambda} \right) + \int_{q(s) < |\Delta| \leq \delta} \frac{\mathbf{f}}{8\pi} \cdot \left(\frac{\mathbf{I}}{R} + \frac{\mathbf{R}\mathbf{R}}{R^3} \right) d\Delta. \quad (3.104)$$

Then we consider the velocity induced by the outer region which is

$$\mathbf{U}^O = [\mathbf{u}_s^O - 2\Lambda(\mathbf{I} - \mathbf{e}_r \mathbf{e}_r) \cdot \mathbf{E}_s^O \cdot \mathbf{e}_r] \Big|_{r=\varepsilon\lambda(s)}, \quad (3.105)$$

where

$$\mathbf{E}_s^O = \int_{|\Delta| > \delta} \frac{\mathbf{f}}{8\pi} \cdot \left(\frac{\mathbf{I}\mathbf{R}}{R^3} - \frac{3\mathbf{R}\mathbf{R}\mathbf{R}}{R^5} \right) d\Delta. \quad (3.106)$$

The order of \mathbf{u}_s^O is $O(1/\ln \delta)$, and the order of \mathbf{E}_s^O is $O(\delta^{-1})$, then the order of the second term in Eq. 3.105 is $O(\Lambda/\delta)$. As we assumed slip length is the same order of radius, the second term should be much smaller than the first term. Taking advantage of this, δ can be cancelled and the velocity of the centerline would be

$$\mathbf{U}(s) = \frac{\mathbf{f}_{\perp}}{8\pi} \left(3 - 2\chi - \frac{2\Lambda}{\varepsilon\lambda} \right) + \frac{1}{8\pi} \int_{|\Delta| > q(s)} \mathbf{f} \cdot \left(\frac{\mathbf{I}}{R} + \frac{\mathbf{R}\mathbf{R}}{R^3} \right) d\Delta. \quad (3.107)$$

When the slip length is zero, $\chi = 1/2$ (Eq. 3.27), and the result is consistent with Lighthill's [89]. Considering Eq. 3.102, parameter q which represents the length of the integration region, is also a function of slip length. When the slip length is zero, it is consistent with no slip case in which $q \sim 0.82b$ (recall the notation of radius $b = \varepsilon\lambda$). With larger slip length, the length of local region decreases exponentially. For example for $\Lambda/b = 0.5, 1, 2$, we have $q/b = 0.5, 0.3, 0.1$.

3.4 Validation and comparison

With the Navier slip assumption, I now have extended the SBT of Cox's in Eq. 3.61 and Lighthill's in Eq. 3.107. In between I also calculated the resistance coefficients for translating rods in Eq. 3.95. In the section, I first compare the the SBT result with the resistance coefficients derived and prove the consistency, then compare the coefficients with the numerical results that have been obtained for spheroid.

3.4.1 Validation of slip SBT

First consider the rod translating along the axis with velocity

$$\mathbf{U} = U \mathbf{i}_1, \quad (3.108)$$

substitute it into Eq. 3.62 and calculate the integration is evaluated as

$$\mathbf{u}_1^{NL} = \ln \frac{\delta}{\sqrt{s(1-s)}}. \quad (3.109)$$

Then substitute Eq. 3.109 into Eq. 3.61, we have

$$\frac{\mathbf{f}_1^*}{2\pi} = U \mathbf{i}_1 \quad (3.110a)$$

$$\frac{\mathbf{f}_2^*}{2\pi} = \left[\ln \frac{2\sqrt{s(1-s)}}{\lambda} + \frac{\Lambda}{\varepsilon\lambda} - \frac{1}{2} \right] U \mathbf{i}_1. \quad (3.110b)$$

Substitute into the logarithmical expansion of \mathbf{f}^* and U , and consider the resistive force theory in Eq. 6.4, the logarithmical expansion of the tangential resistance coefficient is

$$\frac{\xi_{\parallel}}{2\pi} = -\frac{1}{\ln \varepsilon} - \frac{1}{\ln^2 \varepsilon} \left[\ln \frac{2\sqrt{s(1-s)}}{\lambda} + \frac{\Lambda}{\varepsilon\lambda} - \frac{1}{2} \right] + O\left(\frac{1}{\ln^3 \varepsilon}\right) \quad (3.111)$$

Then I compare it with Eq. 3.70 by expand Eq. 3.70 as

$$\begin{aligned} \frac{\xi_{\parallel}}{2\pi} &= \frac{1}{\ln \frac{2\sqrt{s(1-s)}}{\varepsilon\lambda} - \frac{1}{2} + \frac{\Lambda}{\varepsilon\lambda}} \\ &= -\frac{1}{\ln \varepsilon} \left[1 + \frac{1}{\ln \varepsilon} \left(\ln \frac{2\sqrt{s(1-s)}}{\lambda} + \frac{\Lambda}{\varepsilon\lambda} - \frac{1}{2} \right) + O(\ln^2 \varepsilon) \right], \end{aligned} \quad (3.112)$$

which shows is consistent with Eq. 3.111. Similarly, we can consider the rod translates along the direction normal to the axis,

$$\mathbf{U} = U\mathbf{i}_2, \quad (3.113)$$

with the slip SBT we obtain

$$\frac{\mathbf{f}_1^*}{4\pi} = U\mathbf{i}_2, \quad (3.114a)$$

$$\frac{\mathbf{f}_2^*}{4\pi} = \left[\ln \frac{2\sqrt{s(1-s)}}{\lambda} + 1 - \chi \right] U\mathbf{i}_2, \quad (3.114b)$$

leading to the normal resistance coefficient expanded as

$$\frac{\xi_\perp}{4\pi} = -\frac{1}{\ln \varepsilon} - \frac{1}{\ln^2 \varepsilon} \left[\ln \frac{2\sqrt{s(1-s)}}{\lambda} + 1 - \chi \right] + O\left(\frac{1}{\ln^3 \varepsilon}\right), \quad (3.115)$$

which can be easily proved to be consistent with Eq. 3.91.

3.4.2 Comparison with numerical results

We now have approximate local resistance coefficients for rods in Eq. 3.95. As mentioned in the beginning, for the geometry of spheroid, although it is not straightforward to derive the drag coefficient analytically, numerical methods have been used to measure it. In Ref. [69, 25], Keh and Chang measured the tangential and normal drag coefficients for spheroids with a range of aspect ratios. I pick the data for relatively long and thin geometries with aspect ratios $\varepsilon = 0.1$ and 0.05 , and compare it with my result in Eq. 3.95. The comparison is shown in FIG. 3.4.

We observe that for thinner shape, my result matches more accurately. And the error increases with Λ/ε because in the asymptotics, we assume $\Lambda/\varepsilon \sim O(1)$, and the expansion in logarithms breaks when $\Lambda \gg \varepsilon |\ln \varepsilon|$.

3.5 Discussion

In this Chapter, I derive a slender-body theory with Navier slip boundary condition. In particular, I calculate the corresponding resistance coefficients in Eq. 3.95. We observe that the tangential resistance coefficient decrease significantly with increasing slip length, while

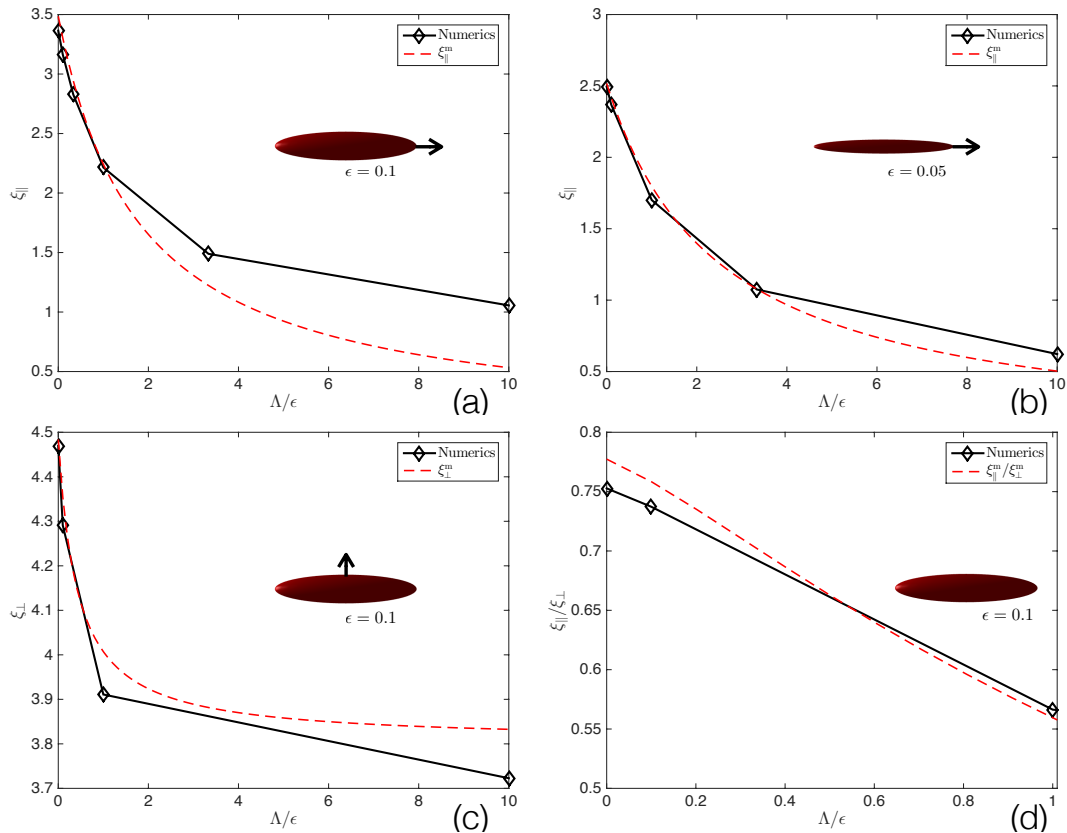


Fig. 3.4 Compare the theoretical results with numerical results from Keh and Chang [69](tangential) and [25](normal). (a) The tangential coefficient ξ_{\parallel} for the spheroid with $\epsilon = 0.1$. (b) The tangential coefficient ξ_{\parallel} for the spheroid with $\epsilon = 0.05$. (c) The tangential coefficient ξ_{\perp} for the spheroid with $\epsilon = 0.1$. (d) The ratio of ξ_{\parallel} to ξ_{\perp} .

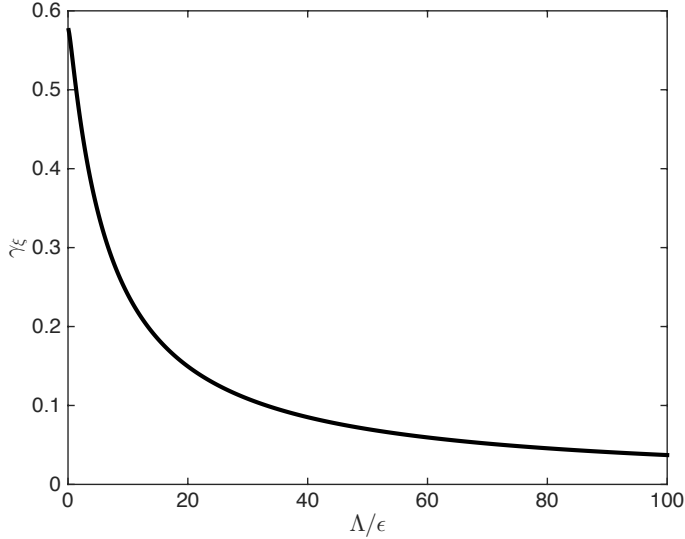


Fig. 3.5 Plot the ratio of resistance coefficients for $\epsilon = 0.001$.

the resistance coefficient of normal direction is relatively less dependent on the change of slip length. For example, we consider a very thin rod with aspect ratio $\epsilon = 0.001$. Introducing a ratio of resistance coefficients $\gamma_\xi = \xi_{\parallel}/\xi_{\perp}$ which is evaluated as

$$\gamma_\xi = \frac{\ln \frac{1}{\epsilon} + 1 - \frac{\epsilon}{2(\epsilon + 2\Lambda)}}{2 \ln \frac{1}{\epsilon} - 1 + \frac{2\Lambda}{\epsilon}}, \quad (3.116)$$

we plot γ_ξ with respect to slip length in FIG. 3.5. When the slip length is large, tangential resistance coefficient is much smaller than that along the normal direction. Intuitively we consider the swimming enhancement provided by slip effects is due to the reduction of viscous friction, and the influence from such boundary condition is much weaker along the normal direction comparing to along the tangential direction. The study in this chapter provide a quantitative evidence for this understanding.

Chapter 4

Hydrodynamic interactions between biological filaments

In previous two chapters, I focus on slip effect, which generally exists in complex fluids and plays an important role in locomotion of micro-swimmers. Inspired by classical studies for no-slip boundary condition, I develop analytical models for swimming with slip and in particular I propose a new mechanism for swimming enhancement. In all the problems that have been discussed, I study only a single filament. However, in many situations, for example most types of bacteria, more than one filament are involved in swimming. From this chapter, I will consider multiple filaments and discuss how the hydrodynamic interactions between the filaments affect the flow.

In this chapter, I first consider two filaments close to each other and show that analytical progress can be achieved by taking advantage of a separation of length scales. A generic two-filament setup (as in Fig. 1b) is characterized by three length scales: the filament radius, a ; the separation distance between the filaments, h ; and the filament length, L . While far-field studies focus on the limit $h \gg L, a$, many biological situations are in the opposite near-field limit, for example in the case of waving cilia arrays [15], for which $a, h \ll L$, i.e. slender filaments close to each other compared to their typical size. I show here that in the special case where $a \ll h$, i.e. for filaments thinner than any other length scale in the problem, the hydrodynamic interactions between the filaments can be analytically integrated out, leading to a set of simplified local equations at leading order in the limit $a \ll h \ll L$. The final results, illustrated on a simple model of two interacting rigid filaments, will allow to tackle theoretically a range of problems in biological physics. The model will be illustrated in §4.1, and an application of the result for planner wave will be shown in §4.2.

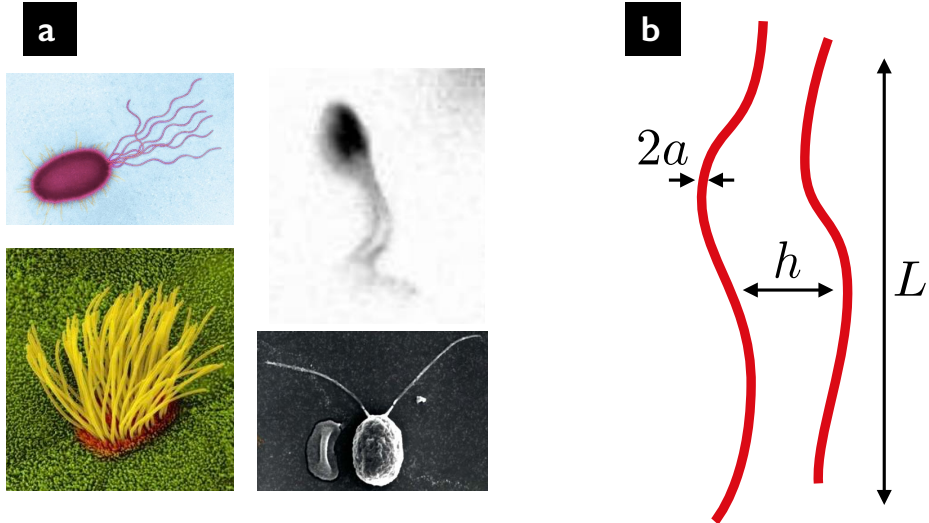


Fig. 4.1 (a) Four examples where biological filaments interact through a viscous fluid (clockwise from top left): flagellar filaments of peritrichous bacteria; two spermatozoa synchronizing their flagella; the two flagella of *Chlamydomonas*; epithelium cilia. (b) Schematic representation of prototypical situation of interest: two slender filaments of length L and cross-sectional radius a located at distance h from each other.

4.1 Long-wavelength integration

4.1.1 Set-up

Consider the two filaments in Fig. 1b, numbered #1 and #2. Denote the location of the centerline to filament i as $\mathbf{r}(s, t)$ where s is the arclength, and let $\mathbf{t}^{(i)}(s) = \partial\mathbf{r}^{(i)}/\partial s$ be its unit tangent. Since the filament is slender ($a \ll L$), resistive-force theory [88] states that the hydrodynamic force densities on each filament, $\mathbf{f}^{(1)}$ and $\mathbf{f}^{(2)}$, are proportional to the local velocity of the filament relative the background fluid i.e.

$$\mathbf{f}^{(1)} = - \left[\xi_{\parallel} \mathbf{t}^{(1)} \mathbf{t}^{(1)} + \xi_{\perp} (\mathbf{I} - \mathbf{t}^{(1)} \mathbf{t}^{(1)}) \right] \cdot \left(\frac{\partial \mathbf{r}^{(1)}}{\partial t} - \mathbf{v}^{(2) \rightarrow (1)} \right), \quad (4.1a)$$

$$\mathbf{f}^{(2)} = - \left[\xi_{\parallel} \mathbf{t}^{(2)} \mathbf{t}^{(2)} + \xi_{\perp} (\mathbf{I} - \mathbf{t}^{(2)} \mathbf{t}^{(2)}) \right] \cdot \left(\frac{\partial \mathbf{r}^{(2)}}{\partial t} - \mathbf{v}^{(1) \rightarrow (2)} \right), \quad (4.1b)$$

where all fields are implicitly functions of s and t and where ξ_{\perp} and ξ_{\parallel} are the drag coefficients for motion in the direction perpendicular and parallel to its local tangent [88]. I compute below the hydrodynamic force density acting on filament #1, the other one being deduced by symmetry. In Eq. 4.1a, the term $\mathbf{v}^{(2) \rightarrow (1)}$ denotes the flow induced by the motion of filament 2 near filament 1: it represents the effect of hydrodynamic interactions and the goal

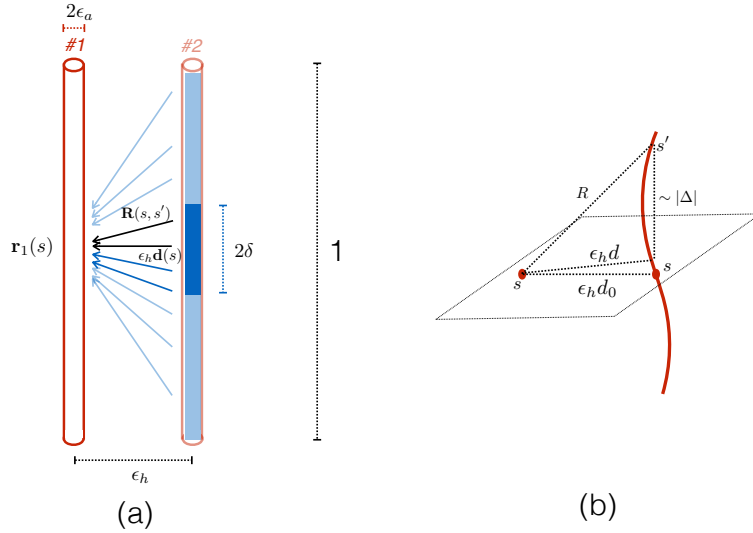


Fig. 4.2 (a) Illustration of method to compute hydrodynamic interactions. The integration region is divided into local region with length 2δ and non-local region. (b) Geometric relations between d , d_0 and R ; R is the distance between points on two rods; $\epsilon_h d$ the projection in $x - y$ plane; $\epsilon_h d_0$ is the local separation distance.

of this work is to show how to calculate its value. As filament #2 undergoes in general both rotational and translational motion, I split $\mathbf{v}^{(2) \rightarrow (1)}$ into the flows induced by local moments, $\mathbf{v}_M^{(2) \rightarrow (1)}$ (rotation), and those induced by local forces, $\mathbf{v}_F^{(2) \rightarrow (1)}$ (translation). We then write

$$\mathbf{v}^{(2) \rightarrow (1)} = \mathbf{v}_M^{(2) \rightarrow (1)} + \mathbf{v}_F^{(2) \rightarrow (1)}, \quad (4.2)$$

and calculate the values of each term in the long wavelength limit, $h \ll L$.

4.1.2 Point moments (rotlets)

To simplify the presentation, I focus in detail on the derivation of the first velocity term, $\mathbf{v}^{(2) \rightarrow (1)}$, induced by the rotational motion of filament #2, while the value of $\mathbf{v}^{(2) \rightarrow (1)}$ is computed along similar lines (see below). Note that while $\mathbf{v}^{(2) \rightarrow (1)}$ is exactly zero for non-rotating filaments, e.g. in the case of the planar waving flagella of spermatozoa, it will be important in other situations involving rotation, e.g. the dynamics of bacterial flagellar filaments. Since $a \ll h$, the flow may be described by a superposition of flow singularities. If $\mathbf{m}^{(2)}$ denotes the hydrodynamic torque density acting on filament #2, the flow is given as a line of integral of rotlets (or point torques) as [8]

$$\mathbf{v}_M^{(2) \rightarrow (1)}(s) = \int_0^L \frac{-\mathbf{m}^{(2)}(s')}{8\pi\mu} \times \frac{\mathbf{R}(s, s')}{R(s, s')^3} ds', \quad (4.3)$$

where s and s' are the arclengths along filaments 1 and 2 and $\mathbf{R}(s, s') = \mathbf{r}^{(1)}(s) - \mathbf{r}^{(2)}(s')$ is the relative position vector with magnitude R (all quantities are implicit functions of time). If filament 2 rotates relative to the background fluid with rotation rate $\boldsymbol{\omega}^{(2)}(s')$ then it is a classical result that $\mathbf{m}^{(2)}(s') = -\xi_r \boldsymbol{\omega}^{(2)}(s') \mathbf{t}^{(2)}(s')$, where the resistance coefficient in rotation is $\xi_r = 4\pi\mu a^2$.

Next I nondimensionalize lengths by L , leading to two dimensionless numbers: the filament aspect ratio, $\varepsilon_a = a/L$, and the distance-to-size ratio, $\varepsilon_h = h/L$. Times are nondimensionalized by a relevant time scale T . The integral from Eq. 4.3 becomes then in dimensionless form

$$\bar{\mathbf{v}}_M^{(2)\rightarrow(1)}(\bar{s}) = \frac{\varepsilon_a^2}{2} \int_0^1 \bar{\boldsymbol{\omega}}(\bar{s}')^{(2)} \mathbf{t}^{(2)}(\bar{s}') \times \frac{\bar{\mathbf{R}}(\bar{s}, \bar{s}')}{\bar{R}(\bar{s}, \bar{s}')^3} d\bar{s}', \quad (4.4)$$

and I drop the bars for notation convenience.

Since we are in the long wavelength limit, $\varepsilon_h \ll 1$, the typical radius of curvature of the filaments, L^2/h , is much larger than h , and thus it is natural to use cartesian coordinates (Fig. 2). I denote \mathbf{e}_z the unit vector along the mean direction of the (approximately) parallel filaments and describe the instantaneous geometry of each filament as $\mathbf{r}^{(i)}(t, s(i)) = [\varepsilon_h x^{(i)}(t, s^{(i)}), \varepsilon_h y^{(i)}(t, s^{(i)}), s^{(i)}]$ where $s^{(1)} = s$ and $s^{(2)} = s'$. Introducing the notation $\Delta = s - s'$ and the planar vector $d(s; s') = [x^{(1)}(s) - x^{(2)}(s'), y^{(1)}(s) - y^{(2)}(s'), 0]$ of magnitude $d = |\mathbf{d}|$, then the relative position vector \mathbf{R} is written by separating direction along and perpendicular to the filaments as $\mathbf{R} = \Delta \mathbf{e}_z + \varepsilon_h d$, with magnitude $R = (\Delta^2 + \varepsilon_h^2 d^2)^{1/2}$.

The schematic representation of how the integration is performed is shown in Fig. 2a with detailed notation in Fig. 2b. The method is inspired by a classical calculation due to Lighthill where, in order to describe the flow induced by the motion of a single filament, he separated the flow induced by point singularities into local and nonlocal terms using an intermediate length scale on which the filament was still slender but almost straight [9]. I introduce an intermediate length scale δ satisfying $\varepsilon_h \ll \delta \ll 1$ and split the integration into two regions: (1) a nonlocal region, $|\Delta| \geq \delta$, where the distance between two points on the filaments is dominated by $R \sim |\Delta|$ since $\varepsilon_h \ll \delta$ (resulting velocity denoted \mathbf{v}^{NL}); and (2) a local region where $|\Delta| \leq \delta$, and for which in the limit $\delta \ll 1$ we can approximate $R \sim (\Delta^2 + \varepsilon_h^2 d_0^2)^{1/2}$ where d_0 is the local filament-filament distance $d_0(s) = d(s; s' = s)$ (resulting velocity denoted \mathbf{v}^{L}). The final result, sum of \mathbf{v}^{NL} and \mathbf{v}^{L} , should then be independent of the value of δ .

Changing the variable of integration in Eq. 4.4 to $\Delta = s - s'$, the non-local contribution to the integral is given by

$$\mathbf{v}_M^{\text{NL}} = \frac{\varepsilon_a^2}{2} \left(\int_{s-1}^{-\delta} + \int_{\delta}^s \right) \left[\boldsymbol{\omega}^{(2)}(s - \Delta) \mathbf{t}^{(2)}(s - \Delta) \times \frac{\mathbf{R}}{R^3} \right] d\Delta. \quad (4.5)$$

Since $|\Delta| \geq \delta$ and $\varepsilon_h \ll \delta$, we have $R(s; s - \Delta) \approx |\Delta|$. Writing $\mathbf{R} = \Delta \mathbf{e}_z + \varepsilon_h \mathbf{d}(s; s - \Delta)$ and $\mathbf{t}(s - \Delta) = \mathbf{e}_z + \varepsilon_h \mathbf{t}_\perp(s - \Delta)$ where $\mathbf{t}_\perp(s - \Delta) = \left(\frac{\partial x^{(2)}}{\partial s'}, \frac{\partial y^{(2)}}{\partial s'}, 0 \right) \Big|_{s' = s - \Delta}$, the integrand from Eq. 4.5 is given by

$$\varepsilon_h \boldsymbol{\omega}^{(2)}(s - \Delta) [\mathbf{e}_z \times \mathbf{d}(s; s - \Delta) + \mathbf{t}_\perp(s - \Delta) \times \Delta \mathbf{e}_z] \frac{1}{|\Delta|^3}. \quad (4.6)$$

The leading-order term in Eq. 4.6 diverges as $1/\Delta^3$ in the limit $\delta \rightarrow 0$, leading to a final asymptotic integral as

$$\mathbf{v}_M^{\text{NL}} = \frac{\varepsilon_a^2 \varepsilon_h}{2} \left(\int_{-\delta}^{s-1} + \int_\delta^s \right) \boldsymbol{\omega}^{(2)}(s - \Delta) \mathbf{e}_z \times \mathbf{d}(s; s - \Delta) \frac{d\Delta}{\Delta^3}. \quad (4.7)$$

In the limit where $\delta \rightarrow 0$, the result in Eq. 4.7 diverges and is dominated by the behavior of the integrand near the boundary, i.e. $\delta = 0$. Calling d_0 the local direction between the filaments perpendicular to their long axis, i.e. $d_0 = d(s; s)$ (Fig. 2b), we obtain in the limit $\delta \rightarrow 0$

$$\mathbf{v}_M^{\text{NL}} = \frac{\varepsilon_a^2 \varepsilon_h}{2\delta^2} \boldsymbol{\omega}^{(2)}(s) \mathbf{e}_z \times \mathbf{d}_0, \quad (4.8)$$

at leading order.

Next I consider the local integration where we have

$$\mathbf{v}_M^{\text{L}} = \frac{\varepsilon_a^2}{2} \int_{-\delta}^\delta \boldsymbol{\omega}^{(2)}(s - \Delta) \mathbf{t}^{(2)}(s - \Delta) \frac{\mathbf{R}}{R^3} d\Delta. \quad (4.9)$$

In the local region, we can Taylor-expand $\boldsymbol{\omega}^{(2)}$ and d around $\Delta = 0$ (i.e. around $s' = s$), as

$$\begin{pmatrix} \boldsymbol{\omega}(s - \Delta)^{(2)} \\ \mathbf{d}(s - \Delta) \end{pmatrix} = \begin{pmatrix} \boldsymbol{\omega}(s)^{(2)} \\ \mathbf{d}(s) \end{pmatrix} + \Delta \begin{pmatrix} \boldsymbol{\omega}_{0\Delta}^{(2)} \\ \mathbf{d}_{0\Delta} \end{pmatrix} + O(\Delta^2), \quad (4.10)$$

where under the long-wavelength approximation, the derivatives $\boldsymbol{\omega}^{(2)}$ and $\mathbf{d}_{0\Delta}$ are of order one (i.e. the geometry and the rotation of the filaments vary on the length scale L). In that case, each term in the integrand can be expanded and we get at leading order that only the local values of the rotation rate, $\boldsymbol{\omega}^{(2)}(s)$, and the force, $\mathbf{f}^{(2)}(s)$, enter the problem, with a local flow given by

$$\mathbf{v}_M^{\text{L}} = \frac{\varepsilon_a^2 \varepsilon_h}{2} \boldsymbol{\omega}^{(2)}(s) \int_{-\delta}^\delta \frac{\mathbf{e}_z \times \mathbf{d}_0}{(\Delta^2 + \varepsilon_h^2 d_0^2)^{\frac{3}{2}}} d\Delta, \quad (4.11)$$

which may be evaluated analytically asymptotically as

$$\mathbf{v}_M^L = \frac{\epsilon_a^2 \epsilon_h}{2} \boldsymbol{\omega}^{(2)}(s) \mathbf{e}_z \times \mathbf{d}_0 \left(\frac{2}{\epsilon_h^2 d_0^2} - \frac{1}{\delta^2} \right). \quad (4.12)$$

Adding up Eq. 4.8 and 4.12, we obtain the final flow induced by filament #2, which is independent of the value of δ , given at leading-order by

$$\mathbf{v}_M^{(2) \rightarrow (1)} = \frac{\epsilon_a^2}{\epsilon_h d_0^2} \boldsymbol{\omega}^{(2)}(s) \mathbf{e}_z \times \mathbf{d}_0. \quad (4.13)$$

4.1.3 Point forces (stokeslets)

A similar approach may be used to evaluate the second velocity term, $\mathbf{v}_F^{(2) \rightarrow (1)}$, induced by the forcing of filament #2 on the fluid. In that case, the flow is given by a line integral of stokeslets singularities (point forces) as

$$\mathbf{v}_F^{(2) \rightarrow (1)}(s) = \int_0^L \frac{-\mathbf{f}^{(2)}(s')}{8\pi\mu} \cdot \left(\frac{\mathbf{I}}{R} + \frac{\mathbf{R}\mathbf{R}}{R^3} \right) ds', \quad (4.14)$$

where \mathbf{I} is the identity tensor and $\mathbf{f}^{(2)}$ the force density acting on filament #2. One notable difference between Eq. 4.3 and Eq. 4.14 is that the integrand in Eq. 4.14 is known explicitly (filament rotation), whereas that in Eq. 4.14 has in it the quantity we are trying to determine, specifically the unknown force density, $\mathbf{f}^{(2)}$. We can however proceed as above as long as $\mathbf{f}^{(2)}$ varies on the length scale L , and similarly for the other filament, so that the resulting velocities in Eq. 4.1 will lead to a linear system to invert to determine both $\mathbf{f}^{(1)}$ and $\mathbf{f}^{(2)}$. After nondimensionalizing force densities by $8\pi\mu L/T$, the nonlocal contribution of the integral in Eq. 4.14 is written as

$$\mathbf{v}_F^{\text{NL}} = - \left(\int_{s-1}^{-\delta} + \int_{\delta}^s \right) \left(\frac{\mathbf{I}}{R} + \frac{\mathbf{R}\mathbf{R}}{R^3} \right) \cdot \mathbf{f}^{(2)}(s-\Delta) d\Delta. \quad (4.15)$$

In the non-local region we have $R(s; s-\Delta) \approx |\Delta|$ and $\mathbf{R} \approx \Delta \mathbf{e}_z$ and thus obtain

$$\mathbf{v}_{F0}^{\text{NL}} = - \left(\int_{s-1}^{-\delta} + \int_{\delta}^s \right) \frac{\mathbf{f}^{(2)}(s-\Delta)}{|\Delta|} + \frac{\Delta^2 [\mathbf{f}^{(2)}(s-\Delta) \cdot \mathbf{e}_z] \mathbf{e}_z}{|\Delta|^3} d\Delta \quad (4.16a)$$

$$= -[\mathbf{I} + \mathbf{e}_z \mathbf{e}_z] \cdot \left(\int_{s-1}^{-\delta} + \int_{\delta}^s \right) \frac{\mathbf{f}^{(2)}(s-\Delta)}{|\Delta|} d\Delta. \quad (4.16b)$$

Here again the asymptotic behaviour in the limit $\delta \rightarrow 0$ is dominated by the behavior near $\Delta = 0$ and we obtain

$$\mathbf{v}_F^{\text{NL}} = -[\mathbf{I} + \mathbf{e}_z \mathbf{e}_z] \cdot \mathbf{f}^{(2)}(s) \left(\int_{-\delta}^{s-1} + \int_{\delta}^s \right) \frac{d\Delta}{\Delta}. \quad (4.17)$$

whose evaluation at leading-order value is given by the logarithmic term

$$\mathbf{v}_F^{\text{NL}} = 2(\ln \delta)(\mathbf{I} + \mathbf{e}_z \mathbf{e}_z) \cdot \mathbf{f}^{(2)}(s). \quad (4.18)$$

Next the local integration is given by the integral of

$$\mathbf{v}_F^{\text{L}} = - \int_{-\delta}^{\delta} \left(\frac{\mathbf{I}}{R} + \frac{\mathbf{R}\mathbf{R}}{R^3} \right) \cdot \mathbf{f}^{(2)} d\Delta. \quad (4.19)$$

In the local region, the force can be Taylor-expanded as

$$\mathbf{f}^{(2)} = \mathbf{f}^{(2)}(s) + \Delta \frac{\partial \mathbf{f}^{(2)}}{\partial \Delta} \Big|_{\Delta=0} \equiv \mathbf{f}^{(2)}(s) + \Delta \mathbf{f}_{0\Delta}, \quad (4.20)$$

where again we assume that $\mathbf{f}_{0\Delta} = O(1)$ under the long-wavelength approximation (i.e. the relevant length scale describing the variations of the force is the length of the filaments, L).

Substitute into Eq. 4.19, we get at leading order that only the local value of the force, $\mathbf{f}^{(2)}(s)$, enters the problem, with a local flow given by

$$\mathbf{v}_F^{\text{L}} = - \int_{-\delta}^{\delta} \frac{\mathbf{f}^{(2)}(s)}{\sqrt{\Delta^2 + \epsilon_h^2 d_0^2}} + \frac{[(\mathbf{f}^{(2)}(s) \cdot (\Delta \mathbf{e}_z + \epsilon_h \mathbf{d}_0))][\Delta \mathbf{e}_z + \epsilon_h \mathbf{d}_0]}{(\Delta^2 + \epsilon_h^2 d_0^2)^{3/2}} d\Delta \quad (4.21a)$$

$$= - \int_{-\delta}^{\delta} \left(\frac{\mathbf{f}^{(2)}(s)}{\sqrt{\Delta^2 + \epsilon_h^2 d_0^2}} + \frac{\Delta^2 (\mathbf{f}^{(2)}(s) \cdot \mathbf{e}_z) \mathbf{e}_z}{(\Delta^2 + \epsilon_h^2 d_0^2)^{3/2}} + \frac{\epsilon_h^2 (\mathbf{f}^{(2)}(s) \cdot \mathbf{d}_0) \mathbf{d}_0}{(\Delta^2 + \epsilon_h^2 d_0^2)^{3/2}} \right) d\Delta. \quad (4.21b)$$

While the first two integrand each give a value which diverges in the limit $\delta \rightarrow 0$, the third term does not, and can be neglected. We are left with two integrals. Using the integrations

$$\int \frac{du}{(1+u^2)^{1/2}} = \ln \left(u + \sqrt{1+u^2} \right), \quad (4.22a)$$

$$\int \frac{u^2 du}{(1+u^2)^{3/2}} = \ln \left(u + \sqrt{1+u^2} \right) - \frac{u}{(1+u^2)^{1/2}}, \quad (4.22b)$$

we are able to evaluate

$$-\int_{-\delta}^{\delta} \frac{\mathbf{f}^{(2)}(s)}{\sqrt{\Delta^2 + \varepsilon_h^2 d_0^2}} d\Delta = 2 \ln \left(\frac{\varepsilon_h d_0}{\delta} \right) \mathbf{f}^{(2)}(s) \quad (4.23)$$

and

$$-\int_{-\delta}^{\delta} \frac{\Delta^2 (\mathbf{f}^{(2)}(s) \cdot \mathbf{e}_z) \mathbf{e}_z}{(\Delta^2 + \varepsilon_h^2 d_0^2)^{3/2}} d\Delta = 2 \ln \left(\frac{\varepsilon_h d_0}{\delta} \right) [\mathbf{e}_z \cdot \mathbf{f}^{(2)}(s)] \mathbf{e}_z \quad (4.24)$$

so that the local term is finally given by

$$\mathbf{v}_F^L = 2 \ln \left(\frac{\varepsilon_h d_0}{\delta} \right) (\mathbf{I} + \mathbf{e}_z \mathbf{e}_z) \cdot \mathbf{f}^{(2)}(s). \quad (4.25)$$

Adding the nonlocal term with the local term, Eqs. 4.18 and 4.25, we obtain

$$\mathbf{v}_F^{(2) \rightarrow (1)} = 2 \ln (\varepsilon_h d_0) (\mathbf{I} + \mathbf{e}_z \mathbf{e}_z) \cdot \mathbf{f}^{(2)}(s), \quad (4.26)$$

for the velocity induced by the unknown force density.

4.1.4 Dimensional results

Returning to dimensional quantities Eqs. 4.13 and 4.26 can be written as

$$\mathbf{v}_M^{(2) \rightarrow (1)} = \left(\frac{a}{h(s)} \right)^2 \boldsymbol{\omega}^{(2)}(s) \mathbf{e}_z \times \mathbf{h}(s) \quad (4.27a)$$

$$\mathbf{v}_F^{(2) \rightarrow (1)} = \frac{1}{4\pi\mu} \ln \left[\frac{h(s)}{L} \right] (\mathbf{I} + \mathbf{e}_z \mathbf{e}_z) \cdot \mathbf{f}^{(2)}(s), \quad (4.27b)$$

where $\mathbf{h}(s)$ is the dimensional local vector between the filaments, i.e. $\mathbf{h}(s) = \mathbf{r}_1(s) - \mathbf{r}_2(s)$, and $h(s)$ its norm.

The results in Eq. 4.27, together with Eq. 4.1 are the main new results of this work. They provide a linear, local, relationship between the force density on each filament ($\mathbf{f}^{(i)}$) and the kinematics of their motion ($\boldsymbol{\omega}^{(j)}$ and $\partial \mathbf{r}(j)/\partial t$). While derived only in the case of two filaments with main directions parallel, these results are easily generalisable to the case of $N > 2$ non-parallel filaments. As a remark, we note that one is not allowed to formally take the limit $h \rightarrow 0$ or $h \rightarrow \infty$ in Eq. 4.27, as both violate the limit $a \ll h \ll L$ in which these formulae were derived.

4.2 An example of planar motion

For planar motion ($\omega^{(j)} = 0$ for $j = 1, 2$), the algebra simplifies further. In Eq. 4.1, since $h \ll L$, the tangent vectors are $\mathbf{t} = \mathbf{e}_z$ at leading order in h/L and since $\xi_{\perp} \approx 2\xi_{\parallel}$ [88] we have for each filament $\xi_{\perp}\mathbf{I} + (\xi_{\parallel} - \xi_{\perp})\mathbf{t}\mathbf{t} \approx \xi_{\perp}[\mathbf{I} - \frac{1}{2}\mathbf{e}_z\mathbf{e}_z] \equiv \mathbf{J}$, so that on each filament i we have the dynamic balance

$$\mathbf{f}^{(i)}(s, t) - \mathbf{J} \cdot \mathbf{v}^{(j) \rightarrow (i)} = -\mathbf{J} \cdot \frac{\partial \mathbf{r}^{(i)}}{\partial t}, \quad (4.28)$$

with $j \neq i$. Given the tensorial operator appearing in Eq. 4.27b, we have to evaluate

$$\left(\mathbf{I} - \frac{1}{2}\mathbf{e}_z\mathbf{e}_z\right) \cdot (\mathbf{I} + \mathbf{e}_z\mathbf{e}_z) = \mathbf{I}, \quad (4.29)$$

and we further note that $\xi_{\perp}/4\pi\mu \approx 1/\ln(1/\varepsilon_a)$ [88]. As a result, Eq. 4.28 simplifies for each filament to

$$\mathbf{f}^{(i)}(s, t) + \frac{\ln(h(s, t)/L)}{\ln(a/L)} \mathbf{f}^{(j)}(s, t) = -\mathbf{J} \cdot \frac{\partial \mathbf{r}^{(i)}}{\partial t}, \quad (4.30)$$

with $j \neq i$. Defining $\lambda(s, t) \equiv \ln(h(s, t)/L)/\ln(a/L)$ and $\Lambda(s, t) \equiv 1 - \lambda^2(s, t)$ (note that $\Lambda > 0$ since $a < h$), this linear system can be inverted by hand and we obtain the analytical formula for the force density $\mathbf{f}^{(i)}(s, t)$ acting on filament i as

$$\mathbf{f}^{(i)}(s, t) = -\frac{1}{\Lambda(s, t)} \mathbf{J} \cdot \left(\frac{\partial \mathbf{r}^{(i)}}{\partial t} - \lambda(s, t) \frac{\partial \mathbf{r}^{(j)}}{\partial t} \right). \quad (4.31)$$

I now illustrate predictions of my theory on a simple model of two rigid filaments undergoing planar motion, and compare with numerical slender-body simulations. Consider two planar filaments of radius a , length L with centerlines located at $[0, \varepsilon y_1(z, t), z]$ and $[0, h_0 + \varepsilon y_2(z, t), z]$. Assume for simplicity small amplitude motion $\varepsilon \ll 1$ and let us use our results to calculate the force density in the y direction, $f^{(i)} = \mathbf{f}^{(i)} \cdot \mathbf{e}_y$, in powers of the amplitude ($f^{(i)} = \varepsilon f_1^{(i)} + \varepsilon^2 f_2^{(i)} + \dots$) in the limit $a \ll h \ll L$. Writing $h = h_0 + \varepsilon h_1$, a Taylor expansion gives $\ln(h/L) = \ln(h_0/L) + \varepsilon_1/h_0 + O(\varepsilon^2)$, which we use to evaluate Eq. 4.31 at order ε , leading to

$$f_1^{(i)} = \frac{\xi_{\perp}}{1 - [\ln(h_0/L)/\ln(a/L)]^2} \left(\frac{\ln(h_0/L)}{\ln(a/L)} \frac{\partial y^{(j)}}{\partial t} - \frac{\partial y^{(i)}}{\partial t} \right). \quad (4.32)$$

At order ε^2 , Eq. 4.30 becomes

$$f_2^{(i)} + \frac{\ln(h_0/L)}{\ln(a/L)} f_2^{(j)} = -\frac{h_1}{h_0 \ln(a/L)} f_1^{(j)}, \quad (4.33)$$

Assuming that both y_1 and y_2 are periodic in time on the same period, then a time-average of Eq. 4.32 using Eq. 4.33 leads to identical mean force densities along both filaments as $\langle f_1^{(1)} \rangle = \langle f_2^{(2)} \rangle = f_2(s)$, where

$$f_2(s) = \frac{\xi_\perp \ln(a/L)}{2h_0[\ln(h_0/L) + \ln(a/L)]^2} \left\langle y_- \frac{\partial y_+}{\partial t} \right\rangle, \quad (4.34)$$

with $y_+ \equiv y^{(1)} + y^{(2)}$ and $y_- \equiv y^{(2)} - y^{(1)}$. For illustration purposes, let us assume that the first filament undergoes sinusoidal rigid-body motion of the form $y_1(t) = R(\sum_n \ln \exp i n \omega t)$ while the second filament has the same motion with a phase difference ϕ , i.e. $y_2(t) = y_1(t + \phi)$. Our theory, Eq. 4.34, predicts that the two-rod system will pump the fluid by exerting a net force on it, F , of magnitude

$$F_2 = \frac{4\pi\mu\omega L}{2h_0[\ln(h_0/L) + \ln(a/L)]^2} \sum_n n |l_n|^2 \sin(n\phi). \quad (4.35)$$

Clearly Eq. 4.35 predicts zero net force for in-phase ($\phi = 0$) and out-of-phase ($\phi = \pi$) motion and thus an optimal phase difference between the two filaments exists. We test in Fig. 3 this theoretical prediction against a numerical implementation of non-local slender-body appropriate for interactions [65] in the case $n = 1$. We numerically solve for the force distribution along each filament using a Galerkin method based on Legendre polynomials. The net force on each filament is then computed at 15 equidistant points within a period, and the mean force calculated. While the theoretical approach (Eq. 28) was derived only asymptotically in the limit where $a/h \rightarrow 0$ and $h/L \rightarrow 0$ we see that even when these parameters are not asymptotically small (here $a/h = 0.25$ and $h/L = 0.1$), the theoretical prediction (solid line) is able to capture the computational results (dashed line and symbols) with good approximation. In contrast, far-field predictions are off by more than two orders of magnitude.

4.3 Discussion

In summary, I have used an asymptotic method to compute the hydrodynamic interactions between nearby filaments undergoing arbitrary rotation and translation. The key ingredient allowing the calculation to be carried out is to exploit the separation of length scales $a \ll h \ll$

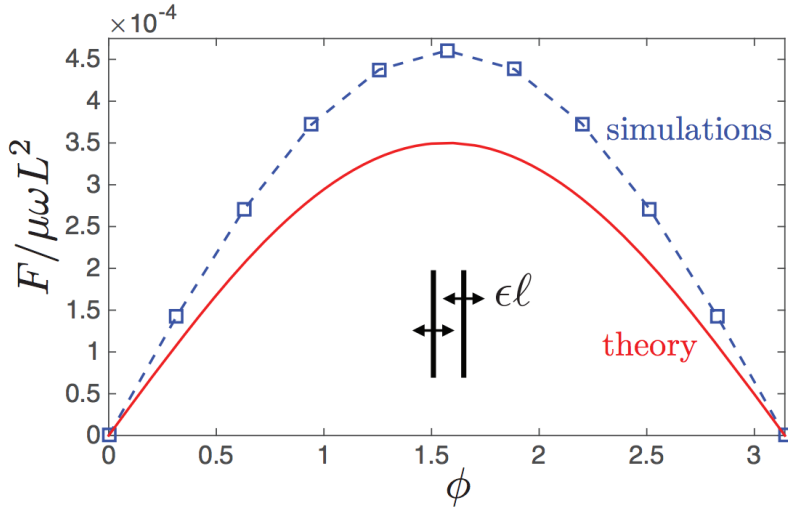


Fig. 4.3 Fig. 3: Net force induced on the fluid by a two-rod pump, $F/\mu\omega L^2$, as a function of the phase difference, ϕ , between the rods. Dashed line and symbols: slender-body theory simulations; Solid line: theory (eq. (4.35)). The dimensionless distance between the rods is $h/L = 0.1$, their aspect ratio $a/L = 0.025$ (so that $a/h = 0.25$) and the motion amplitude is $\epsilon\ell = h/10$.

L which enables a representation of the flow as a superposition of fundamental singularities whose strengths vary only on long wavelengths compared to the separation between the filaments.

Like any other asymptotic derivation, a crucial question in this work is that of the magnitude of the error (i.e. the order of the next-order terms). To fix ideas, consider first a single filament undergoing planar deformation with a centerline described by $[x, y(x, t)]$. The classical formula for the leading-order force density, f , on the filament is $\mathbf{f} = -(\xi_\perp \partial y / \partial t) \mathbf{e}_y$, with (i) logarithmic corrections in the aspect ratio of the filament from next-order terms beyond resistive-force theory, i.e. relative error $O(1/\ln(L/a))$ and (ii) algebraic corrections in the typical slope of the filament, i.e. relative error $O(h/L)$ due to the difference between the true instantaneous geometry of the filament and its mean direction [77]. The same relative errors apply to our current work. Additional errors arise in our work near the ends of the filaments. Specifically, in order for the non-local integrations to be carried out near the ends of the filaments, the arclength s needs to satisfy $h \ll \min(s, L-s)$, with logarithmically (resp. algebraically) small relative errors in $h/\min(s, L-s)$ from filament translation (resp. rotation). Physically, this logarithmic accuracy of local hydrodynamics is the equivalent to that of resistive-force theory but extended to multiple filaments. Note that since $h \ll L$, the results are still able to provide the value of the hydrodynamic force density on the majority of the filaments. I finally point out that while the addition of higher-order flow singularities than

rotlet and stokeslets along each filament would improve the analysis, the resulting additional terms would decay spatially algebraically and faster than the terms in Eq. 4.27, which provide thus the leading-order contribution in the limit $a \ll h \ll L$.

The framework developed in this work will allow to address theoretically a number of problems on the biomechanics of filaments where nonlocal hydrodynamic interactions may be integrated out analytically for example in cytoskeletal mechanics, hydrodynamic interactions and cellular propulsion, beyond the classical, complementary, far-field approach.

Chapter 5

Bundling of elastic filaments from hydrodynamic interactions

One particular example involves hydrodynamic interaction is flagellar bundling and unbundling for petrichous bacteria (Fig. 1.1), which have attracted a lot of attention in recent years. The presence of multiple flagella allow bacteria to undergo random walk-like trajectories where long straight swimming ‘runs’ (~ 1 s) are interrupted by short ‘tumbles’ (~ 0.1 s) during which the cells randomly reorient [12, 95, 96]. During the run phase, all flagella take a normal left-handed shape and are rotated in a counter-clockwise direction (CCW, when viewed from outside the cell behind the flagella) by specialised rotatory motors embedded in the cell wall. During a tumble, at least one motor switches its rotation direction to clockwise (CW), the corresponding flagella fly out of the bundle and change their helical pitch, amplitude and handedness as governed by biochemistry [22, 60, 133]. This in turn leads to a modification of the force balance on the whole cell and its reorientation. At the end of a tumble, all motors return to a CCW rotation, and the splayed flagella reintegrate into the normal left-handed helical bundle behind the cell, then resumes swimming along a straight line.

Given its relevance to one of the most fundamental forms of mobility on the planet, the role of fluid dynamics in this process has received a lot of attention from the research community. Experimentally, a macro-scale version of the interactions between rotated helices [71], and subsequent flow measurements [72], showed that hydrodynamic interactions alone were able to lead to wrapping of flexible helical filaments consistent with experimental observations at the cellular scale [133]. Computationally, the issue of synchronization between rotating helices was addressed [72, 109], and similarly for rotating paddles [6]. Full simulations of the bundling process were carried using a variety of computational methods including the use of regularized flow singularities [41], multi-particle collision dynamics

[110, 112], finite differences [64], the immersed boundary method [92], beads-spring models [136] and the boundary element method [67].

The process by which the flagella of peritrichous bacteria interact, repeatedly come together and separate is complex and involves at least three important mechanical aspects: hydrodynamic interactions between the rotating helical filaments [95, 71, 41, 109, 110, 92, 112, 67, 64], elasticity and deformation from the short flexible hook joining the rotary motors to the flagellar filaments [109, 20] and interactions between the filaments and the rotating body of the cell [106, 3].

In parallel to these significant computational advances, theoretical studies have not been able yet to derive simplified models allowing it capture, from first principle, the essence of the dynamics of the bundling and unbundling process. In this chapter, I derive the tools required to build such a model and apply it to the case of two rotated straight filaments. Taking advantage of a separation of length scales for slender filaments I show that in the long-wavelength limit the shape of the filament, obeying a balance between hydrodynamic and elastic forces, satisfies a local nonlinear partial differential equation. Crucial to the derivation of this equation is the integration of non-local hydrodynamic interactions which can be done by hand in the long-wavelength limit [51, 98]. Then I study the dynamics predicted by our model numerically and reveal the presence of two configuration instabilities, first to a ‘crossing’ state where filaments touch as one point and then to a ‘bundled’ state where filaments wrap along each other in a helical fashion. The derivations, which provide a simplified approach to capture the dynamics of bundling and unbundling, should be applicable to a wide range of problems in biological mechanics where slender filaments interact hydrodynamically.

5.1 Interactions between two elastic filaments

5.1.1 Set-up

To address flagellar bundling as a balance between hydrodynamics and elasticity, I set up a very simplified model illustrated in Fig. 5.1. Two naturally straight elastic filaments of length L and radius a are rotated at their clamped ends by imposed rotation rates $\omega_0^{(i)}$ where $i = 1, 2$ refers to the filament number. The filaments are initially parallel and separated by a distance h_0 . The filaments are assumed to be located in a viscous fluid of viscosity μ . As a result, their rotation set up rotational flows and, with the other ends of both filaments free, will lead a helical wrapping driven purely by hydrodynamic interactions. Note that in general the two rotation rates of the filaments are allowed to be different; however, in most of the

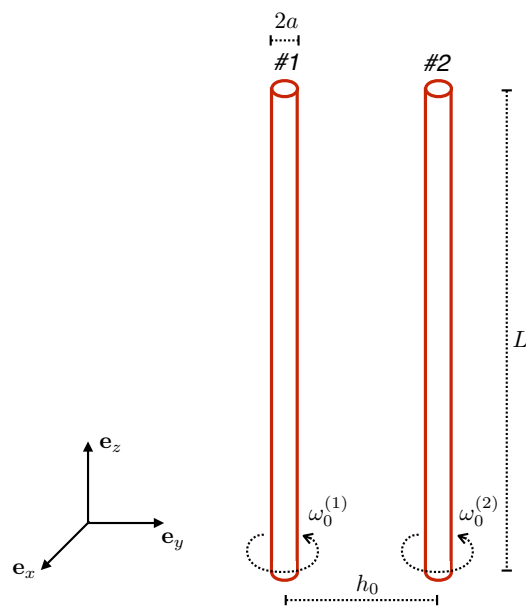


Fig. 5.1 A simplified model of flagellar bundling. Two parallel elastic filaments of length L and radius a are separated by a mean distance h_0 . Both filaments are rotated with speed $\omega_0^{(i)}$ ($i = 1, 2$) in a viscous fluid from their clamped end while their other end remains mechanically free. We use cartesian coordinates with z along the filaments and x, y perpendicular to it.

cases studied below we will consider identical rotation rate, i.e. $\omega_0^{(i)} = \omega_0$. Note also that while we focus our initial derivation to two filaments, the results will generalised later in the paper to the case of $N > 2$ filaments.

In order to derive an analytical model of the dynamics, we need to make a further assumption. Looking at the typical dimensions of flagellar filament of bacteria, we see that the three relevant length scales a , h_0 , and L are often in the limit where there is a clear scale separation, $a \ll h_0 \ll L$. As an illustrative example, consider the flagellar filaments of *E. coli*. Each filament has a typical length $L \approx 10 \mu\text{m}$ and radius $a \approx 10 \text{ nm}$. The cell body takes approximately the shape of a prolate ellipsoid of $1 \mu\text{m}$ width and $2 \mu\text{m}$ length [133, 10]. Assuming the same scale as the body size, the distance between the proximal ends of the flagellar filaments can be thus estimated to be around $h_0 \approx 1 \mu\text{m}$. These numbers lead therefore to ratios $a/h_0 \sim 10^{-2}$ and $h_0/L \sim 10^{-1}$, which confirms this separation of scales.

Mathematically, placing ourselves in the limit $a \ll L$ means that each filament is slender and we will be able to make use of resistive-force theory to compute hydrodynamic forces. The limit $h_0 \ll L$ means that the filaments are not in the far-field limit but in the opposite limit where all long-range hydrodynamic interactions have to be included. Furthermore, given that their separation will remain at most h_0 , this means that we will be able to treat the problem in the long-wavelength limit, a crucial step to derive an analytical model. Finally, the limit $a \ll h_0$ means that lubrication stresses can be ignored and the flow can be accurately captured by a superposition of hydrodynamic singularities.

5.1.2 Force balance

Focusing on small-scale systems, we remain safely in the low-Reynolds number regime, and therefore the force balance on each filament is written instantaneously as

$$\mathbf{f}_h^{(i)}(s, t) + \mathbf{f}_e^{(i)}(s, t) = 0, \quad (5.1)$$

where $\mathbf{f}_h^{(i)}(s, t)$ and $\mathbf{f}_e^{(i)}(s, t)$ refer, respectively, to the hydrodynamic and elastic forces per unit length acting along filament i and where s refers to the arclength along the filament ranging from $s = 0$ (clamped end) to $s = L$ (free end). I denote the position vector of filament i as $\mathbf{r}^{(i)}(s, t)$.

5.1.3 Kinematics

Assuming that all displacements remain on the order of h_0 , it is natural to describe the shapes of the filaments using Cartesian coordinates (Fig. 5.1) as

$$\mathbf{r}^{(i)}(s, t) = [h_0 x^{(i)}(s, t), h_0 y^{(i)}(s, t), s] = \left[h_0 \zeta^{(i)}(s, t), h_0 \left(\mp \frac{1}{2} + \eta^{(i)}(s, t) \right), s \right], \quad (5.2)$$

where $[x^{(i)}, y^{(i)}]$ and $[\zeta^{(i)}, \eta^{(i)}]$ denote the filament position and displacement scaled by h_0 , respectively.

5.2 Calculation of elastic force density

5.2.1 Classical rod theory

First let us compute the elastic force density, \mathbf{f}_e , arising in Eq. 5.1. Notation-wisely, we drop for simplicity the upper index (i) and consider one specific filament. For an inextensible elastic filament able to both bend and twist, it is a classical result that \mathbf{f}_e contains three terms, namely [138, 107]

$$\mathbf{f}_e = -A \frac{\partial^4 \mathbf{r}}{\partial s^4} + C \left[\Omega \left(\frac{\partial \mathbf{r}}{\partial s} \times \frac{\partial^2 \mathbf{r}}{\partial s^2} \right) \right]_s - \left[\Lambda \frac{\partial \mathbf{r}}{\partial s} \right]_s. \quad (5.3)$$

In Eq. 5.3 the coefficients A, C are the bending and twisting moduli of the filament, respectively, Ω is the twist density and Λ is the Lagrange multiplier (tension) enforcing the inextensibility of the filament. The conservation law for twist density (often referred to as the compatibility equation) is [107]

$$\frac{\partial \Omega}{\partial t} = \frac{\partial \omega}{\partial s} + \frac{\partial \mathbf{r}}{\partial s} \times \frac{\partial^2 \mathbf{r}}{\partial s^2} \cdot \left[\frac{\partial \mathbf{r}}{\partial t} \right]_s, \quad (5.4)$$

where ω , a notation shorthand for $\omega^{(i)}(s, t)$, is the local rotation rate of the filament around its local centerline. In addition, the local torque balance along the filament is written as

$$C \frac{\partial \Omega}{\partial s} = \xi_r \omega, \quad (5.5)$$

where $\xi_r \approx 4\pi\mu a^2$ is the local drag coefficient for rotation around the filament centerline. Substituting Eq. 5.5 into Eq. 5.4 classically leads to a forced diffusion equation for the twist

density as

$$\frac{\partial \Omega}{\partial t} = \frac{C}{\xi_r} \frac{\partial^2 \Omega}{\partial s^2} + \frac{\partial \mathbf{r}}{\partial s} \times \frac{\partial^2 \mathbf{r}}{\partial s^2} \cdot \left[\frac{\partial \mathbf{r}}{\partial t} \right]_s. \quad (5.6)$$

5.2.2 Separation of time scales

In order to appreciate the relative magnitude of each term in Eq. 5.3, I consider the physical scalings of the various quantities of interest. The relevant time scale in Eq. 5.6 is a diffusion time, T_t , scaling as

$$T_t = \frac{\xi_r L^2}{C}. \quad (5.7)$$

In contrast, balancing Eq. 5.3 with an usual hydrodynamic drag term of the form $\sim \xi_\perp \partial \mathbf{r} / \partial t$, reveals that the relevant bending time scale in Eq. 5.3 is a hyper-diffusion time, T_b , scaling as

$$T_b = \frac{\xi_\perp L^4}{A}. \quad (5.8)$$

In the slender limit $L/a \gg 1$ we have the classical result for the drag coefficient [31, 82]

$$\xi_\perp \approx \frac{4\pi\mu}{\ln(L/a)}, \quad (5.9)$$

and therefore, after introducing the ratio Γ of elastic modulus,

$$\Gamma = \frac{C}{A}, \quad (5.10)$$

we obtain that the ratio of twist to bending relaxation time scales is given by the scaling

$$\frac{T_t}{T_b} \sim \frac{\varepsilon_a^2 \ln(1/\varepsilon_a)}{\Gamma}, \quad (5.11)$$

where we have defined $\varepsilon_a \equiv a/L$, a small number in the slender limit. Clearly Eq. 5.11 indicates that $T_t \ll T_b$. Since T_b is the time scale relevant to describe the shape of the filaments, we will be able to separate the time scales and consider the twist problem solved in a quasi-steady fashion [137].

5.2.3 Non-dimensionalisation

We proceed by nondimensionalising the equations using the length scale L and time scale T_b as the relevant dimensions and we use bars to denote dimensionless variables. Following

Eq. 5.2, we write for the position of the filament

$$\bar{\mathbf{r}} = [\varepsilon_h \bar{x}, \varepsilon_h \bar{y}, \bar{s}], \quad (5.12)$$

where we have defined a second dimensionless number $\varepsilon_h \equiv h_0/L$, which is assumed to be small. Writing as well

$$\bar{s} = s/L, \quad \bar{\Lambda} = \Lambda \frac{L^2}{A}, \quad \bar{\mathbf{f}}_e = \mathbf{f}_e \frac{L^3}{A}, \quad \bar{\Omega} = \Omega L. \quad (5.13)$$

we obtain the dimensionless equations as

$$\bar{\mathbf{f}}_e = -\frac{\partial^4 \bar{\mathbf{r}}^{(i)}}{\partial \bar{s}^4} + \Gamma \left[\bar{\Omega} \left(\frac{\partial \bar{\mathbf{r}}}{\partial \bar{s}} \times \frac{\partial^2 \bar{\mathbf{r}}}{\partial \bar{s}^2} \right) \right]_{\bar{s}} - \left[\bar{\Lambda} \frac{\partial \bar{\mathbf{r}}}{\partial \bar{s}} \right]_{\bar{s}}, \quad (5.14a)$$

$$\frac{\partial \bar{\Omega}}{\partial \bar{t}} = \frac{\Gamma}{\varepsilon_a^2 \ln(1/\varepsilon_a)} \frac{\partial^2 \bar{\Omega}}{\partial \bar{s}^2} + \frac{\partial \bar{\mathbf{r}}}{\partial \bar{s}} \times \frac{\partial^2 \bar{\mathbf{r}}}{\partial \bar{s}^2} \cdot \left[\frac{\partial \bar{\mathbf{r}}}{\partial \bar{t}} \right]_{\bar{s}}. \quad (5.14b)$$

Note finally that the imposed rotation is nondimensionalised as $\bar{\omega}_0 = \omega_0 T_b$, and the result is related to the classical dimensionless Sperm number, Sp , quantifying a balance between elastic and viscous drag as [82]

$$\bar{\omega}_0 = \frac{\xi_\perp \omega_0 L^4}{A} \equiv \text{Sp}^4. \quad (5.15)$$

5.2.4 Twist equilibrium

For convenience, let us now drop the ‘bar’ notation in what follows, and except where explicitly stated results should be assumed to be dimensionless.

Given the separation of time scales by Eq. 5.11, we expect the first term on the right-hand of Eq. 5.14b to dominate and thus with the boundary condition at the clamped and free ends,

$$\frac{\partial \Omega}{\partial s}(s=0) = \frac{\varepsilon_a^2 \ln(1/\varepsilon_a)}{\Gamma} \omega_0, \quad \Omega(s=1) = 0, \quad (5.16)$$

the twist density is given in quasi-steady equilibrium by a simple linear function

$$\Omega = \frac{\varepsilon_a^2 \ln(1/\varepsilon_a)}{\Gamma} \omega_0 (s-1). \quad (5.17)$$

Substituting this result into Eq. 5.14a, we obtain the explicit formula for the elastic force density as

$$\mathbf{f}_e = -\frac{\partial^4 \mathbf{r}}{\partial s^4} + \omega_0 \varepsilon_a^2 \ln \varepsilon_a \left[(1-s) \left(\frac{\partial \mathbf{r}}{\partial s} \times \frac{\partial^2 \mathbf{r}}{\partial s^2} \right) \right]_s - \left[\Lambda \frac{\partial \mathbf{r}}{\partial s} \right]_s. \quad (5.18)$$

5.2.5 Scalings

In order to make further progress, we next compare the expected magnitude of each term in Eq. 5.18. The first two terms clearly scale as

$$\frac{\partial^4 \mathbf{r}}{\partial s^4} \sim \varepsilon_h, \quad (5.19a)$$

$$\omega_0 \varepsilon_a^2 \ln \varepsilon_a \left[(1-s) \left(\frac{\partial \mathbf{r}}{\partial s} \times \frac{\partial^2 \mathbf{r}}{\partial s^2} \right) \right]_s \sim \varepsilon_h \varepsilon_a^2 \ln(1/\varepsilon_a) S p^4. \quad (5.19b)$$

In order to derive the scaling for the third term, we need to carefully examine the equation for the tension, Λ .

5.2.6 Tension

In order to solve for Langrange multiplier Λ explicitly, we consider the original equation for the force density, Eq. 5.3. The inextensibility condition is mathematically written $\mathbf{r}_s \cdot \mathbf{r}_s = 1$ or $\mathbf{r}_{ts} \cdot \mathbf{r}_s = 0$, where we use superscripts to denote partial derivatives. We next compute the s derivative of the force density as

$$\begin{aligned} \mathbf{f}_s &= \left(\mathbf{I} - \frac{1}{2} \mathbf{r}_s \mathbf{r}_s \right) \cdot (\mathbf{r}_{ts} - \mathbf{v}_s) - \frac{1}{2} (\mathbf{r}_{ss} \mathbf{r}_s + \mathbf{r}_s \mathbf{r}_{ss}) \cdot (\mathbf{r}_t - \mathbf{v}) \\ &= \mathbf{r}_{ts} - \left(\mathbf{I} - \frac{1}{2} \mathbf{r}_s \mathbf{r}_s \right) \cdot \mathbf{v}_s - \frac{1}{2} (\mathbf{r}_{ss} \mathbf{r}_s + \mathbf{r}_s \mathbf{r}_{ss}) \cdot (\mathbf{r}_t - \mathbf{v}), \end{aligned} \quad (5.20)$$

and now aim to simplify all terms involving time derivatives in Eq. 5.3. Since $\mathbf{r}_s \cdot \mathbf{r}_s = 1$, it is clear that a derivative of this equation leads to $\mathbf{r}_s \cdot \mathbf{r}_{ss} = 0$. Evaluating next the dot product $\mathbf{f}_s \cdot \mathbf{r}_s$ we have

$$\begin{aligned} \mathbf{f}_s \cdot \mathbf{r}_s &= -\mathbf{v}_s \cdot \mathbf{r}_s + \frac{1}{2} \mathbf{v}_s \cdot \mathbf{r}_s - \frac{1}{2} \mathbf{r}_{ss} \cdot (\mathbf{r}_t - \mathbf{v}) \\ &= -\frac{1}{2} \mathbf{v}_s \cdot \mathbf{r}_s - \frac{1}{2} \mathbf{r}_{ss} \cdot (\mathbf{r}_t - \mathbf{v}). \end{aligned} \quad (5.21)$$

We then calculate $\mathbf{f} \cdot \mathbf{r}_{ss}$ as

$$\mathbf{f} \cdot \mathbf{r}_{ss} = \mathbf{r}_{ss} \cdot (\mathbf{r}_t - \mathbf{v}), \quad (5.22)$$

and can now eliminate all terms involving time derivatives by combining these equations as

$$2\mathbf{f}_s \cdot \mathbf{r}_s + \mathbf{f} \cdot \mathbf{r}_{ss} = -\mathbf{v}_s \cdot \mathbf{r}_s. \quad (5.23)$$

Substituting the equation for the elastic force, Eq. 5.3, into Eq. 5.23, we obtain

$$2(\Lambda \mathbf{r}_s)_{ss} \cdot \mathbf{r}_s + (\Lambda \mathbf{r}_s)_s \cdot \mathbf{r}_{ss} = -2\mathbf{r}_{5s} \cdot \mathbf{r}_s + 2\Gamma[\Omega(\mathbf{r}_s \times \mathbf{r}_{ss})]_{ss} \cdot \mathbf{r}_s - \mathbf{r}_{4s} \cdot \mathbf{r}_{ss} + \Gamma[\Omega(\mathbf{r}_s \times \mathbf{r}_{ss})]_s \cdot \mathbf{r}_{ss} + \mathbf{v}_s \cdot \mathbf{r}_s. \quad (5.24)$$

The terms on the left-hand side can be simplified by noting that

$$2(\Lambda \mathbf{r}_s)_{ss} \cdot \mathbf{r}_s + (\Lambda \mathbf{r}_s)_s \cdot \mathbf{r}_{ss} = 2\Lambda_{ss} + \Lambda \mathbf{r}_{3s} \cdot \mathbf{r}_s, \quad (5.25)$$

while the terms on the right-hand side involving the twist density combine into

$$2\Gamma[\Omega(\mathbf{r}_s \times \mathbf{r}_{ss})]_{ss} \cdot \mathbf{r}_s + \Gamma[\Omega(\mathbf{r}_s \times \mathbf{r}_{ss})]_s \cdot \mathbf{r}_{ss} = -\Gamma\Omega\mathbf{r}_s \times \mathbf{r}_{3s} \cdot \mathbf{r}_{ss}. \quad (5.26)$$

The equation for Λ takes therefore the final form

$$2\Lambda_{ss} + \Lambda \mathbf{r}_{3s} \cdot \mathbf{r}_s = -2\mathbf{r}_{5s} \cdot \mathbf{r}_s - \mathbf{r}_{4s} \cdot \mathbf{r}_{ss} - \Gamma\Omega\mathbf{r}_s \times \mathbf{r}_{3s} \cdot \mathbf{r}_{ss} + \mathbf{v}_s \cdot \mathbf{r}_s. \quad (5.27)$$

Since $s = O(1)$, we see that the first term on the left-hand side of Eq. 5.27 provides the leading-order scaling for the magnitude of Λ . This needs to be balanced with the leading-order term on the right-hand side of the equation, which includes three terms scaling respectively as $O(\varepsilon_h^2)$, $O(\varepsilon_h^2 \varepsilon_a^2 \ln(1/\varepsilon_a) Sp^4)$ and $O(\varepsilon_h \mathbf{v})$. Since \mathbf{v} is expected to scale with \mathbf{f} , the term $\mathbf{v}_s \cdot \mathbf{r}_s$ will contribute to a higher orders, and therefore we obtain the scaling for the final term in Eq. 5.18 as

$$\left(\Lambda \frac{\partial \mathbf{r}}{\partial s} \right)_s \sim O(\max\{\varepsilon_h^2, \varepsilon_h^2 \varepsilon_a^2 \ln(1/\varepsilon_a) Sp^4\}). \quad (5.28)$$

5.2.7 Orders of magnitude and final scalings

In order to estimate the relative magnitude of the bending, twisting and tension terms in the case relevant to the bundling of bacterial flagella, we need to examine the numbers applicable in the biological world. Beyond the length scales mentioned above, we may use

past measurements for real biological filaments [61] to obtain the estimates

$$\omega \approx 100 \text{ s}^{-1}, \quad A \approx 10^{-24} - 10^{-22} \text{ Nm}^2. \quad (5.29)$$

These numbers imply that the range in Sperm numbers is $\text{Sp} \approx 3 - 10$. As seen in Section 5.1.1, a typical value for ε_a is around 10^{-3} , and thus we see that

$$\varepsilon_a^2 \ln(1/\varepsilon_a) \text{Sp}^4 \ll 1. \quad (5.30)$$

This in turn means that the tension in Eq. 5.30 scales in fact as

$$\left(\Lambda \frac{\partial \mathbf{r}}{\partial s} \right)_s \sim O(\varepsilon_h^2), \quad (5.31)$$

and that the term in Eq. 5.19b can be neglected when compared with the one in Eq. 5.19a. Since $\varepsilon_h \ll 1$, the tension term in Eq. 5.31 may also be neglected in comparison with the bending term in Eq. 5.19a. In the dynamical regime relevant to the helical filaments of bacteria, the elastic force density is therefore dominated by the bending term and we have the final result

$$\mathbf{f}_e = -\frac{\partial^4 \mathbf{r}}{\partial s^4}. \quad (5.32)$$

5.3 Calculation of hydrodynamic force density

Having evaluated the elastic force density in the limit relevant to the bundling of bacterial flagella, we here consider the second term appearing in Eq. 5.1, namely the hydrodynamic force density. We derive its value in the long-wavelength limit; an early version of this calculation was presented in Chapter 4.

5.3.1 Resistive-force theory

Since the filament is slender ($a \ll L$), the hydrodynamic force density is provided by resistive-force theory, which states that the force is proportional to the local velocity of the filament relative to the background flow [31, 82], as

$$\mathbf{f}_h^{(i)} = - \left[\xi_{\parallel} \mathbf{t}^{(i)} \mathbf{t}^{(i)} + \xi_{\perp} (\mathbf{I} - \mathbf{t}^{(i)} \mathbf{t}^{(i)}) \right] \cdot \left(\frac{\partial \mathbf{r}^{(i)}}{\partial t} - \mathbf{v}^{(j) \rightarrow (i)} \right), \quad (5.33)$$

where $\mathbf{v}^{(j)\rightarrow(i)}$ denotes the flow velocity induced by the motion of filament j near filament i (i.e. hydrodynamic interactions). The tangent vector along the filament is defined as

$$\mathbf{t}^{(i)} = \frac{\partial \mathbf{r}^{(i)}}{\partial s}. \quad (5.34)$$

The hydrodynamic resistance coefficients for motion parallel and perpendicular to the local tangent, ξ_{\parallel} and ξ_{\perp} , approximately satisfy

$$\xi_{\perp} = 2\xi_{\parallel}, \quad (5.35)$$

which leads to a simpler form of Eq. 5.33 as

$$\mathbf{f}_h^{(i)} = -\xi_{\perp} \left[\mathbf{I} - \frac{1}{2} \mathbf{t}^{(i)} \mathbf{t}^{(i)} \right] \cdot \left[\frac{\partial \mathbf{r}^{(i)}}{\partial t} - \mathbf{v}^{(j)\rightarrow(i)} \right]. \quad (5.36)$$

Using the scalings consistent with Eq. 5.13,

$$\bar{\mathbf{f}}_h = \frac{L^3}{A} \mathbf{f}_h, \quad \bar{\mathbf{v}}^{(j)\rightarrow(i)} = \mathbf{v}^{(j)\rightarrow(i)} \frac{\xi_{\perp} L^3}{A}, \quad (5.37)$$

the dimensionless form of Eq. 5.36 is finally given by

$$\bar{\mathbf{f}}_h^{(i)} = - \left[\mathbf{I} - \frac{1}{2} \mathbf{t}^{(i)} \mathbf{t}^{(i)} \right] \cdot \left[\frac{\partial \bar{\mathbf{r}}^{(i)}}{\partial \bar{t}} - \bar{\mathbf{v}}^{(j)\rightarrow(i)} \right]. \quad (5.38)$$

5.3.2 Hydrodynamic interactions

Hydrodynamic interactions between the moving filaments fundamentally arise from two different types of motion, which will be captured by different flow singularities: rotational motion of the filaments around their centreline (fast decaying rotlets) and translational motion (slow decaying stokeslets). The dimensional flow field induced by the motion of filament j near filament i , $\mathbf{v}^{(j)\rightarrow(i)}$, can therefore be split into two terms induced by local moments and forces as

$$\mathbf{v}^{(j)\rightarrow(i)} = \mathbf{v}_M^{(j)\rightarrow(i)} + \mathbf{v}_F^{(j)\rightarrow(i)}. \quad (5.39)$$

Due to the wide-separation assumption, $a \ll h_0$, both \mathbf{v}_M and \mathbf{v}_F can be described by a superposition of flow singularities.

Using $\mathbf{m}^{(j)}$ to denote the torque density acting on filament j , and $\mathbf{R}(s, s')$ the relative position vector $\mathbf{r}^{(i)}(s) - \mathbf{r}^{(j)}(s')$, with magnitude $R(s, s')$, the flow $\mathbf{v}_M^{(j)\rightarrow(i)}$ is given by an

integration of rotlets singularities [8],

$$\mathbf{v}_M^{(j) \rightarrow (i)} = \int_0^L \frac{-\mathbf{m}^{(j)}(s')}{8\pi\mu} \times \frac{\mathbf{R}(s, s')}{R(s, s')^3} ds', \quad (5.40)$$

where the minus sign arises from the fact that $-\mathbf{m}^{(j)}$ is the density of moment acted from the filament on the fluid.

Using the classical hydrodynamic result

$$\mathbf{m}^{(j)} = -\xi_r \boldsymbol{\omega}^{(j)} \mathbf{t}^{(j)}, \quad (5.41)$$

which also Eq. 5.5, the integral becomes

$$\mathbf{v}_M^{(j) \rightarrow (i)} = \int_0^L \frac{\xi_r \boldsymbol{\omega}^{(j)}}{8\pi\mu} \mathbf{t}^{(j)} \times \frac{\mathbf{R}(s, s')}{R(s, s')^3} ds'. \quad (5.42)$$

Similarly, the flow velocity induced by the translational motion is given by a linear superposition of stokeslets as

$$\mathbf{v}_F^{(j) \rightarrow (i)}(s) = \int_0^L \frac{-\mathbf{f}_h^{(j)}(s')}{8\pi\mu} \cdot \left(\frac{\mathbf{I}}{R} + \frac{\mathbf{R}\mathbf{R}}{R^3} \right) ds', \quad (5.43)$$

where the force density along filament j , $\mathbf{f}_h^{(j)}$, is still to be solved for.

Following the nondimensionalisation procedures from Eq. 5.13 and 5.37, the dimensionless form of these two integrals are given by

$$\bar{\mathbf{v}}_M^{(j) \rightarrow (i)}(\bar{s}) = \frac{\epsilon_a^2}{2} \int_0^1 \bar{\boldsymbol{\omega}}(\bar{s}')^{(j)} \bar{\mathbf{t}}^{(j)}(\bar{s}') \times \frac{\bar{\mathbf{R}}(\bar{s}, \bar{s}')}{\bar{R}(\bar{s}, \bar{s}')^3} d\bar{s}', \quad (5.44a)$$

$$\bar{\mathbf{v}}_F^{(j) \rightarrow (i)}(\bar{s}) = \frac{1}{2\ln(1/\epsilon_a)} \int_0^1 \bar{\mathbf{f}}_h^{(j)} \cdot \left(\frac{\mathbf{I}}{\bar{R}} + \frac{\bar{\mathbf{R}}\bar{\mathbf{R}}}{\bar{R}^3} \right) d\bar{s}'. \quad (5.44b)$$

For notation convenience, we drop the bars below to indicate dimensionless quantities in the following derivations. Consider the integration results in previous chapter, Eq. 4.13 and 4.26, Eq. 5.44 is evaluated as

$$\mathbf{v}_M^{(j) \rightarrow (i)} = \frac{\epsilon_a^2}{\epsilon_h d^2} \boldsymbol{\omega}^{(j)}(s) \mathbf{e}_z \times \mathbf{d}, \quad (5.45a)$$

$$\mathbf{v}_F^{(j) \rightarrow (i)} = \frac{\ln(\epsilon_h d)}{\ln \epsilon_a} \mathbf{f}_h^{(j)}(s) \cdot (\mathbf{I} + \mathbf{e}_z \mathbf{e}_z). \quad (5.45b)$$

The algebraic dependence of \mathbf{v}_M on d arises from the fast $\sim 1/r^3$ spatial decay of rotlets while the logarithmic dependence in \mathbf{v}_F is a consequence of the slow $\sim 1/r$ decay of point forces in Stokes flows.

5.4 Long-wavelength bundling model

With both the elastic and hydrodynamic forces evaluated asymptotically in the limit relevant to the bundling of bacterial flagella ($\epsilon_a \ll \epsilon_h \ll 1$), we may now derive the long-wavelength bundling model.

First, we substitute Eq. 5.32 and Eq. 5.38 into Eq. 5.1, so that the force balance on filament i may now be written

$$\frac{\partial^4 \mathbf{r}^{(i)}}{\partial s^4} + \left[\mathbf{I} - \frac{1}{2} \mathbf{t}^{(i)} \mathbf{t}^{(i)} \right] \cdot \left[\frac{\partial \mathbf{r}^{(i)}}{\partial t} - \mathbf{v}^{(j) \rightarrow (i)} \right] = 0. \quad (5.46)$$

As seen in Sec. 5.2.4, the twist density is quasi-steady mechanical equilibrium, and as a consequence the local rotation rate of the filament relative to the fluid is constant, i.e. $\omega^{(i)}(s) = \omega_0^{(i)}$. Since at leading order $\mathbf{t}^{(i)}$ is \mathbf{e}_z , we have the force balance as

$$\frac{\partial^4 \mathbf{r}^{(i)}}{\partial s^4} + \left[\mathbf{I} - \frac{1}{2} \mathbf{e}_z \mathbf{e}_z \right] \cdot \left[\frac{\partial \mathbf{r}^{(i)}}{\partial t} - \mathbf{v}^{(j) \rightarrow (i)} \right] = 0. \quad (5.47)$$

Considering the description of the geometry in cartesian coordinates as in Eq. 6.10, we see that

$$\mathbf{e}_z \cdot \frac{\partial \mathbf{r}^{(i)}}{\partial t} = 0. \quad (5.48)$$

Also, considering Eqs. 5.39 and 5.45, and using the fact that the force density in Eq. 5.45b is given by Eq. 5.32, we obtain

$$\mathbf{v}^{(j) \rightarrow (i)} = \frac{\epsilon_a^2 \omega_0^{(j)}}{\epsilon_h d^2} \mathbf{e}_z \times \mathbf{d} - \frac{\ln(\epsilon_h d)}{\ln \epsilon_a} \frac{\partial^4 \mathbf{r}^{(j)}}{\partial s^4}, \quad (5.49)$$

which clearly leads to

$$\mathbf{e}_z \cdot \mathbf{v}^{(j) \rightarrow (i)} = 0. \quad (5.50)$$

Substituting Eqs. 5.48 and 5.50 into Eq. 5.47, we have

$$\frac{\partial^4 \mathbf{r}^{(i)}}{\partial s^4} + \frac{\partial \mathbf{r}^{(i)}}{\partial t} = \mathbf{v}^{(j) \rightarrow (i)}, \quad (5.51)$$

which, when using Eq. 5.49, transforms into

$$\frac{\partial \mathbf{r}^{(i)}}{\partial t} + \frac{\partial^4 \mathbf{r}^{(i)}}{\partial s^4} = \frac{\varepsilon_a^2 \omega_0^{(j)}}{\varepsilon_h d^2} \mathbf{e}_z \times \mathbf{d} - \frac{\ln(\varepsilon_h d)}{\ln \varepsilon_a} \frac{\partial^4 \mathbf{r}^{(j)}}{\partial s^4}. \quad (5.52)$$

An inspection of the terms in Eq. 5.52 reveals the presence of two dimensionless numbers. The first one, which is multiplying the bending term, is given by a ratio of logarithms

$$\frac{\ln(\varepsilon_h d)}{\ln \varepsilon_a}. \quad (5.53)$$

This term is not a true parameter since it depends on the local filament-filament distance, d . However, given the presence of two logarithms, it is expected to show only weak dependence on it, and is thus approximately given by the ratio [51]

$$\frac{\ln(L/h_0)}{\ln(L/a)}. \quad (5.54)$$

The second dimensionless number is more critical and controls the driving force in the bundling dynamics. It is the one comparing the rotational component of the flow in Eq. 5.52 to the bending (or viscous terms) which scales as ε_h . We term this dimensionless ratio the *Bundling Number*, Bu , which is therefore defined by

$$Bu = \frac{\varepsilon_a^2 \omega_0}{\varepsilon_h^2}, \quad (5.55)$$

and if different filaments have different rotation rates then clearly there will be more than one relevant bundling numbers. Alternatively, given Eq. 5.15, the bundling number can also be written as

$$Bu = \frac{\varepsilon_a^2 S p^4}{\varepsilon_h^2}. \quad (5.56)$$

As a final note, we may write the final model projected along cartesian coordinates, and obtain

$$\frac{\partial}{\partial t} \begin{bmatrix} x^{(i)} \\ y^{(i)} \end{bmatrix} + \frac{\partial^4}{\partial s^4} \begin{bmatrix} x^{(i)} \\ y^{(i)} \end{bmatrix} = \frac{\varepsilon_a^2 \omega_0^{(j)}}{\varepsilon_h^2 d^2} \begin{bmatrix} -y^{(i)} + y^{(j)} \\ x^{(i)} - x^{(j)} \end{bmatrix} - \frac{\ln(\varepsilon_h d)}{\ln \varepsilon_a} \frac{\partial^4}{\partial s^4} \begin{bmatrix} x^{(j)} \\ y^{(j)} \end{bmatrix}, \quad (5.57)$$

where $d^2 = (x^{(1)} - x^{(2)})^2 + (y^{(1)} - y^{(2)})^2$. This is the form which will be used below in the numerical solution of the problem.

5.5 Bundling and unbundling of elastic filaments

I have derived above the local partial differential equation describing the time-evolution of the filaments interacting hydrodynamically. It is given in Eq. 5.52 in a vector form and in Eq. 5.57 in cartesian coordinates. We now study numerically (with technical details summarised in §5.5.1) the dynamics predicted by the model and focus on four situations of interest: Two filaments with identical rotation rate (§5.5.2); $N > 2$ symmetric filaments (§5.5.3); An asymmetric arrangement of three filaments (§5.5.4) and the unbundling of filaments (§5.5.5).

5.5.1 Numerical procedure

In order to solve Eq. 5.52, we discretise the equation spatially using second-order central finite difference. Each filament is assumed to be clamped at its rotated end ($s = 0$) and free on the other end ($s = 1$) and thus the boundary conditions are written as

$$\mathbf{r}(s = 0, t) = \mathbf{r}_0, \quad \frac{\partial \mathbf{r}}{\partial s}(s = 0, t) = \mathbf{e}_z, \quad (5.58a)$$

$$\frac{\partial^2 \mathbf{r}}{\partial s^2}(s = 1, t) = \mathbf{0}, \quad \frac{\partial^3 \mathbf{r}}{\partial s^3}(s = 1, t) = \mathbf{0}, \quad (5.58b)$$

where \mathbf{r}_0 refers to the location of the end point of the particular filament of interest. Each filament starts initially from a straight shape given by

$$\mathbf{r}(s, t = 0) = \mathbf{r}_0 + s\mathbf{e}_z, \quad 0 \leq s \leq 1, \quad (5.59)$$

from which Eq. 5.52 is solved in time using a second-order Crank-Nicolson method. In order to prevent the interacting filaments from touching each other and overlap, I apply numerically a short-range repulsive potential of the form

$$V_r = \left(\frac{2\epsilon_a}{\epsilon_h d} \right)^q. \quad (5.60)$$

In the results shown in the following sections we choose the value $q = 4$ so that this repulsion only comes into play when $d \sim a$ and thus does not affect any of the long-ranged hydrodynamic features. I also tried $q = 6$ with no qualitative impact on the dynamics.

5.5.2 Bundling of two filaments

Let us first consider the case of two filaments with identical rotation rate, ω_0 . If we denote the projection of \mathbf{r} on the $x - y$ plane as $\tilde{\mathbf{r}} = \mathbf{r} \cdot (\mathbf{I} - \mathbf{e}_z \mathbf{e}_z)$, then by symmetry we clearly have

$$\tilde{\mathbf{r}}^{(1)}(s, t) + \tilde{\mathbf{r}}^{(2)}(s, t) = \mathbf{0}. \quad (5.61)$$

Or in components,

$$\begin{bmatrix} x^{(1)} \\ y^{(1)} \end{bmatrix} + \begin{bmatrix} x^{(2)} \\ y^{(2)} \end{bmatrix} = \mathbf{0}. \quad (5.62)$$

Substituting this symmetry property into Eq. 5.57, we obtain that each filament shape satisfies

$$\frac{\partial \tilde{\mathbf{r}}}{\partial t} + \left[1 - \frac{\ln(\varepsilon_h d)}{\ln \varepsilon_a} \right] \frac{\partial^4 \tilde{\mathbf{r}}}{\partial s^4} = \frac{2Bu}{d^2} \mathbf{e}_z \times \tilde{\mathbf{r}}, \quad (5.63)$$

written in components as

$$\frac{\partial}{\partial t} \begin{bmatrix} x \\ y \end{bmatrix} + \left[1 - \frac{\ln(\varepsilon_h d)}{\ln \varepsilon_a} \right] \frac{\partial^4}{\partial s^4} \begin{bmatrix} x \\ y \end{bmatrix} = \frac{2Bu}{d^2} \begin{bmatrix} -y \\ x \end{bmatrix}, \quad d^2 = 4(x^2 + y^2). \quad (5.64)$$

This equation was solved numerically for a wide range of values of Bu. As will be detailed below, we obtain three qualitatively different dynamics which we now illustrate by focusing on three representative values of Bu (specifically, Bu = 2, 30 and 60). The time-varying shapes of the filaments are shown as a function of time in Fig. 5.2 while in Fig. 5.3 we plot the dimensionless bending energy of each filament as a function of time. This bending energy defined for each filament, E_b , is proportional to the bending modulus, and the integration of square of curvatures,

$$E_b = \int_0^L \frac{A}{2} |\mathbf{r}_{ss}|^2 ds. \quad (5.65)$$

I define the dimensionless form, \bar{E}_b ,

$$\bar{E}_b = \int_0^1 x_{ss}^2 + y_{ss}^2 d\bar{s}, \quad (5.66)$$

with scaling

$$E_b = \frac{A}{2L} \varepsilon_h^2 \bar{E}_b. \quad (5.67)$$

In all three cases the long-time steady-state shapes are illustrated in Fig. 5.4.

For a small value, $Bu < 2$, the rotating filaments each bend toward each other until converging on steady weakly bent shapes (Fig. 5.2-5.4a). For an intermediate value, $Bu = 30$, the initial dynamics is similar but then at a critical time the filaments undergo a rapid conformation change and snap into a crossing configuration in which they remain (Fig. 5.2-5.4b). In contrast for a high value, $Bu = 60$, the filaments do not remain in a crossing configuration but instead they quickly transition to a bundled state where the filaments wrap helically around each other all along the filament after the crossing point (Fig. 5.2-5.4c)

In order to further characterise the different steady-state conformations, I plot in Fig. 5.5 the value of the long-time dimensionless bending energy of the filaments as a function of Bu . The results show two branches; the black solid line represents numerically results obtained while increasing the values of Bu while the red dashed line captures the computational results obtained by starting with a high value and decreasing Bu . Interestingly, we see that the two transitions (bent \leftrightarrow crossing and crossing \leftrightarrow bundle) both show hysteresis loops. When Bu increases from zero, the transitions occur approximately at $Bu \approx 2$ and 40 , while in the decreasing case, the critical values are $Bu \approx 10$ and 1.5 .

5.5.3 N symmetric filaments

After focusing on two filaments, we can consider the more general case of N filaments distributed symmetrically along a circular base from which they are all rotated with equal angular velocity. This situation is sketched in Fig. 5.6.

The in-place location of filament $\#n$ is written as

$$\mathbf{r}^{(n)}(s) = [h_0x^{(n)}(s), h_0y^{(n)}(s)], \quad (5.68)$$

which maybe be related to the displacements $[\zeta^{(n)}, \eta^{(n)}]$ as

$$x^{(n)} = \frac{\sin(n-1)\theta}{2} + \zeta^{(n)}, \quad y^{(n)} = -\frac{\cos(n-1)\theta}{2} + \eta^{(n)}. \quad (5.69)$$

In order to simplify the system we define the complex number

$$\mathbf{z}^{(n)} = x^{(n)} + iy^{(n)}, \quad (5.70)$$

which, due to the expected symmetry of the N -filament configuration, satisfies

$$\mathbf{z}^{(n)} = \mathbf{ze}^{i(n-1)\theta}. \quad (5.71)$$

To derive the dynamics equation, we first extend Eq. 5.52 to the case of N arbitrary filaments by adding up the flows arising from hydrodynamic interactions. Using dimensional quantities, the position of the n th filament satisfies

$$\frac{\partial \mathbf{r}^{(n)}}{\partial t} + \frac{A}{\xi_{\perp}} \frac{\partial^4 \mathbf{r}^{(n)}}{\partial s^4} = a^2 \omega_0 \sum_{j \neq n}^N \frac{\mathbf{e}_z \times (\mathbf{r}^{(n)} - \mathbf{r}^{(j)})}{|\mathbf{r}^{(n)} - \mathbf{r}^{(j)}|^2} - \frac{A}{\xi_{\perp}} \sum_{j \neq n}^N \frac{\ln(|\mathbf{r}^{(n)} - \mathbf{r}^{(j)}|/L)}{\ln(a/L)} \frac{\partial^4 \mathbf{r}^{(j)}}{\partial s^4}. \quad (5.72)$$

The two summations in Eq. 5.72 maybe be expressed explicitly by exploiting symmetries. Focusing on the filament with $n = 1$, for which we write $\mathbf{r}^{(1)} \equiv \mathbf{r}$, we observe that

$$\sum_{l=j, N+2-j} \frac{\mathbf{z} - \mathbf{z}^{(l)}}{|\mathbf{z} - \mathbf{z}^{(l)}|^2} = \frac{\mathbf{z} \left[2 - e^{i(j-1)\theta} - e^{i(N+1-j)\theta} \right]}{|\mathbf{z}|^2 \left[(1 - \cos(j-1)\theta)^2 + \sin^2(j-1)\theta \right]} = \frac{\mathbf{z}}{|\mathbf{z}|^2}, \quad (5.73)$$

which is independent of j . As a result we have a first summation given by

$$\sum_{j=2}^N \frac{\mathbf{e}_z \times (\mathbf{r} - \mathbf{r}^{(j)})}{|\mathbf{r} - \mathbf{r}^{(j)}|^2} = (N-1) \frac{\mathbf{e}_z \times \mathbf{r}}{2|\mathbf{r}|^2}. \quad (5.74)$$

Similarly for the second summation we have

$$\sum_{l=j, N+2-j} \ln |\mathbf{z} - \mathbf{z}^{(l)}| \frac{\partial^4 \mathbf{z}^{(l)}}{\partial s^4} = 2 \cos(j-1)\theta \left[\ln |\mathbf{z}| + \ln \sqrt{2 - 2 \cos(j-1)\theta} \right] \frac{\partial^4 \mathbf{z}}{\partial s^4}, \quad (5.75)$$

so that

$$\begin{aligned} \sum_{j=2}^N \ln |\mathbf{r} - \mathbf{r}^{(j)}| \frac{\partial^4 \mathbf{r}}{\partial s^4} &= \frac{\partial^4 \mathbf{r}}{\partial s^4} \sum_{j=2}^N \cos(j-1)\theta \left[\ln |\mathbf{r}| + \ln \sqrt{2 - 2 \cos(j-1)\theta} \right] \\ &= (\alpha_N \ln |\mathbf{r}| + \beta_N) \frac{\partial^4 \mathbf{r}}{\partial s^4}, \end{aligned} \quad (5.76)$$

where the coefficients α_N and β_N are given by

$$\alpha_N = \sum_{j=2}^N \cos(j-1)\theta, \quad \beta_N = \sum_{j=2}^N \cos(j-1)\theta \ln \sqrt{2 - 2 \cos(j-1)\theta}. \quad (5.77)$$

Substituting Eq. 5.74 and 5.76 into Eq. 5.72, we obtained the simplified equation in the case of N symmetric filaments

$$\frac{\partial \mathbf{r}}{\partial t} + \frac{A}{\xi_{\perp}} \frac{\partial^4 \mathbf{r}}{\partial s^4} = a^2 \omega_0 \frac{(N-1) \mathbf{e}_z \times \mathbf{r}^{(1)}}{2|\mathbf{r}|^2} - \frac{A}{\xi_{\perp} \ln(a/L)} (\alpha_N \ln |\mathbf{r}/L| + \beta_N) \frac{\partial^4 \mathbf{r}}{\partial s^4}, \quad (5.78)$$

which may also be written using dimensionless variables as

$$\frac{\partial \bar{\mathbf{r}}}{\partial \bar{t}} + \left[1 + \frac{(\alpha_N \ln |\bar{\mathbf{r}}| + \beta_N)}{\ln \varepsilon_a} \right] \frac{\partial^4 \bar{\mathbf{r}}}{\partial \bar{s}^4} = \frac{\varepsilon_a^2 \bar{\omega}_0 (N-1)}{2} \frac{\mathbf{e}_z \times \bar{\mathbf{r}}}{|\bar{\mathbf{r}}|^2}, \quad (5.79)$$

where a N -filament Bundling number is naturally defined as

$$Bu_N = \frac{\varepsilon_a^2 \bar{\omega}_0 (N-1)}{\varepsilon_h^2}. \quad (5.80)$$

Note that the case $N = 2$ which was considered earlier in the paper may be recovered identically under this framework. Indeed we have in this case

$$\theta = \frac{\pi}{2}, \quad \alpha_2 = -1, \quad \beta_2 = -\ln 2, \quad (5.81)$$

leading to

$$\frac{\partial \bar{\mathbf{r}}}{\partial \bar{t}} + \left[1 - \frac{\ln(2|\bar{\mathbf{r}}|)}{\ln \varepsilon_a} \right] \frac{\partial^4 \bar{\mathbf{r}}}{\partial \bar{s}^4} = \frac{\varepsilon_a^2 \bar{\omega}_0}{2} \frac{\mathbf{e}_z \times \bar{\mathbf{r}}}{|\bar{\mathbf{r}}|^2}. \quad (5.82)$$

Since $2\bar{\mathbf{r}} = \varepsilon_h \mathbf{d}$, the equation is identical to Eq. 5.64.

The final equation, Eq. 5.79, allows thus to exploit symmetries in order to significantly simplify the complicated multi-filaments problem. Qualitatively, we obtain the same three regimes (bent, crossed, bundled) as with two filaments. Numerical results showing the time dependence of the shapes are illustrated in Figs. 5.7 for $N = 3$ filaments (top) and $N = 6$ (bottom) in the case of a large Bundling number, $Bu_N = 60$, leading to crossing at intermediate times and a final bundled state.

5.5.4 Asymmetric filaments

In the situation where the distribution of filaments is not symmetric, it is possible to apply our model by solving the coupled system of equations in Eq. 5.72. As an illustration, we show in Fig. 5.8 the dynamics in the case of $N = 3$ filaments clamped and rotated with a 3:1 separation distance. The initial position of the filaments is given in a dimensional form by

$$\mathbf{r}_0^{(1)} = [0, -0.05L], \quad \mathbf{r}_0^{(2)} = [0, 0.25L], \quad \mathbf{r}_0^{(3)} = [0, 0.05L]. \quad (5.83)$$

For $Bu = 30$ (ε_h is chosen as the largest ratio between filament-filament distance and L , which is 0.1 in this case), the two filaments which are the closest to each other bundle first together, and then bundle as a pair with the third filament located further away.

5.5.5 Unbundling

In the biological world, swimming bacteria change their swimming direction by reversing the rotation direction of at least one its rotary motors, leading the bundle of helical flagella coming apart [133]. This process may be addressed with this simple model. We consider N identically-rotating filaments in the steady bundled state and may then switch the rotation direction of one of the filaments (i.e. switching its Bundling number to a negative value). This is illustrated in Fig. 5.9 for $N = 2$ filaments (top) and $N = 3$ (bottom). In both cases, the unbundling process is fast compared to the initial bundling dynamics shown Figs. 5.2 and 5.7 and it results in a separation between the negatively-rotating filament and the other ones. With more filaments, different numbers of motors may switch directions, leading to different unbundled states. This is illustrated in Fig. 5.10 in the case of $N = 6$ filaments where we show the long-time conformation of the rotating shapes as a function of the number of negatively-rotating filaments and their location (indicated by a red dot at their base).

5.6 Crossing instability

One of the main results predicted from our model is the occurrence of instabilities in the conformation of the filaments. This is best seen by inspecting Fig. 5.5. The dimensionless bending energy of the steady-state shape of each filament clearly indicates that sharp transitions occur from weakly bent to crossing ($Bu \approx 2$) and from crossing to bundling ($Bu \approx 40$). In addition, each transition is associated with a strong hysteresis loop.

Both crossing and bundling instabilities share the same physical origin. Hydrodynamic interactions bend the filaments and are resisted by elastic forces. At a critical rotation rate, the bending resistance is unable to balance the hydrodynamic stresses, and the filament transition to a new conformation.

From a kinematic standpoint, if two nearly-straight filaments cross, their crossing is expected to take place at either one point or along many points; indeed if two filaments happen to cross at one point, and then are made to cross at a second location along their length, then the remaining portion of the filaments is expected to remain in close continuous contact. In summary, it is expected that two crossings implies in fact many crossings.

Intuitively, I propose therefore that the fundamental instability to understand is the first, crossing instability. In this section, by focusing on the case of two filaments, I present a theoretical approach, together with a simple two-dimensional model, to show how to predict that instability.

5.6.1 Small Bu analysis and analytical ansatz

We start by solving the problem for the steady-state shape of the filaments in the small-Bu limit. The steady state of Eq. 5.64 satisfies the equation

$$\left[1 - \frac{\ln(\varepsilon_h d)}{\ln \varepsilon_a}\right] \frac{\partial^4}{\partial s^4} \begin{bmatrix} x \\ y \end{bmatrix} = \frac{2\text{Bu}}{d^2} \begin{bmatrix} -y \\ x \end{bmatrix}. \quad (5.84)$$

Based on the symmetries in the geometry, we expect x to be odd in Bu while y is expected to be even. In the limit of small values of Bu we thus look to solve Eq. 5.84 as a regular series expansion

$$x = \text{Bu}x_1 + \text{Bu}^3x_3 + \dots, \quad y = -\frac{1}{2} + \text{Bu}^2y_2 + \dots, \quad (5.85)$$

and we aim to solve for the leading order deflections (x_1, y_2) . In order to proceed with the solution, we also need to choose values for the small dimensionless parameters ε_a and ε_h . Given the numbers relevant to the bundling of bacterial flagella discussed in Sec. 5.1.1, we choose the relevant values $\varepsilon_a = 0.001$ and $\varepsilon_h = 0.01$.

With these assumptions, the solution of Eq. 5.84 at $O(\text{Bu})$ is

$$\frac{\partial^4 x_1}{\partial s^4} = \frac{3}{2}. \quad (5.86)$$

With the boundary conditions given in Eq. 5.58, we obtain the solution as

$$x_1 = \frac{s^4}{16} - \frac{s^3}{4} + \frac{3s^2}{8}. \quad (5.87)$$

At next order, $O(\text{Bu}^2)$, we have to solve

$$\frac{\partial^4 y_2}{\partial s^4} = 3x_1, \quad (5.88)$$

whole solution satisfying the boundary conditions in Eq. 5.58 is

$$y_2 = \frac{s^8}{8960} - \frac{s^7}{1120} + \frac{s^6}{320} - \frac{3s^3}{80} + \frac{13s^2}{160}. \quad (5.89)$$

Let us compare the numerical solution to the asymptotic solution in Fig. 5.11a. For find that for $\text{Bu} = 1$, the agreement with between the two is very good; however for $\text{Bu} = 2$ (close to the instability point), the difference between the computational solution and the theoretical one is more important.

In order to build a more accurate analytical model for the deflection of the filaments, we need to correct the asymptotic solution so it remains valid up to the instability point. To do so, we examine the shape of the filaments as obtained numerically for $Bu = 1$ and $Bu = 2$ and plot the rescaled distance between the filaments in Fig. 5.11b as a function of the arclength scaled by the arclength where the minimum distance occurs, s_c . We linearly map d to $1 - \frac{d-1}{d_{\min}-1}$, so that the minimum points both reaches zero. We see that, up to a rescaling, the shapes at $Bu = 1$ and $Bu = 2$ are identical and the only difference is how their magnitude scale with the change in Bu .

To construct a better analytical model, we then proceed by choosing a steady reference state $[Bu_o, x_o(s), y_o(s)]$ where the asymptotic solution provides a good estimate (we choose $Bu_o = 1$). I denote by $[s_{oc}, x_{oc}, y_{oc}]$ the critical point where the distance between the filaments, d , reaches its minimum value. We then numerically track this same critical point as we increase the value of Bu , which we denote $[s_c(Bu), x_c(Bu), y_c(Bu)]$. From this, and given the similarly of the shapes seen in Fig. 5.11b, we can construct an analytical steady-state ansatz $[Bu, x(Bu; s), y(Bu; s)]$ by simply scaling in x , y and s the reference analytical solution as

$$x(Bu; s) = \frac{x_c}{x_{oc}} x_o \left(Bu_o; \frac{s_{oc}}{s_c} s \right) \quad (5.90a)$$

$$y(Bu; s) = -\frac{1}{2} + \frac{y_c + \frac{1}{2}}{y_{oc} + \frac{1}{2}} \left[y_o \left(Bu_o; \frac{s_{oc}}{s_c} s \right) + 1/2 \right]. \quad (5.90b)$$

I show in Fig. 5.12 a comparison for each component of the shapes $x(s)$ (Fig. 5.12a) and $y(s)$ (Fig. 5.12b) between the computations (solid lines) and the analytical ansatz (dashed lines). We see that the ansatz, obtained analytically for $Bu = 1$, is able to fully capture the shape obtained numerically at $Bu = 2$.

We may then use this analytical ansatz as an accurate base state, $[x_b(Bu; s), y_b(Bu; s)]$, around which we may carry out a linear stability calculation. Assuming small deviations around the base state and exponential growth, we decompose the general shape $[x(s, t), y(s, t)]$ of the filament as

$$x(s, t) = x_b(Bu; s) + \hat{x}(s)e^{\sigma t}, \quad y(s, t) = y_b(Bu; s) + \hat{y}(s)e^{\sigma t}, \quad (5.91)$$

and substitute into Eq. 5.84, leading to the linear system,

$$\sigma \begin{bmatrix} \hat{x} \\ \hat{y} \end{bmatrix} + \left[\frac{2}{3} - \frac{\ln 2 \sqrt{x_b^2 + y_b^2}}{\ln \varepsilon_a} \right] \begin{bmatrix} \hat{x} \\ \hat{y} \end{bmatrix}_{4s} = \mathbf{A} \begin{bmatrix} \hat{x} \\ \hat{y} \end{bmatrix}, \quad (5.92)$$

where the matrix \mathbf{A} is given by

$$\mathbf{A} = \begin{bmatrix} \frac{x_b(x_b)_{4s}}{(\ln \varepsilon_a)(x_b^2 + y_b^2)} + \frac{\text{Bu}x_b y_b}{(x_b^2 + y_b^2)^2} & \frac{y_b(x_b)_{4s}}{(\ln \varepsilon_a)(x_b^2 + y_b^2)} + \frac{\text{Bu}(y_b^2 - x_b^2)}{2(x_b^2 + y_b^2)^2} \\ \frac{x_b(y_b)_{4s}}{(\ln \varepsilon_a)(x_b^2 + y_b^2)} + \frac{\text{Bu}(y_b^2 - x_b^2)}{2(x_b^2 + y_b^2)^2} & \frac{y_b(y_b)_{4s}}{(\ln \varepsilon_a)(x_b^2 + y_b^2)} - \frac{\text{Bu}x_b y_b}{(x_b^2 + y_b^2)^2} \end{bmatrix}. \quad (5.93)$$

We use finite differences

in order to solve numerically the eigenvalue problem in Eq. 5.92. We plot in Fig. 5.13 the eigenvalue with the largest real part as a function of the Bundling number. The system is seen to become linearly unstable slightly above $\text{Bu} = 2.5$, a value close to the computational result of $\text{Bu} \approx 2.2$ for the crossing instability.

5.6.2 Two-dimensional model

The analytical asymptotic solution with rescaling of its amplitude allows to capture the shape instability at a critical value of the Bundling number, and thus the transition to the ‘crossing’ configuration. In order to understand intuitively the physics behind this instability, we consider a simple toy problem displaying the same instability.

Instead of a continuous filament, consider two parallel rigid cylinders which are linked elastically to a reference position. The cylinders are assumed to rotate at a constant rate in the fluid and thus to interact hydrodynamically. This setup is illustrated schematically in Fig. 5.14 with the same axis notation as for the two-filament case.

Assuming that one of the cylinders is located at (x, y) in Cartesian coordinates. When $t = 0$, the position is $(0, -1/2)$. According to symmetry, the other cylinder is located at $(-x, -y)$. We assume a elastic force simply proportional to the displacement of the cylinders away from their reference configuration $(x, y + 1/2)$, the force balance between local viscous drag, elastic restoring force and hydrodynamic interactions leads to the dimensionless equation for the position (x, y)

$$\frac{\partial}{\partial t} \begin{bmatrix} x \\ y \end{bmatrix} + \begin{bmatrix} x \\ y + \frac{1}{2} \end{bmatrix} = \frac{\mathbf{B}}{d^2} \begin{bmatrix} -y \\ x \end{bmatrix}, \quad (5.94)$$

where \mathbf{B} is a dimensionless coefficient similar to the bundling number which includes geometry and elasticity, and $d = 2\sqrt{x^2 + y^2}$ is the distance between cylinders.

For which values of \mathbf{B} can a steady state be found? At steady state, the hydrodynamic force has to balance the elastic resistance. If both cylinders are located at a distance d from

each other, the magnitude of the hydrodynamic force is given by $B/2d$ while the elastic restoring force is given by the distance to the reference point. Since the hydrodynamic force acts at right angle to the vector joining the cylinders, each cylinder is constrained mechanically to remain on a circle of diameter $1/2$ (see Fig. 5.14b). the distance between the cylinder and its reference configuration may then be obtained using the Pythagorean Theorem as $\sqrt{1/4 - d^2/4} = \sqrt{1 - d^2}/2$. Force balance between elasticity and hydrodynamics requires therefore that

$$B = d\sqrt{1 - d^2}. \quad (5.95)$$

The right hand-side of this equation is bounded from above by $1/2$ and thus there exists a steady state only for $B \leq 1/2$, which corresponds to a finite critical distance between the cylinders of $d = 1/\sqrt{2}$. This simple elasto-hydrodynamic model allows therefore to reproduce the same physics of a continuous elastic deformation until a critical finite distance and a bifurcation.

5.6.3 Single model

Inspired by the success of the simple cylindrical model, we adapt a similar idea to the case of two elastic filaments by focusing on the elastic deformation at their tips. Using the asymptotic results in Eqs. 5.86 - 5.89, we see that for small values of Bu the components at tip ($s = 1$) of the elastic forces and the displacements are given by

$$x_{4s}(s = 1) = \frac{3}{2}Bu, \quad x(s = 1) = \frac{3}{16}Bu, \quad (5.96)$$

$$y_{4s}(s = 1) = \frac{9}{16}Bu^2, \quad y = -\frac{1}{2} + \frac{413}{8960}Bu^2. \quad (5.97)$$

Using these results, we can then infer a linear force-displacement relationship valid at the tip at small Bu

$$x_{4s} = 8x, \quad y_{4s} = \frac{5040}{413} \left(y + \frac{1}{2} \right). \quad (5.98)$$

Using Eq. 5.98 to replace the continuous elastic forcing by one proportional to the displacement of the tip away from its reference point, we may replace Eq. 5.84 by an algebraic equation as

$$\left[1 - \frac{\ln(\varepsilon_h d)}{\ln \varepsilon_a} \right] \begin{bmatrix} 8x \\ \frac{5040}{413} \left(y + \frac{1}{2} \right) \end{bmatrix} = \frac{2Bu}{d^2} \begin{bmatrix} -y \\ x \end{bmatrix}. \quad (5.99)$$

Since the two vectors in Eq. 5.99 are proportional to each other, their cross product is zero leading to the identity

$$x^2 = -\frac{630}{413}y \left(y + \frac{1}{2} \right). \quad (5.100)$$

As a consequence we have

$$\frac{d^2}{4} = x^2 + y^2 = -\frac{217}{413}y^2 - \frac{315}{413}y. \quad (5.101)$$

We then use the first row of Eq. 5.99 to obtain Bu as an explicit function of y

$$Bu = - \left(1 - \frac{\ln \epsilon_h d}{\ln \epsilon_a} \right) \frac{4xd^2}{y}, \quad (5.102)$$

with x given by Eq. 5.100 and d by Eq. 5.101.

The value of the right-hand side of this equation may be computed for all y in the interval $-0.5 \leq y < 0$, with results shown in Fig. 5.15.

We see that Bu reaches its maximum value around 2 at position $(0.31, -0.23)$, with distance d around 0.76. When Bu is larger than this critical value, no steady-state solution exists, thus the a shape instability. This analytical estimate agrees very well with the critical value of Bu found numerically and allows therefore to successfully capture the physics of it.

5.7 Discussion

In this chapter, I have presented a long-wavelength elastic filaments model of flagellar bundling. By deriving the leading-order coupling flow that represents the hydrodynamic interactions between two nearby elastic filaments with separation h lying in the regime $a \ll h \ll L$, I have obtained a partial differential equation with a single controlling dimensionless number, bundling number Bu . Based on this model, I have solved the bundling and unbundling dynamics of two or more filaments. The steady-state filaments demonstrate three types of configurations, nearly straight, crossing and bundle, depending on the range of Bu , and instabilities occur with the transitions. I analytically tackled the instability occurs in the first transition by building a small Bu ansatz and a simplified 2d model. The critical values of Bu given by two methods are $Bu = 2.5$ and 2 respectively, which is in good agreement with the numerically computed $Bu = 2.2$.

Beyond the far field $h \gg a$ where the bundling model has been derived, an untouched question is the case when filaments almost touch each other. In numerical studies, I have applied repulsion forcing to keep the distance between filaments in the same order of

magnitude of radius a . We can check the validity by considering the lubrication limit where $h \ll a$. At lubrication limit, the hydrodynamic force is scaled as $O(a^{3/2}h^{-1/2})$, while in our calculation the far-field result is $O(a^2/h)$. When the distance $h \sim O(a)$, both forces are $O(a)$. However, when the filaments approach further and reach the lubrication limit, hydrodynamic force should be replaced by a much smaller force at lubrication regime, and a more sophisticated model would be required to untangle the matching of lubrication and far-field solutions.

The framework we developed to calculate the hydrodynamic interaction term is very general and can be extended to any particular situations where two or more nearby slender filaments interacting through fluids. I would like to include the helical feature of filaments to improve our bundling model in the future. Beyond that we also expect to implement applications in other problems of similar nature such as cilia arrays and cytoskeletal mechanics.

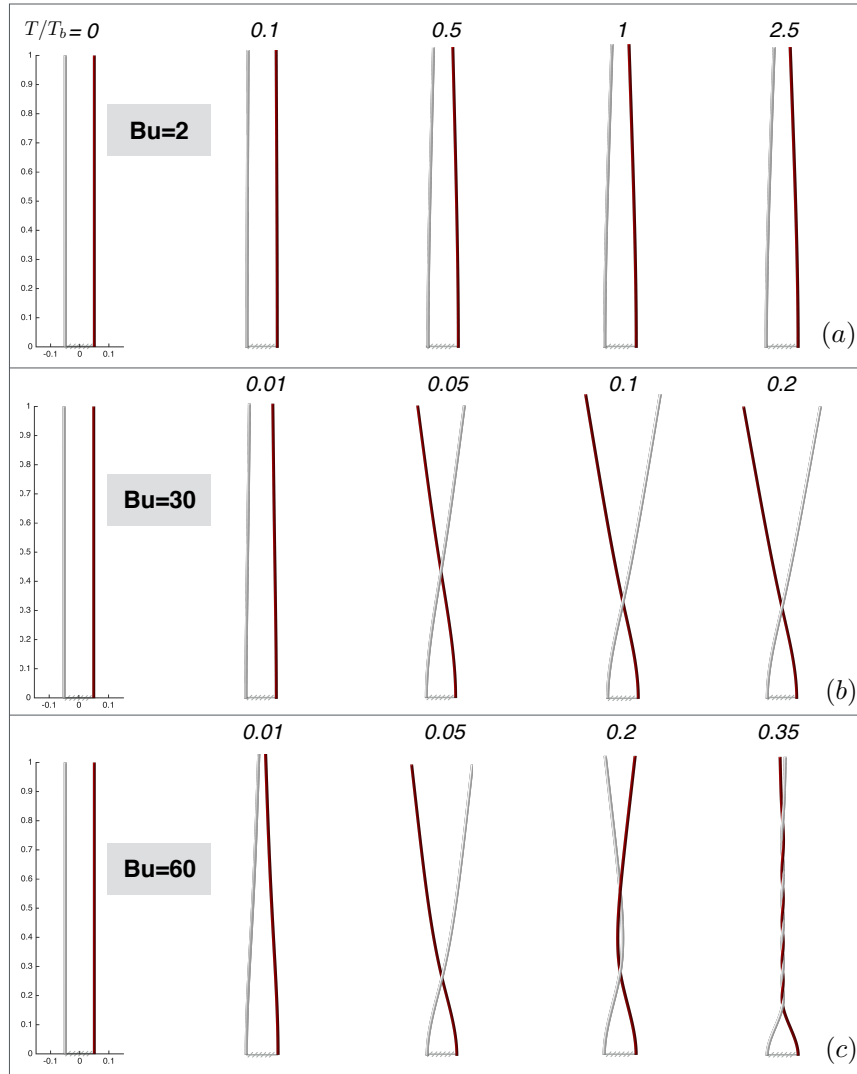


Fig. 5.2 Bundling of two elastic filaments as a function of time for three representative values of B_u ; (a): $B_u = 2$, with a weakly bent final configuration; (b): $B_u = 30$, with a final crossing configuration; (c): $B_u = 60$, with a final bundled state. The bending energy corresponding to these shapes is plotted in Fig. 5.3.

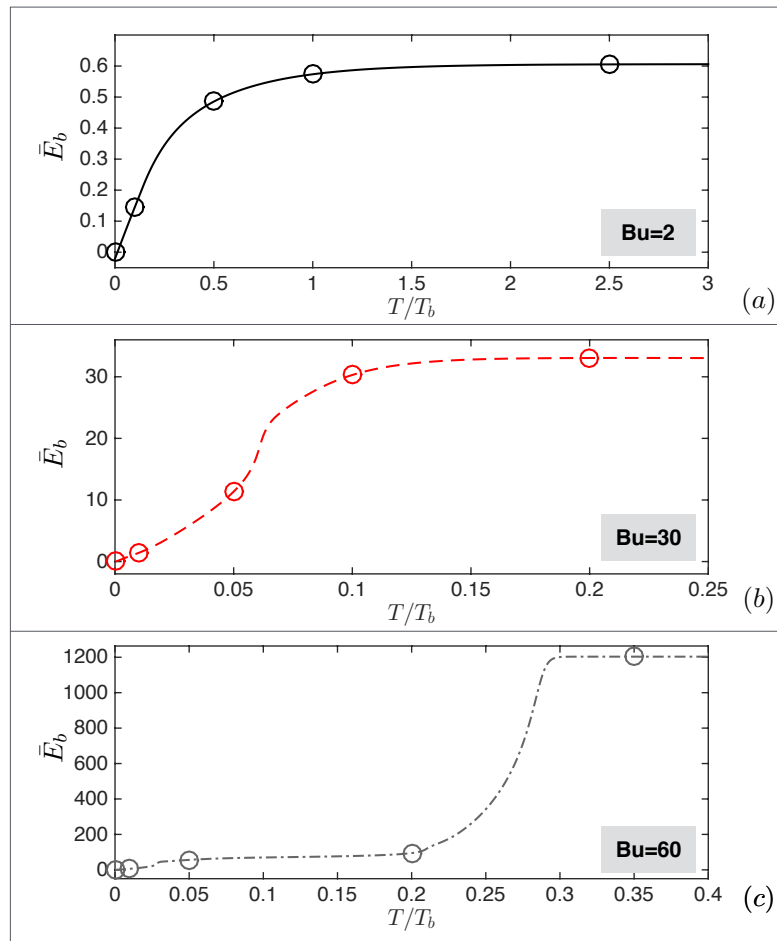


Fig. 5.3 Dimensionless filament bending energy for each filament, \bar{E}_b , as a function of time for the dynamics illustrated in Fig. 5.2 with specific times shown in circles: (a): $Bu = 2$; (b): $Bu = 30$; (c) $Bu = 60$.

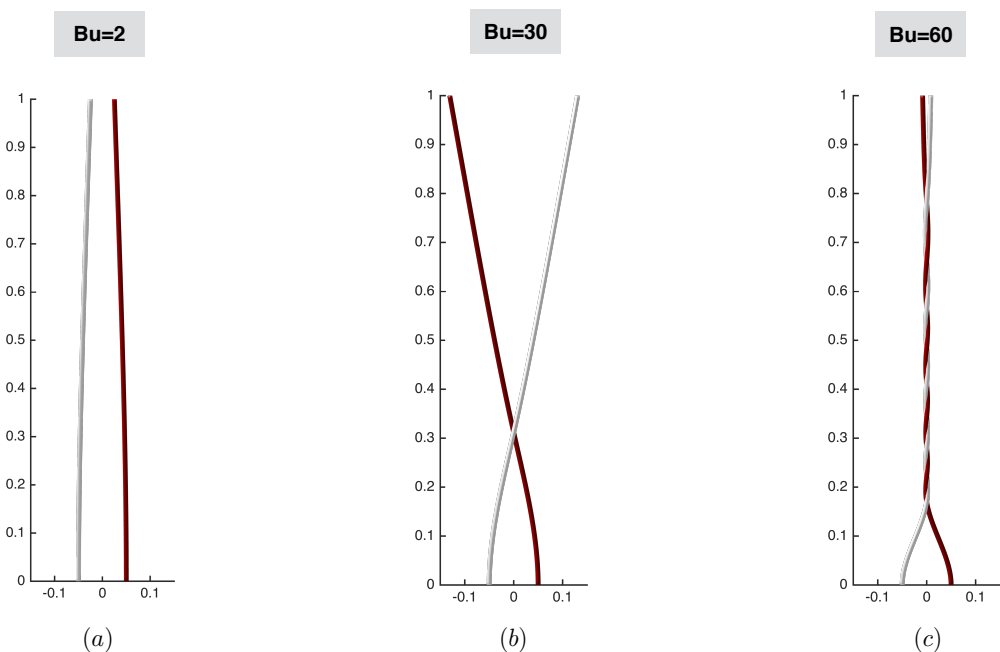


Fig. 5.4 Steady-state filament shapes for $Bu = 2, 30$ and 60 obtained for the dynamics shown in Figs. 5.2-5.3 in the long-time limit. The three possible final states are: (a): weakly bent; (b): crossing; (c): bundled.

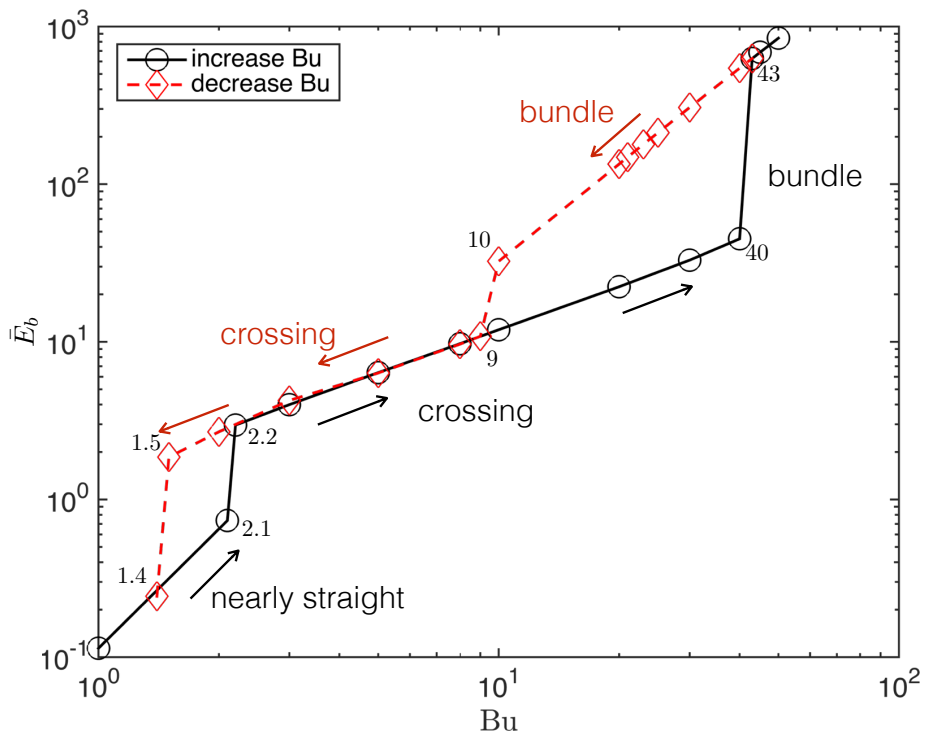


Fig. 5.5 Plot of dimensionless bending energy for each filament with respect to Bu . Black solid line represents the states marched from low Bu , while red dash line represents the states marched from high Bu . Two strong hysteresis exist in the considered range. The critical values of transitions for increasing branch is $Bu = 2$ and 40 , while for decreasing branch is $Bu = 10$ and 1.5 .

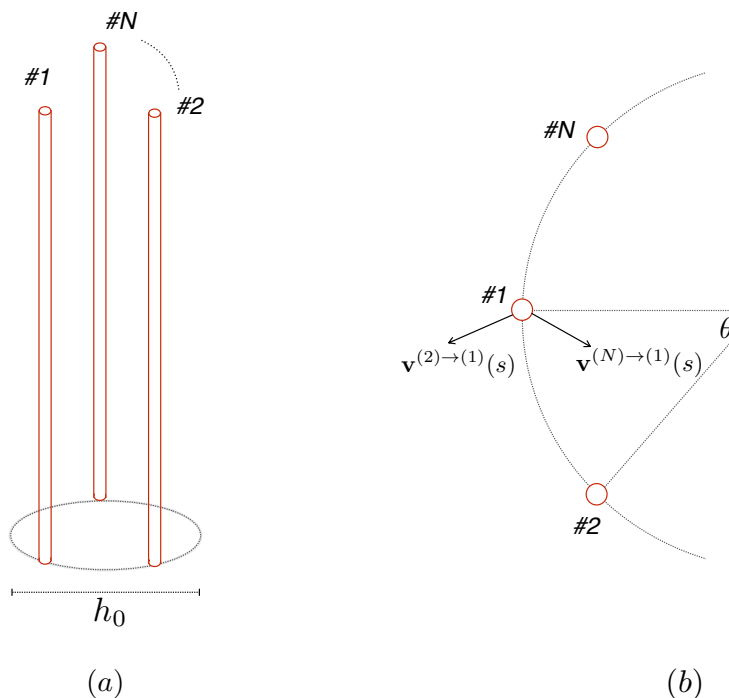


Fig. 5.6 (a) Configuration of N filaments symmetrically distributed along a circle of diameter h_0 ; (b): Top view of the N filament configuration; $\mathbf{v}^{(j)\rightarrow(i)}$ denotes the velocity generated by j th filament near the i th one while $\theta = 2\pi/N$. By exploiting the symmetries of the setup, the net flow generated by j th ($j = 2, 3 \dots N$) and $(N + 2 - j)$ th filaments is independent of j .

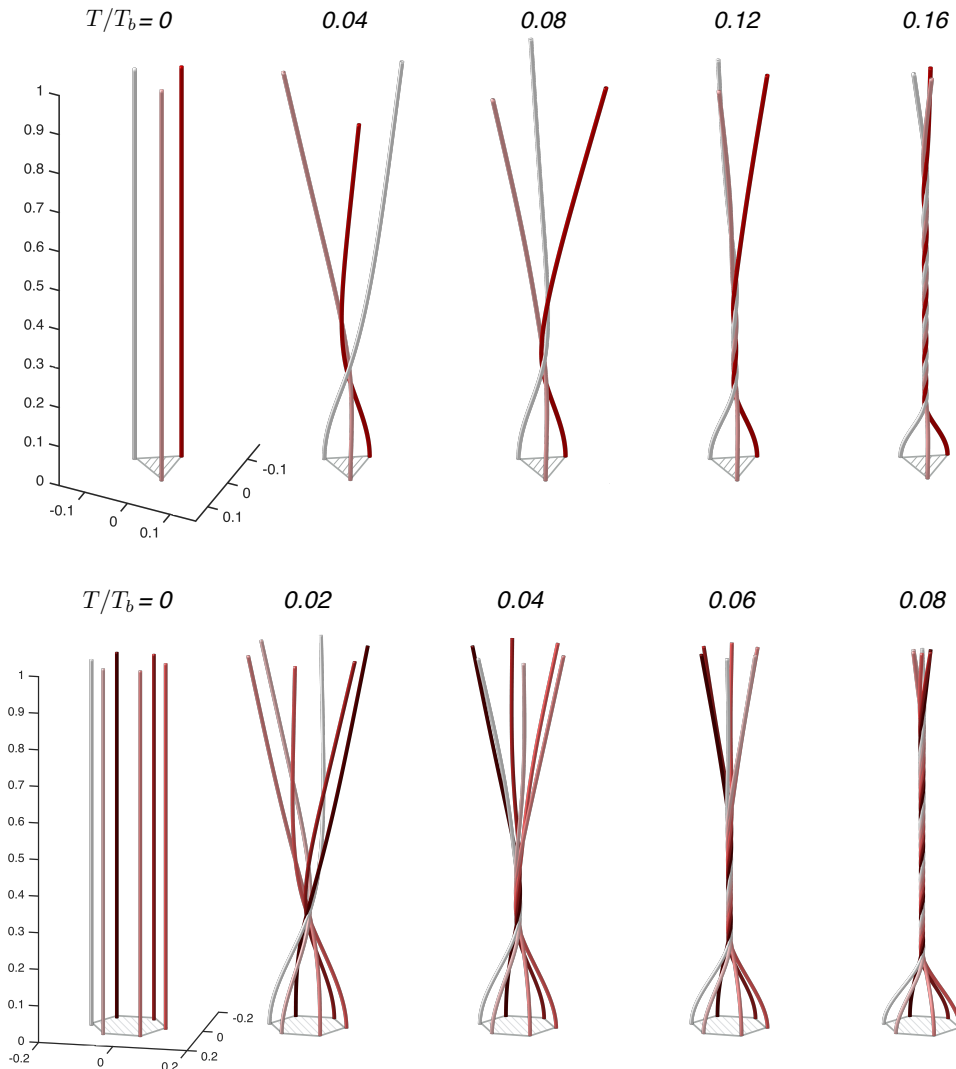


Fig. 5.7 Time dynamics of a symmetric arrangement of $N = 3$ filaments (top) and $N = 6$ (bottom) for $Bu = 60$ showing crossing at intermediate times followed by a transition to a bundled state at long times.

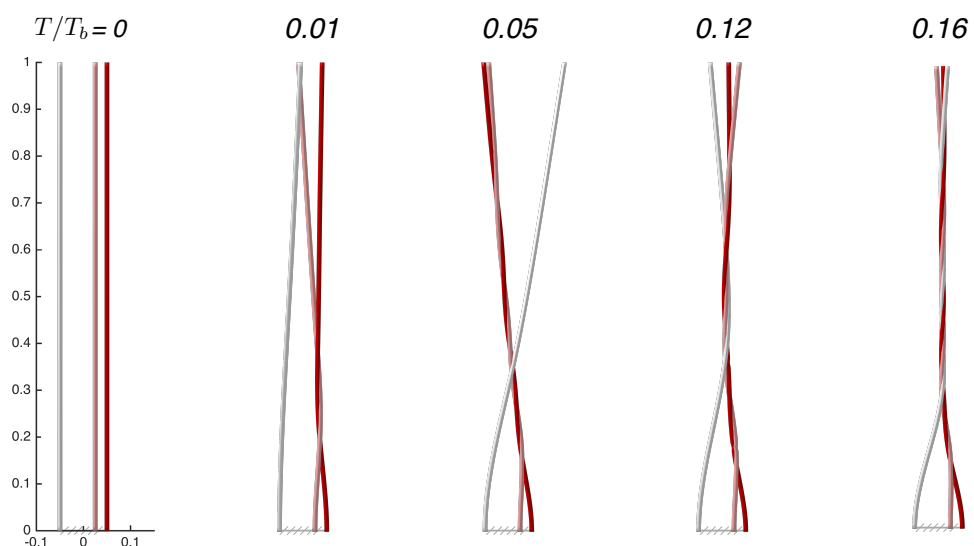


Fig. 5.8 Bundling of three filaments clamped and rotated with a 3:1 ratio in their relative separation for $Bu = 30$.

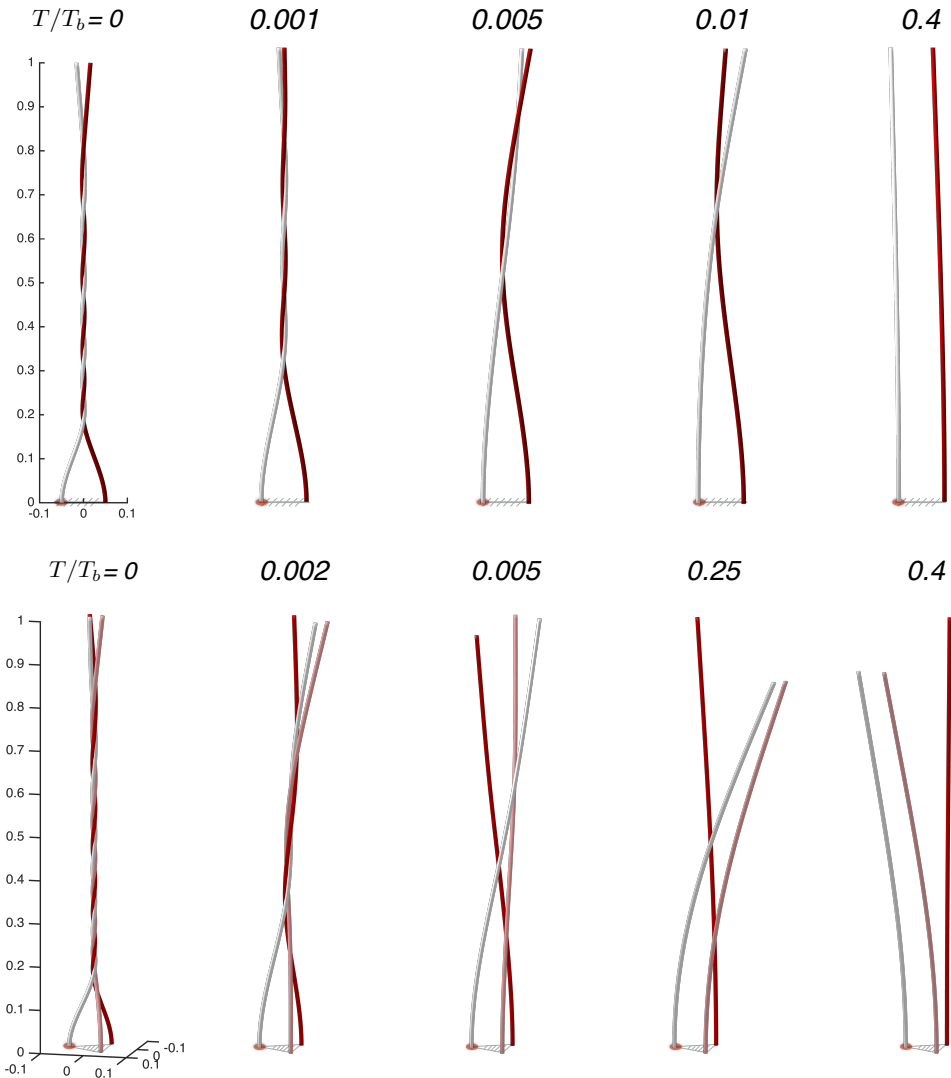


Fig. 5.9 Hydrodynamic unbundling of rotating filaments. Top: cases of two bundled filaments where at $t = 0$ the Bundling number of the filament on the left (with red dot at bottom) is switched to $Bu = -50$, while for the other is maintained at $Bu = 50$. Bottom: three filaments where the filament with the red dot at bottom is switched to $Bu = -40$, while for the other two are maintained at $Bu = 40$.

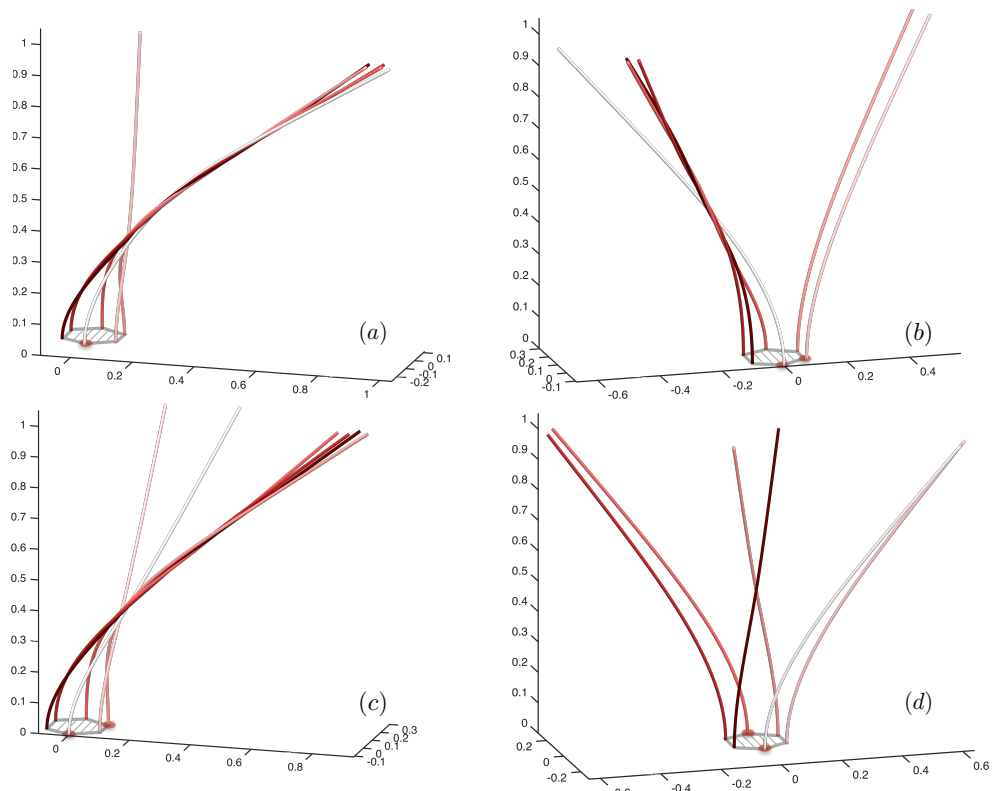


Fig. 5.10 Steady unbundled states for $N = 6$ filaments. Filaments with a red dot at their base have negative rotation and $Bu = -40$ while all other ones are maintained at $Bu = 40$.

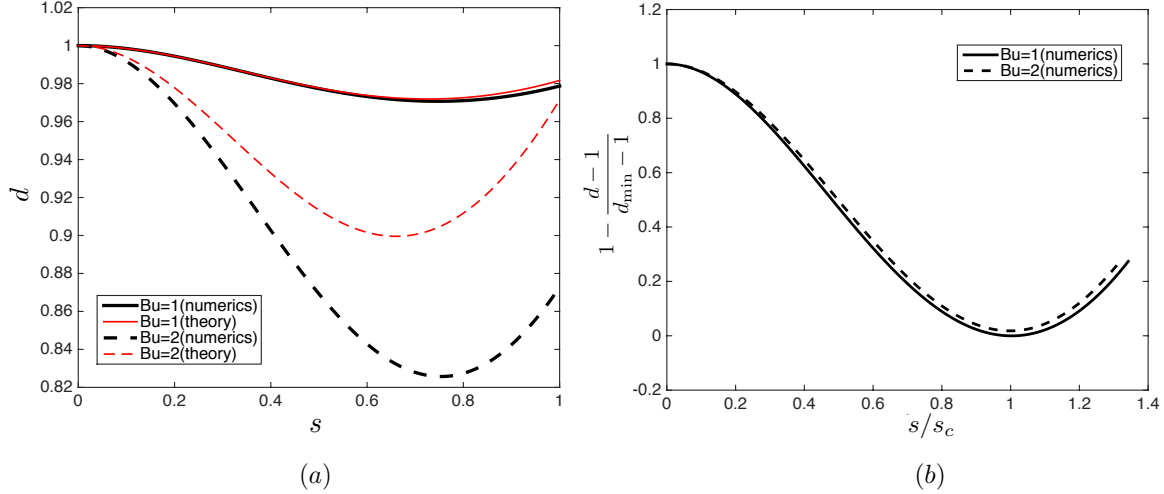


Fig. 5.11 (a) Comparison between the asymptotic solution for the deflection of the filaments (thin red lines) with the numerical solution (thick black lines) for $Bu = 1$ (solid) and $Bu = 2$ (dashed); (b) A closer look at the numerical solutions for for $Bu = 1$ (solid) and $Bu = 2$ (dashed) indicated that up to a re-scaling they have the same shape. We denote s_c the critical value where the distance between filaments reaches its minimum.

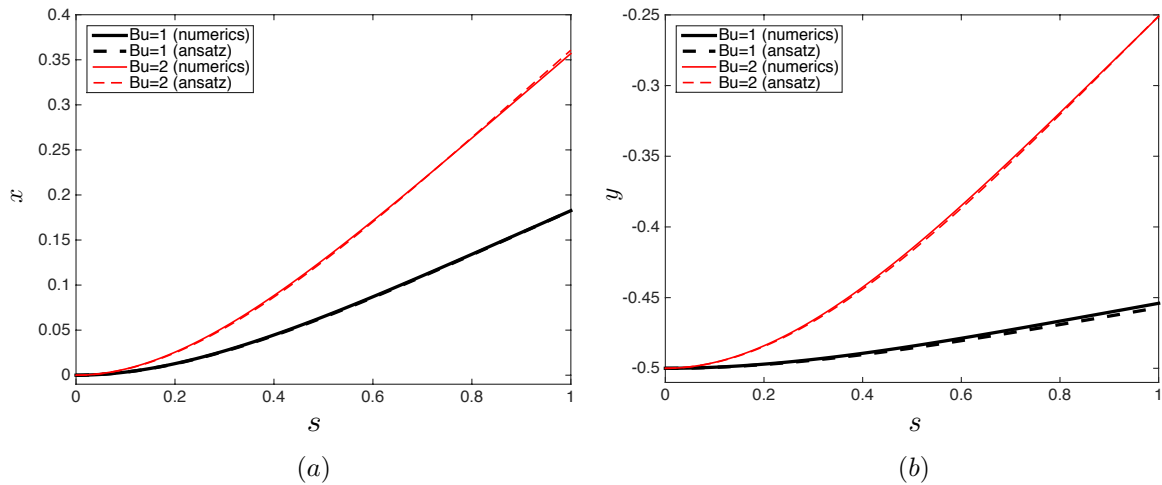


Fig. 5.12 Comparison between the numerical steady shapes (solid lines) and the shape predicted by the analytical ansatz (dashed line): (a): $x(s)$; (b): $y(s)$. The shapes are compared for $Bu = 1$ (thick black lines) and $Bu = 2$ (thin red lines).

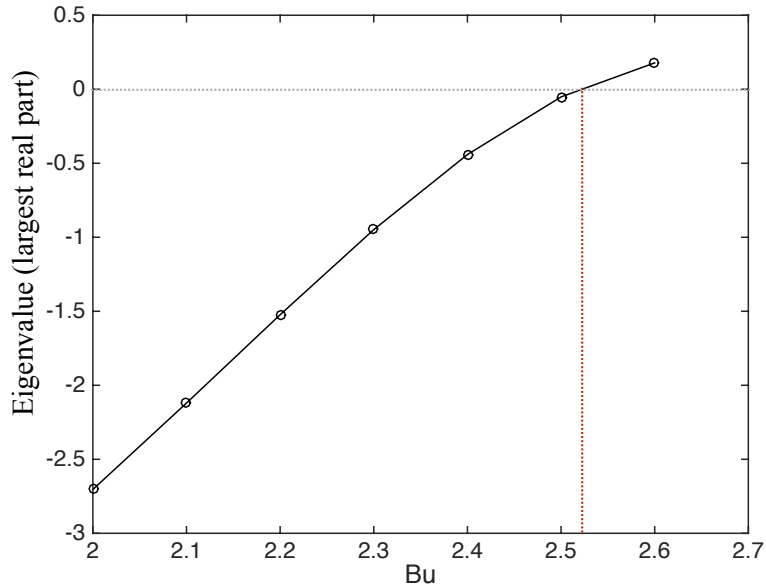


Fig. 5.13 Solution of the eigenvalue problem in Eq. 5.92 with the largest real part as a function of the Bundling number. The red dotted dash line indicated the critical point of transition from stable to unstable, which takes places slightly above $Bu = 2.5$.

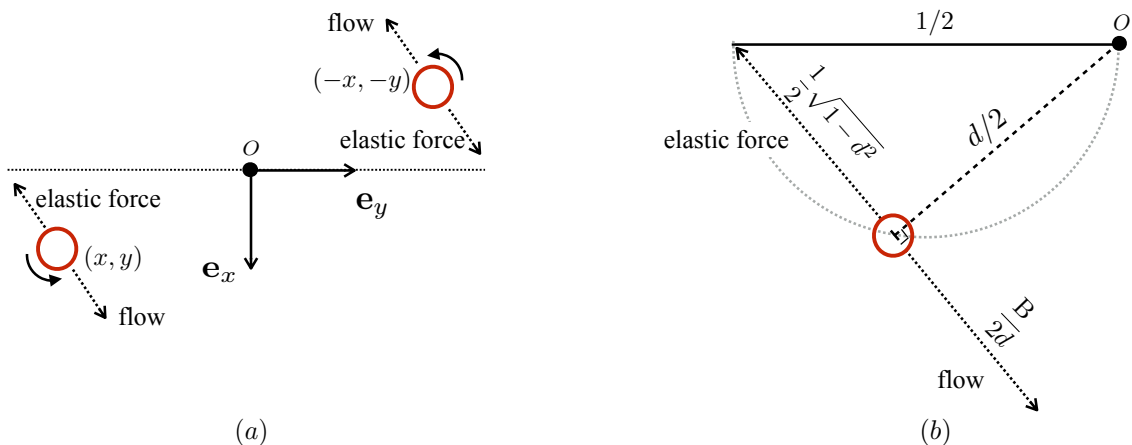


Fig. 5.14 (a) Setup for two-dimensional cylindrical model: two parallel rigid cylinders linked elastically to a reference position interaction hydrodynamically; (b) Geometric calculation of magnitude of forces.

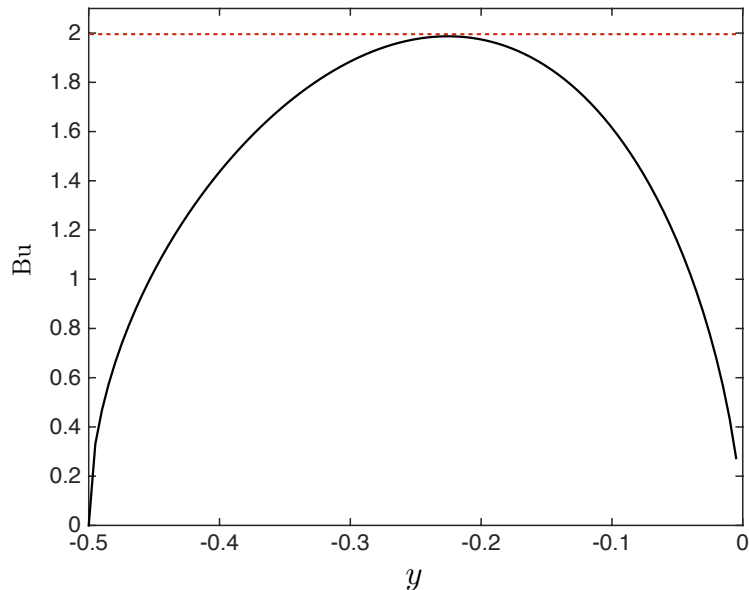


Fig. 5.15 Plot of B_u with respect to y , we found that the bundling number has a maximum with is around 2.

Chapter 6

Synchronisation of two nearby helices

The bundling of flagellar usually contains two effects that involve hydrodynamic interactions between filaments, which are attraction and synchronisation. In previous chapter, I propose a two-filament model for flagellar bundling, which address the process of attraction. However it is still not realistic enough as we ignore the helical geometry of the filament, which leads to the problem of synchronisation.

In recent years, several experimental and computational studies have been focused on the process of synchronisation. Kim etc. set up a macroscopic experiment of two relatively rigid helical filaments immersed in viscous fluid, and observed synchronisation of two helices [71]. This experiment proved that the synchronisation can be a consequence of interplay between the flow and the helical geometry. Subsequent numerical studies have clarified the problem further. Kim and Powers considered two completely rigid helices, the ends of which are fixed so only rotation motion are allowed [72]. With this setup, they measured the instantaneous force and torque on each helix and the phase difference between helices. However, the phase difference evolving with time did not show any synchronisation. Then Reichert and Stark used the same setup but applied an elastic recovery force at the end of the helices, which allowed the helix to tilt slightly [109]. As a result of that synchronisation was observed, elasticity was proved to be crucial.

As we know that analytically evaluating hydrodynamic integrations of flow singularities between nearby filaments have been thought as a challenging problem, and helical geometry can even increase the complexity. I demonstrate a new method to deal with hydrodynamic integrations between rods in Chapter. 4. Using the similar idea of long-wavelength assumption, I consider helical geometries in this chapter and measure the force and torque asymptotically. As illustrated in Chapter. 4 and 5, the main idea of the long-wavelength integration is achieved by taking advantage of a separation of length scales, which is assumed as $a \ll h \ll L$. When it comes to helical case, another length scale, the amplitude of the helix, b , should be consid-

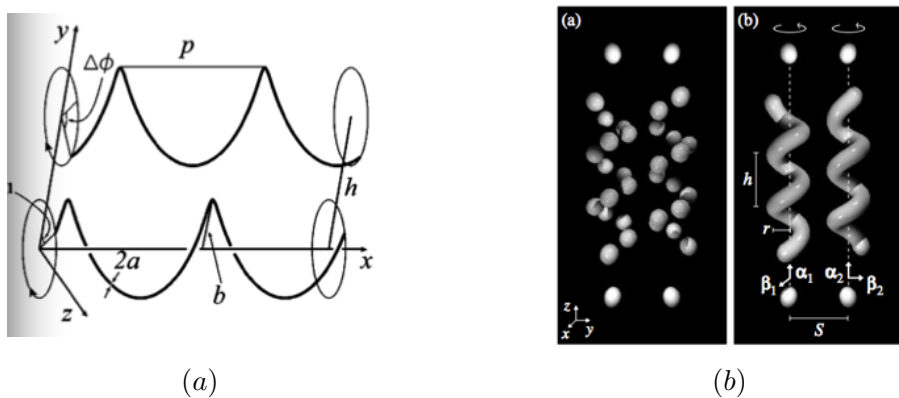


Fig. 6.1 Geometry considered in (a) Ref. [72] and (b) [109]. The difference is that in (a) the ends of helices are fixed while in (b) it allowed the helices to tilt slightly.

ered. Since I have already derived the result for rod case, it is natural to consider the solution perturbed with small amplitude of helix. Then in this study, I use a separation of length scales that $a \ll b \ll h \ll L$, using which I derive leading order force and torque, and then compare with numerical measurements in Ref. [72]. Furthermore, I propose a model that includes a recovery torque, which is a simple form representing the elastic effect. By calculating the phase difference evolving with time, synchronisation is observed. The derivations in this chapter provide a fully analytical model for synchronisation during flagellar bundling, the result can be applied to a variety of problems in which helical geometry is involved.

6.1 Hydrodynamic interactions between two helices

6.1.1 Set-up

Consider two identical helices shown in Fig. 6.2, each with radius a , amplitude b , wave length λ , and wave number k which is $2\pi/\lambda$. Another wavelength measured along the arc length s , is denoted Λ . We define the ratio between two wave lengths $\alpha = \lambda/\Lambda$ and then the helix angle is $\cos^{-1} \alpha$. Two helices are located with a fixed separation distance h between centerlines. With phase of helices denoted ϕ_1 and ϕ_2 , the position of the helices in cartesian coordinates are

$$\mathbf{r}_1 = [b \cos(k\alpha s + \phi_1), -\frac{h}{2} + b \sin(k\alpha s + \phi_1), \alpha s], \quad (6.1a)$$

$$\mathbf{r}_2 = [b \cos(k\alpha s + \phi_2), \frac{h}{2} + b \sin(k\alpha s + \phi_2), \alpha s], \quad (6.1b)$$

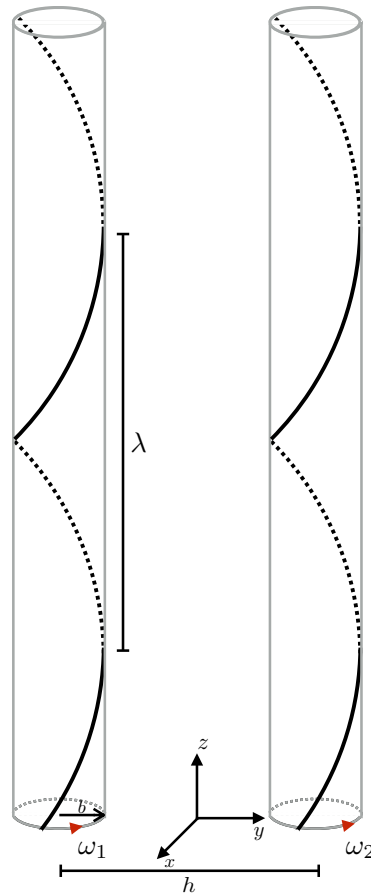


Fig. 6.2 Two identical helices with wavelength λ separated by a distance h between center-lines. The helices rotate with rotation rates ω_1 and ω_2 .

which has geometric constrain that

$$(b^2 k^2 + 1) \alpha^2 = 1. \quad (6.2)$$

Each helix rotates with a instantaneous rate ω_i ($i = 1, 2$) which is

$$\omega_i = \frac{\partial \phi_i}{\partial t}. \quad (6.3)$$

6.1.2 Hydrodynamic force

Now we consider the force exerted by the flow on the filaments which is \mathbf{f}_i . According to resistive force theory [88], we have

$$\mathbf{f}_1 = -[\xi_{\perp}\mathbf{I} + (\xi_{\parallel} - \xi_{\perp})\mathbf{t}_1\mathbf{t}_1] \cdot \left(\frac{\partial \mathbf{r}_1}{\partial t} - \mathbf{v}_{2 \rightarrow 1} \right), \quad (6.4a)$$

$$\mathbf{f}_2 = -[\xi_{\perp}\mathbf{I} + (\xi_{\parallel} - \xi_{\perp})\mathbf{t}_2\mathbf{t}_2] \cdot \left(\frac{\partial \mathbf{r}_2}{\partial t} - \mathbf{v}_{1 \rightarrow 2} \right), \quad (6.4b)$$

where $\xi_{\parallel, \perp}$ are resistance coefficients, \mathbf{t}_i is the tangential direction vector along the helix, and $\mathbf{v}_{j \rightarrow i}$ is the flow field induced by helix j around helix i . Approximately substitute

$$\xi_{\perp} = 2\xi_{\parallel}, \quad (6.5)$$

into Eq. 6.4, the force is simplified to

$$\mathbf{f}_1 = -\xi_{\perp} \left(\mathbf{I} - \frac{1}{2}\mathbf{t}_1\mathbf{t}_1 \right) \cdot \left(\frac{\partial \mathbf{r}_1}{\partial t} - \mathbf{v}_{2 \rightarrow 1} \right), \quad (6.6a)$$

$$\mathbf{f}_2 = -\xi_{\perp} \left(\mathbf{I} - \frac{1}{2}\mathbf{t}_2\mathbf{t}_2 \right) \cdot \left(\frac{\partial \mathbf{r}_2}{\partial t} - \mathbf{v}_{1 \rightarrow 2} \right). \quad (6.6b)$$

Similar with the definition in Chapter 4 and 5, the interaction term $\mathbf{v}_{j \rightarrow i}$ is represented by a line of flow singularities. With the assumption that the amplitude b is much larger than the radius a , the flow induced by translation motion should be more significant than that induced by rotation. Then we only consider stokeslets, take filament 1 as an example, the term relevant hydrodynamic interactions is

$$\mathbf{v}_{2 \rightarrow 1} = -\frac{1}{8\pi\mu} \int_0^L \mathbf{f}_2 \cdot \left(\frac{\mathbf{I}}{R} + \frac{\mathbf{R}\mathbf{R}}{R^3} \right) ds, \quad (6.7)$$

where

$$\mathbf{R}(s, s') = \mathbf{r}_1(s) - \mathbf{r}_2(s'), \quad R = |\mathbf{R}|. \quad (6.8)$$

6.1.3 Nondimensionalisation

In our set up, we have four length scales, total length L , amplitude b , separation distance h , radius of filament a . Keeping the previous length separation that $a \ll h \ll L$, we consider small amplitude which is much smaller than the separation distance but still much larger than the radius. Then four lengths satisfy $a \ll b \ll h \ll L$. By nondimensionalise all the lengths

with L , we obtain three small parameters,

$$\varepsilon_a = a/L, \quad \varepsilon_h = h/L, \quad \varepsilon_b = b/L. \quad (6.9)$$

In terms of time scale, since we consider the rotation rate ω_i changing with time, we assume the initial rotation rate is ω_{i0} and we take $1/\omega_{i0}$ as the time scale for nondimensionalisation. Then the dimensionless form of position vector is

$$\bar{\mathbf{r}}_1 = [\varepsilon_b \cos(2\pi n \alpha \bar{s} + \phi_1), \varepsilon_b \sin(2\pi n \alpha \bar{s} + \phi_1) - \frac{\varepsilon_h}{2}, \alpha \bar{s}], \quad (6.10a)$$

$$\bar{\mathbf{r}}_2 = [\varepsilon_b \cos(2\pi n \alpha \bar{s}' + \phi_2), \varepsilon_b \sin(2\pi n \alpha \bar{s}' + \phi_2) + \frac{\varepsilon_h}{2}, \alpha \bar{s}']. \quad (6.10b)$$

Notation-wisely, we drop the 'bars' for following derivations. If the force density is scaled as $8\pi\mu L\omega_{i0}$, Eq. 6.6 becomes

$$\mathbf{f}_1 = \frac{1}{2 \ln \varepsilon_a} \left(\mathbf{I} - \frac{1}{2} \mathbf{t}_1 \mathbf{t}_1 \right) \cdot \left(\frac{\partial \mathbf{r}_1}{\partial t} + \mathbf{J}_{2 \rightarrow 1} \cdot \mathbf{f}_2 \right) \quad (6.11a)$$

$$\mathbf{f}_2 = \frac{1}{2 \ln \varepsilon_a} \left(\mathbf{I} - \frac{1}{2} \mathbf{t}_2 \mathbf{t}_2 \right) \cdot \left(\frac{\partial \mathbf{r}_2}{\partial t} + \mathbf{J}_{1 \rightarrow 2} \cdot \mathbf{f}_1 \right), \quad (6.11b)$$

where

$$\mathbf{J}_{2 \rightarrow 1}(s) = \int_0^1 \frac{\mathbf{I}}{R} + \frac{\mathbf{R}\mathbf{R}}{R^3} ds'. \quad (6.12)$$

We move all the force terms to the left hand side, we obtain a linear system for the forces,

$$\mathbf{f}_1 - \frac{1}{2 \ln \varepsilon_a} \left(\mathbf{I} - \frac{1}{2} \mathbf{t}_1 \mathbf{t}_1 \right) \cdot \mathbf{J}_{2 \rightarrow 1} \cdot \mathbf{f}_2 = \frac{1}{2 \ln \varepsilon_a} \left(\mathbf{I} - \frac{1}{2} \mathbf{t}_1 \mathbf{t}_1 \right) \cdot \frac{\partial \mathbf{r}_1}{\partial t}, \quad (6.13a)$$

$$\mathbf{f}_2 - \frac{1}{2 \ln \varepsilon_a} \left(\mathbf{I} - \frac{1}{2} \mathbf{t}_2 \mathbf{t}_2 \right) \cdot \mathbf{J}_{1 \rightarrow 2} \cdot \mathbf{f}_1 = \frac{1}{2 \ln \varepsilon_a} \left(\mathbf{I} - \frac{1}{2} \mathbf{t}_2 \mathbf{t}_2 \right) \cdot \frac{\partial \mathbf{r}_2}{\partial t}. \quad (6.13b)$$

6.2 Asymptotic analysis with small amplitude

6.2.1 Expand as orders of ε_b

Since we have derived the force for rod case in Chapter 4, taking advantage of which, it is natural to consider the solution perturbed by small amplitude, or ε_b in dimensionless form. We thus expand Eq. 6.13 as orders of ε_b . First we expand all the variables that appear in

Eq. 6.13 as orders of ε_b ,

$$\mathbf{f}_i = \varepsilon_b \mathbf{f}_i^{(1)} + \varepsilon_b^2 \mathbf{f}_i^{(2)} + \dots \quad (6.14a)$$

$$\mathbf{t}_i = \mathbf{t}_i^{(0)} + \varepsilon_b \mathbf{t}_i^{(1)} + \dots \quad (6.14b)$$

$$\mathbf{J}_{j \rightarrow i} = \mathbf{J}_{j \rightarrow i}^{(0)} + \varepsilon_b \mathbf{J}_{j \rightarrow i}^{(1)} + \dots \quad (6.14c)$$

$$\mathbf{r}_i = \mathbf{r}_i^{(0)} + \varepsilon_b \mathbf{r}_i^{(1)} + \dots \quad (6.14d)$$

Substitute Eq. 6.14 into Eq. 6.13, we can solve the forces order by order. At zeroth order, which is the rod case, no forces can be generated because the displacement is zero. Then to obtain non-zero force, we need to consider at least order of ε_b , at which the equation is

$$\mathbf{f}_i^{(1)} - \frac{1}{2 \ln \varepsilon_a} \left(\mathbf{I} - \frac{1}{2} \mathbf{t}_i^{(0)} \mathbf{t}_i^{(0)} \right) \cdot \mathbf{J}_{j \rightarrow i}^{(0)} \cdot \mathbf{f}_j^{(1)} = \frac{1}{2 \ln \varepsilon_a} \left(\mathbf{I} - \frac{1}{2} \mathbf{t}_i^{(0)} \mathbf{t}_i^{(0)} \right) \cdot \frac{\partial \mathbf{r}_i^{(1)}}{\partial t}. \quad (6.15)$$

And for the next order, we have

$$\begin{aligned} \mathbf{f}_i^{(2)} - \frac{1}{2 \ln \varepsilon_a} \left(\mathbf{I} - \frac{1}{2} \mathbf{t}_i^{(0)} \mathbf{t}_i^{(0)} \right) \cdot \mathbf{J}_{j \rightarrow i}^{(0)} \cdot \mathbf{f}_j^{(2)} &= -\frac{1}{4 \ln \varepsilon_a} (\mathbf{t}_i^{(0)} \mathbf{t}_i^{(1)} + \mathbf{t}_i^{(1)} \mathbf{t}_i^{(0)}) \cdot \mathbf{J}_{j \rightarrow i}^{(0)} \cdot \mathbf{f}_j^{(1)} \\ &\quad + \frac{1}{2 \ln \varepsilon_a} \left(\mathbf{I} - \frac{1}{2} \mathbf{t}_i^{(0)} \mathbf{t}_i^{(0)} \right) \cdot \mathbf{J}_{j \rightarrow i}^{(1)} \cdot \mathbf{f}_j^{(1)} \\ &\quad - \frac{1}{4 \ln \varepsilon_a} (\mathbf{t}_i^{(0)} \mathbf{t}_i^{(1)} + \mathbf{t}_i^{(1)} \mathbf{t}_i^{(0)}) \cdot \frac{\partial \mathbf{r}_i^{(1)}}{\partial t} \\ &\quad + \frac{1}{2 \ln \varepsilon_a} \left[\mathbf{I} - \frac{1}{2} \mathbf{t}_i^{(0)} \mathbf{t}_i^{(0)} \right] \cdot \frac{\partial \mathbf{r}_i^{(2)}}{\partial t}. \end{aligned} \quad (6.16)$$

6.2.2 Expand position vector

The dimensionless form of Eq. 6.2 is

$$\alpha^2 + \frac{4\pi^2 \alpha^2 \varepsilon_b^2}{\lambda^2} = 1, \quad (6.17)$$

considering $1 = n\Lambda = n\lambda/\alpha$, the condition becomes

$$\alpha^2 + 4\pi^2 n^2 \varepsilon_b^2 = 1, \quad (6.18)$$

Then the ratio α can be expanded as

$$\begin{aligned}\alpha &= (1 - 4\pi^2 n^2 \varepsilon_b^2)^{-\frac{1}{2}} \\ &= 1 + 2\pi^2 n^2 \varepsilon_b^2 + O(\varepsilon_b^4).\end{aligned}\quad (6.19)$$

Substitute Eq. 6.19 into Eq. 6.10, we have the position vector expanded as

$$\mathbf{r}_i = \begin{bmatrix} 0 \\ \mp \frac{\varepsilon_h}{2} \\ s \end{bmatrix} + \varepsilon_b \begin{bmatrix} \cos \Phi_i \\ \sin \Phi_i \\ 0 \end{bmatrix} + \varepsilon_b^2 \begin{bmatrix} 0 \\ 0 \\ 2\pi^2 n^2 s \end{bmatrix} + O(\varepsilon_b^3), \quad (6.20)$$

where $\Phi_i = 2\pi n s + \phi_i$. Take derivative with respect to s , we obtain the expansion of tangential vector

$$\mathbf{t}_i = \begin{bmatrix} 0 \\ 0 \\ 1 \end{bmatrix} + 2\pi n \varepsilon_b \begin{bmatrix} -\sin \Phi_i \\ \cos \Phi_i \\ 0 \end{bmatrix} + O(\varepsilon_b^2). \quad (6.21)$$

In Eq. 6.13, tangential vector appears in a form of tensor $\mathbf{t}_i \mathbf{t}_i$, which can be expanded as

$$\mathbf{t}_i \mathbf{t}_i = \mathbf{t}_i^{(0)} \mathbf{t}_i^{(0)} + \varepsilon_b (\mathbf{t}_i^{(0)} \mathbf{t}_i^{(1)} + \mathbf{t}_i^{(1)} \mathbf{t}_i^{(0)}) + \dots \quad (6.22)$$

For calculation convenience, I use matrices or dyadics to represent tensor. Substitute Eq. 6.21 into Eq. 6.22, we obtain

$$\mathbf{t}_i^{(0)} \mathbf{t}_i^{(0)} = \mathbf{e}_z \mathbf{e}_z \equiv \begin{bmatrix} 0 & 0 & 0 \\ 0 & 0 & 0 \\ 0 & 0 & 1 \end{bmatrix}, \quad (6.23a)$$

$$\mathbf{t}_i^{(0)} \mathbf{t}_i^{(1)} + \mathbf{t}_i^{(1)} \mathbf{t}_i^{(0)} = 2\pi n \begin{bmatrix} 0 & 0 & -\sin \Phi_i \\ 0 & 0 & \cos \Phi_i \\ -\sin \Phi_i & \cos \Phi_i & 0 \end{bmatrix}. \quad (6.23b)$$

Take derivative of Eq. 6.20 with respect to time, we obtain the expansion of velocity of the deformation of each filament,

$$\frac{\partial \mathbf{r}_i}{\partial t} = \varepsilon_b \omega_i \begin{bmatrix} -\sin \Phi_i \\ \cos \Phi_i \\ 0 \end{bmatrix} + O(\varepsilon_b^3), \quad (6.24)$$

in which we apply the result that $\omega_i = \frac{\partial \Phi_i}{\partial t}$. Now we have obtained expansions of all the terms except interaction term $\mathbf{J}_{j \rightarrow i}$, which can be considered as a tensor. Since the procedure is more complicated, we derive in a separate section.

6.3 Expand hydrodynamic interaction term

6.3.1 Expand relative position vector \mathbf{R}

By introducing $\Delta = s - s'$, integration in Eq. 6.12 becomes

$$\mathbf{J}_{2 \rightarrow 1} = \int_{s-1}^s \frac{\mathbf{I}}{R} + \frac{\mathbf{R}\mathbf{R}}{R^3} d\Delta. \quad (6.25)$$

For notation convenience, we use \mathbf{J} to represent $\mathbf{J}_{2 \rightarrow 1}$ in this section and another term $\mathbf{J}_{1 \rightarrow 2}$ can be obtained by symmetry. Considering Eq. 6.20, \mathbf{R} can be expanded as

$$\begin{aligned} \mathbf{R} &= \mathbf{r}_1(s) - \mathbf{r}_2(s') \\ &= \begin{bmatrix} 0 \\ -\varepsilon_h \\ \Delta \end{bmatrix} + \varepsilon_b \begin{bmatrix} \delta_{\cos} \\ \delta_{\sin} \\ 0 \end{bmatrix} + \varepsilon_b^2 \begin{bmatrix} 0 \\ 0 \\ 2\pi^2 n^2 \Delta \end{bmatrix} + O(\varepsilon_b^3), \end{aligned} \quad (6.26)$$

where $\delta_{\cos} = \cos \Phi_1 - \cos \Phi_2$, and $\delta_{\sin} = \sin \Phi_1 - \sin \Phi_2$. Then the magnitude can be calculated as

$$\begin{aligned} R^2 &= \mathbf{R} \cdot \mathbf{R} \\ &= (\varepsilon_h^2 + \Delta^2) - 2\varepsilon_b \varepsilon_h \delta_{\sin} + O(\varepsilon_b^2), \end{aligned} \quad (6.27)$$

with which we can calculate

$$R^{-1} = (\varepsilon_h^2 + \Delta^2)^{-\frac{1}{2}} + \varepsilon_b \frac{\varepsilon_h \delta_{\sin}}{(\varepsilon_h^2 + \Delta^2)^{\frac{3}{2}}} + O(\varepsilon_b^2) \quad (6.28a)$$

$$R^{-3} = (\varepsilon_h^2 + \Delta^2)^{-\frac{3}{2}} + \varepsilon_b \frac{3\varepsilon_h \delta_{\sin}}{(\varepsilon_h^2 + \Delta^2)^{\frac{5}{2}}} + O(\varepsilon_b^2) \quad (6.28b)$$

Considering Eq. 6.26, the dyadic tensor $\mathbf{R}\mathbf{R}$ can be expanded as

$$\mathbf{R}\mathbf{R} = \mathbf{R}^{(0)}\mathbf{R}^{(0)} + \varepsilon_b [\mathbf{R}^{(0)}\mathbf{R}^{(1)} + \mathbf{R}^{(1)}\mathbf{R}^{(0)}] + O(\varepsilon_b^2), \quad (6.29)$$

where

$$\mathbf{R}^{(0)}\mathbf{R}^{(0)} = \begin{bmatrix} 0 & 0 & 0 \\ 0 & \varepsilon_h^2 & -\varepsilon_h\Delta \\ 0 & -\varepsilon_h\Delta & \Delta^2 \end{bmatrix} \quad (6.30a)$$

$$\mathbf{R}^{(0)}\mathbf{R}^{(1)} + \mathbf{R}^{(1)}\mathbf{R}^{(0)} = \begin{bmatrix} 0 & -\varepsilon_h\delta_{\cos} & \Delta\delta_{\cos} \\ -\varepsilon_h\delta_{\cos} & -2\varepsilon_h\delta_{\sin} & \Delta\delta_{\sin} \\ \Delta\delta_{\cos} & \Delta\delta_{\sin} & 0 \end{bmatrix}. \quad (6.30b)$$

6.3.2 Evaluate $\mathbf{J}^{(0)}$

Now we substitute Eq. 6.28 and 6.30 into Eq. 6.25 and combine Eq. 6.14c, we have

$$\mathbf{J}^{(0)} = \int_{s-1}^s \frac{\mathbf{I}}{(\varepsilon_h^2 + \Delta^2)^{\frac{1}{2}}} + \frac{1}{(\varepsilon_h^2 + \Delta^2)^{\frac{3}{2}}} \begin{bmatrix} 0 & 0 & 0 \\ 0 & \varepsilon_h^2 & -\varepsilon_h\Delta \\ 0 & -\varepsilon_h\Delta & \Delta^2 \end{bmatrix} d\Delta. \quad (6.31)$$

We choose an intermediate length δ that $\varepsilon_h \ll \delta \ll 1$, the integration is separated into local and non-local parts

$$\mathbf{J}_{NL}^{(0)} = \int_{s-1}^{-\delta} + \int_{-\delta}^s \frac{\mathbf{I}}{(\varepsilon_h^2 + \Delta^2)^{\frac{1}{2}}} + \frac{1}{(\varepsilon_h^2 + \Delta^2)^{\frac{3}{2}}} \begin{bmatrix} 0 & 0 & 0 \\ 0 & \varepsilon_h^2 & -\varepsilon_h\Delta \\ 0 & -\varepsilon_h\Delta & \Delta^2 \end{bmatrix} d\Delta, \quad (6.32a)$$

$$\mathbf{J}_L^{(0)} = \int_{-\delta}^{\delta} \frac{\mathbf{I}}{(\varepsilon_h^2 + \Delta^2)^{\frac{1}{2}}} + \frac{1}{(\varepsilon_h^2 + \Delta^2)^{\frac{3}{2}}} \begin{bmatrix} 0 & 0 & 0 \\ 0 & \varepsilon_h^2 & -\varepsilon_h\Delta \\ 0 & -\varepsilon_h\Delta & \Delta^2 \end{bmatrix} d\Delta. \quad (6.32b)$$

Since in the nonlocal region $\Delta \gg \varepsilon_h$,

$$\mathbf{J}_{NL}^{(0)} = \int_{s-1}^{-\delta} + \int_{-\delta}^s \frac{\mathbf{I}}{|\Delta|} + \frac{\mathbf{e}_z \mathbf{e}_z}{|\Delta|} d\Delta. \quad (6.33)$$

And in the local region, Δ should be the same order with ε_h . Using the results of integrals

$$\int_{s-1}^{-\delta} + \int_{-\delta}^s \frac{d\Delta}{|\Delta|} = -2\ln\delta + \ln s(1-s) + \dots, \quad (6.34a)$$

$$\int_{-\delta}^{\delta} \frac{d\Delta}{(\Delta^2 + \varepsilon_h^2)^{\frac{1}{2}}} = -2\ln\varepsilon_h + 2\ln\delta + 2\ln 2 + O\left(\frac{\varepsilon_h^2}{\delta^2}\right), \quad (6.34b)$$

$$\int_{-\delta}^{\delta} \frac{d\Delta}{(\Delta^2 + \varepsilon_h^2)^{\frac{3}{2}}} = \frac{2}{\varepsilon_h^2} - \frac{1}{\delta^2} + \dots, \quad (6.34c)$$

$$\int_{-\delta}^{\delta} \frac{d\Delta}{(\Delta^2 + \varepsilon_h^2)^{\frac{5}{2}}} = \frac{4}{3\varepsilon_h^4} + O\left(\frac{1}{\delta^2}\right), \quad (6.34d)$$

we calculate Eq. 6.32 as

$$\mathbf{J}_{NL}^{(0)} = -2\ln\delta(\mathbf{I} + \mathbf{e}_z\mathbf{e}_z), \quad (6.35a)$$

$$\mathbf{J}_L^{(0)} = (-2\ln\varepsilon_h + 2\ln\delta)(\mathbf{I} + \mathbf{e}_z\mathbf{e}_z). \quad (6.35b)$$

Adding up two parts and δ can be cancelled out, finally we have

$$\mathbf{J}^{(0)} = -2\ln\varepsilon_h(\mathbf{I} + \mathbf{e}_z\mathbf{e}_z). \quad (6.36)$$

6.3.3 Evaluate $\mathbf{J}^{(1)}$

Now we move to the next order. Substitute expansions in Eq. 6.28, 6.30 and 6.14c into Eq. 6.25, we have

$$\begin{aligned} \mathbf{J}^{(1)} &= \int_{s-1}^s \frac{\varepsilon_h \delta_{\sin}}{(\varepsilon_h^2 + \Delta^2)^{\frac{3}{2}}} \mathbf{I} + \frac{1}{(\varepsilon_h^2 + \Delta^2)^{\frac{3}{2}}} \begin{bmatrix} 0 & -\varepsilon_h \delta_{\cos} & \Delta \delta_{\cos} \\ -\varepsilon_h \delta_{\cos} & -2\varepsilon_h \delta_{\sin} & \Delta \delta_{\sin} \\ \Delta \delta_{\cos} & \Delta \delta_{\sin} & 0 \end{bmatrix} \\ &\quad + \frac{3\varepsilon_h \delta_{\sin}}{(\varepsilon_h^2 + \Delta^2)^{\frac{5}{2}}} \begin{bmatrix} 0 & 0 & 0 \\ 0 & \varepsilon_h^2 & -\varepsilon_h \Delta \\ 0 & -\varepsilon_h \Delta & \Delta^2 \end{bmatrix} d\Delta. \end{aligned} \quad (6.37)$$

In order to calculate Eq. 6.37, we need long-wavelength assumption as illustrated in Chapter. 4 and 5. We assume the phase changes slowly along the helix, then $\delta \sin$ and $\delta \cos$ can be expanded as

$$\delta_{\cos} = \delta_{\cos}|_{\Delta=0} + O(\Delta), \quad (6.38a)$$

$$\delta_{\sin} = \delta_{\sin}|_{\Delta=0} + O(\Delta). \quad (6.38b)$$

There are three terms in the integration, then we evaluate them one by one. Substitute Eq. 6.38 and results of integrals in Eq. 6.34 into the first part of integration, we obtain

$$\int_{s-1}^s \frac{\varepsilon_h \delta_{\sin}}{(\varepsilon_h^2 + \Delta^2)^{\frac{3}{2}}} \mathbf{I} d\Delta \sim \frac{2}{\varepsilon_h} \delta_{\sin}|_{\Delta=0} \mathbf{I}. \quad (6.39)$$

Then the second term is evaluated as

$$\int_{s-1}^s \frac{d\Delta}{(\varepsilon_h^2 + \Delta^2)^{\frac{3}{2}}} \begin{bmatrix} 0 & -\varepsilon_h \delta_{\cos} & \Delta \delta_{\cos} \\ -\varepsilon_h \delta_{\cos} & -2\varepsilon_h \delta_{\sin} & \Delta \delta_{\sin} \\ \Delta \delta_{\cos} & \Delta \delta_{\sin} & 0 \end{bmatrix} \sim -\frac{2}{\varepsilon_h} \begin{bmatrix} 0 & \delta_{\cos}|_{\Delta=0} & 0 \\ \delta_{\cos}|_{\Delta=0} & 2\delta_{\sin}|_{\Delta=0} & 0 \\ 0 & 0 & 0 \end{bmatrix}. \quad (6.40)$$

Then the last term is

$$\int_{s-1}^s \frac{3\varepsilon_h \delta_{\sin}}{(\varepsilon_h^2 + \Delta^2)^{\frac{5}{2}}} \begin{bmatrix} 0 & 0 & 0 \\ 0 & \varepsilon_h^2 & -\varepsilon_h \Delta \\ 0 & -\varepsilon_h \Delta & \Delta^2 \end{bmatrix} d\Delta \sim \frac{2}{\varepsilon_h} \delta_{\sin}|_{\Delta=0} \begin{bmatrix} 0 & 0 & 0 \\ 0 & 2 & 0 \\ 0 & 0 & 1 \end{bmatrix}. \quad (6.41)$$

Add three parts Eq. 6.39, 6.40 and 6.41 together, we obtain

$$\mathbf{J}^{(1)} = \frac{2}{\varepsilon_h} \begin{bmatrix} \delta_{\sin}|_{\Delta=0} & -\delta_{\cos}|_{\Delta=0} & 0 \\ -\delta_{\cos}|_{\Delta=0} & \delta_{\sin}|_{\Delta=0} & 0 \\ 0 & 0 & 2\delta_{\sin}|_{\Delta=0} \end{bmatrix}. \quad (6.42)$$

6.4 Evaluate torque and force

6.4.1 Torque

Now we have calculated all the expansions for $\mathbf{t}_i \mathbf{t}_i$, $\frac{\partial \mathbf{r}_i}{\partial t}$ and $\mathbf{J}_{j \rightarrow i}$. Substitute Eq. 6.23a, 6.24 and 6.36 into Eq. 6.15, and introduce a ratio that

$$\beta = \frac{\ln \varepsilon_h}{\ln \varepsilon_a} < 1, \quad (6.43)$$

we have first order equation

$$\mathbf{f}_1^{(1)} + \beta \left(\mathbf{I} - \frac{1}{2} \mathbf{e}_z \mathbf{e}_z \right) \cdot (\mathbf{I} + \mathbf{e}_z \mathbf{e}_z) \mathbf{f}_2^{(1)} = \frac{\omega_1}{2 \ln \epsilon_a} \left(\mathbf{I} - \frac{1}{2} \mathbf{e}_z \mathbf{e}_z \right) \cdot \begin{bmatrix} -\sin \Phi_1 \\ \cos \Phi_1 \\ 0 \end{bmatrix}, \quad (6.44a)$$

$$\mathbf{f}_2^{(1)} + \beta \left(\mathbf{I} - \frac{1}{2} \mathbf{e}_z \mathbf{e}_z \right) \cdot (\mathbf{I} + \mathbf{e}_z \mathbf{e}_z) \mathbf{f}_1^{(1)} = \frac{\omega_2}{2 \ln \epsilon_a} \left(\mathbf{I} - \frac{1}{2} \mathbf{e}_z \mathbf{e}_z \right) \cdot \begin{bmatrix} -\sin \Phi_2 \\ \cos \Phi_2 \\ 0 \end{bmatrix}. \quad (6.44b)$$

Using the result that

$$\left(\mathbf{I} - \frac{1}{2} \mathbf{e}_z \mathbf{e}_z \right) \cdot (\mathbf{I} + \mathbf{e}_z \mathbf{e}_z) = \mathbf{I}, \quad (6.45)$$

and

$$\mathbf{e}_z \cdot \begin{bmatrix} -\sin \Phi_i \\ \cos \Phi_i \\ 0 \end{bmatrix} = 0, \quad (6.46)$$

Eq. 6.44 is simplified to

$$\mathbf{f}_1^{(1)} + \beta \mathbf{f}_2^{(1)} = \frac{\omega_1}{2 \ln \epsilon_a} \begin{bmatrix} -\sin \Phi_1 \\ \cos \Phi_1 \\ 0 \end{bmatrix}, \quad (6.47a)$$

$$\mathbf{f}_2^{(1)} + \beta \mathbf{f}_1^{(1)} = \frac{\omega_2}{2 \ln \epsilon_a} \begin{bmatrix} -\sin \Phi_2 \\ \cos \Phi_2 \\ 0 \end{bmatrix}. \quad (6.47b)$$

Eq. 6.47 is a linear system and the forces are solved as

$$(1 - \beta^2) \mathbf{f}_1^{(1)}(s) = \frac{\omega_1}{2 \ln \epsilon_a} \begin{bmatrix} -\sin \Phi_1 \\ \cos \Phi_1 \\ 0 \end{bmatrix} - \frac{\beta \omega_2}{2 \ln \epsilon_a} \begin{bmatrix} -\sin \Phi_2|_{s'=s} \\ \cos \Phi_2|_{s'=s} \\ 0 \end{bmatrix}, \quad (6.48a)$$

$$(1 - \beta^2) \mathbf{f}_2^{(1)}(s') = \frac{\omega_2}{2 \ln \epsilon_a} \begin{bmatrix} -\sin \Phi_2 \\ \cos \Phi_2 \\ 0 \end{bmatrix} - \frac{\beta \omega_1}{2 \ln \epsilon_a} \begin{bmatrix} -\sin \Phi_1|_{s=s'} \\ \cos \Phi_1|_{s=s'} \\ 0 \end{bmatrix}. \quad (6.48b)$$

Then we consider the torque along z direction

$$m_i = \left(\mathbf{r}_i \pm \frac{1}{2} \mathbf{e}_y \right) \times \mathbf{f}_i \cdot \mathbf{e}_z. \quad (6.49)$$

We observe that the leading order should be the order of ϵ_b^2 , then we expand it as

$$m_i = \epsilon_b^2 m_i^{(2)} + \dots, \quad (6.50)$$

where

$$m_i^{(2)} = \mathbf{r}_i^{(1)} \times \mathbf{f}_i^{(1)} \cdot \mathbf{e}_z. \quad (6.51)$$

Substitute Eq. 6.20 and 6.48 into Eq. 6.51, and use the result that

$$\begin{bmatrix} \cos \Phi_i \\ \sin \Phi_i \\ 0 \end{bmatrix} \times \begin{bmatrix} -\sin \Phi_i \\ \cos \Phi_i \\ 0 \end{bmatrix} \cdot \mathbf{e}_z = 1, \quad (6.52a)$$

$$\begin{bmatrix} \cos \Phi_i \\ \sin \Phi_i \\ 0 \end{bmatrix} \times \begin{bmatrix} -\sin \Phi_j \\ \cos \Phi_j \\ 0 \end{bmatrix} \cdot \mathbf{e}_z = \cos(\Phi_i - \Phi_j) = \cos(\phi_i - \phi_j), \quad (6.52b)$$

we have

$$(1 - \beta^2) m_1^{(2)} = \frac{\omega_1}{2 \ln \epsilon_a} - \frac{\beta \omega_2}{2 \ln \epsilon_a} \cos \Delta\phi \quad (6.53a)$$

$$(1 - \beta^2) m_2^{(1)} = \frac{\omega_2}{2 \ln \epsilon_a} - \frac{\beta \omega_1}{2 \ln \epsilon_a} \cos \Delta\phi, \quad (6.53b)$$

where $\Delta\phi = \phi_1 - \phi_2$.

If we write linear system in Eq. 6.53 with the form of matrix, we have

$$\begin{bmatrix} m_1 \\ m_2 \end{bmatrix} = \frac{\epsilon_b^2}{2(1 - \beta^2) \ln \epsilon_a} \begin{bmatrix} 1 & -\beta \cos \Delta\phi \\ -\beta \cos \Delta\phi & 1 \end{bmatrix} \begin{bmatrix} \omega_1 \\ \omega_2 \end{bmatrix}. \quad (6.54)$$

6.4.2 Force

We have obtained the first order force in Eq. 6.48, integrate it along the centerline, the net force is zero. To obtain non-zero force, we need to move to the next order. Substitute expansions in Eq. 6.23, 6.24, 6.36 and 6.42 into second order equation in Eq. 6.16, we have

$$\begin{aligned}
\mathbf{f}_i^{(2)} + \beta \mathbf{f}_j^{(2)} &= \pi n \beta \begin{bmatrix} 0 & 0 & -\sin \Phi_i \\ 0 & 0 & \cos \Phi_i \\ -\sin \Phi_i & \cos \Phi_i & 0 \end{bmatrix} \begin{bmatrix} 1 & 0 & 0 \\ 0 & 1 & 0 \\ 0 & 0 & 2 \end{bmatrix} \mathbf{f}_j^{(1)} \\
&+ \frac{1}{\epsilon_h \ln \epsilon_a} \begin{bmatrix} 1 & 0 & 0 \\ 0 & 1 & 0 \\ 0 & 0 & \frac{1}{2} \end{bmatrix} \begin{bmatrix} \delta_{\sin} & -\delta_{\cos} & 0 \\ -\delta_{\cos} & \delta_{\sin} & 0 \\ 0 & 0 & 2\delta_{\sin} \end{bmatrix} \mathbf{f}_j^{(1)} \\
&- \frac{\pi n \omega_i}{2 \ln \epsilon_a} \begin{bmatrix} 0 & 0 & -\sin \Phi_i \\ 0 & 0 & \cos \Phi_i \\ -\sin \Phi_i & \cos \Phi_i & 0 \end{bmatrix} \begin{bmatrix} -\sin \Phi_i \\ \cos \Phi_i \\ 0 \end{bmatrix}.
\end{aligned} \tag{6.55}$$

Calculate

$$\begin{bmatrix} 0 & 0 & -\sin \Phi_i \\ 0 & 0 & \cos \Phi_i \\ -\sin \Phi_i & \cos \Phi_i & 0 \end{bmatrix} \begin{bmatrix} 1 & 0 & 0 \\ 0 & 1 & 0 \\ 0 & 0 & 2 \end{bmatrix} = \begin{bmatrix} 0 & 0 & -2\sin \Phi_i \\ 0 & 0 & 2\cos \Phi_i \\ -\sin \Phi_i & \cos \Phi_i & 0 \end{bmatrix}, \tag{6.56}$$

$$\begin{bmatrix} 1 & 0 & 0 \\ 0 & 1 & 0 \\ 0 & 0 & \frac{1}{2} \end{bmatrix} \begin{bmatrix} \delta_{\sin} & -\delta_{\cos} & 0 \\ -\delta_{\cos} & \delta_{\sin} & 0 \\ 0 & 0 & 2\delta_{\sin} \end{bmatrix} = \begin{bmatrix} \delta_{\sin} & -\delta_{\cos} & 0 \\ -\delta_{\cos} & \delta_{\sin} & 0 \\ 0 & 0 & \delta_{\sin} \end{bmatrix}, \tag{6.57}$$

and

$$\begin{bmatrix} 0 & 0 & -\sin \Phi_i \\ 0 & 0 & \cos \Phi_i \\ -\sin \Phi_i & \cos \Phi_i & 0 \end{bmatrix} \begin{bmatrix} -\sin \Phi_i \\ \cos \Phi_i \\ 0 \end{bmatrix} = \mathbf{e}_z, \tag{6.58}$$

Eq. 6.55 is simplified to

$$\begin{aligned} \mathbf{f}_i^{(2)} + \beta \mathbf{f}_j^{(2)} &= \pi n \beta \begin{bmatrix} 0 & 0 & -2 \sin \Phi_i \\ 0 & 0 & 2 \cos \Phi_i \\ -\sin \Phi_i & \cos \Phi_i & 0 \end{bmatrix} \mathbf{f}_j^{(1)} \\ &\quad + \frac{1}{\epsilon_h \ln \epsilon_a} \begin{bmatrix} \delta_{\sin} & -\delta_{\cos} & 0 \\ -\delta_{\cos} & \delta_{\sin} & 0 \\ 0 & 0 & \delta_{\sin} \end{bmatrix} \mathbf{f}_j^{(1)} \\ &\quad - \frac{\pi n \omega_i}{2 \ln \epsilon_a} \mathbf{e}_z. \end{aligned} \quad (6.59)$$

Then we substitute Eq. 6.48 into Eq. 6.59, and use the result that

$$\begin{bmatrix} 0 & 0 & -2 \sin \Phi_i \\ 0 & 0 & 2 \cos \Phi_i \\ -\sin \Phi_i & \cos \Phi_i & 0 \end{bmatrix} \begin{bmatrix} -\sin \Phi_j \\ \cos \Phi_j \\ 0 \end{bmatrix} = \cos \Delta \phi \mathbf{e}_z, \quad (6.60)$$

and

$$\begin{bmatrix} 0 & 0 & -2 \sin \Phi_i \\ 0 & 0 & 2 \cos \Phi_i \\ -\sin \Phi_i & \cos \Phi_i & 0 \end{bmatrix} \begin{bmatrix} -\sin \Phi_i \\ \cos \Phi_i \\ 0 \end{bmatrix} = \mathbf{e}_z, \quad (6.61)$$

and we simplify the first term

$$\begin{bmatrix} 0 & 0 & -2 \sin \Phi_i \\ 0 & 0 & 2 \cos \Phi_i \\ -\sin \Phi_i & \cos \Phi_i & 0 \end{bmatrix} \mathbf{f}_j^{(1)} = \frac{1}{2(1-\beta^2) \ln \epsilon_a} (\cos \Delta \phi \omega_j - \beta \omega_i) \mathbf{e}_z. \quad (6.62)$$

Then add the first and third term together we have

$$\begin{aligned} &\pi n \beta \begin{bmatrix} 0 & 0 & -2 \sin \Phi_i \\ 0 & 0 & 2 \cos \Phi_i \\ -\sin \Phi_i & \cos \Phi_i & 0 \end{bmatrix} \mathbf{f}_j^{(1)} - \frac{\pi n \omega_i}{2 \ln \epsilon_a} \mathbf{e}_z \\ &= \frac{\pi n \beta}{2(1-\beta^2) \ln \epsilon_a} (\cos \Delta \phi \omega_j - \beta \omega_i) \mathbf{e}_z - \frac{\pi n \omega_i}{2 \ln \epsilon_a} \mathbf{e}_z \\ &= \frac{\pi n}{2(1-\beta^2) \ln \epsilon_a} (\beta \cos \Delta \phi \omega_j - \omega_i) \mathbf{e}_z, \end{aligned} \quad (6.63)$$

and Eq. 6.59 becomes

$$\begin{aligned} \mathbf{f}_i^{(2)} + \beta \mathbf{f}_j^{(2)} &= \frac{1}{\epsilon_h \ln \epsilon_a} \begin{bmatrix} \delta_{\sin} & -\delta_{\cos} & 0 \\ -\delta_{\cos} & \delta_{\sin} & 0 \\ 0 & 0 & \delta_{\sin} \end{bmatrix} \mathbf{f}_j^{(1)} \\ &\quad + \frac{\pi n}{2(1-\beta^2) \ln \epsilon_a} (\beta \cos \Delta\phi \omega_j - \omega_i) \mathbf{e}_z. \end{aligned} \quad (6.64)$$

Next we substitute Eq. 6.48 into Eq. 6.64 and calculate

$$\begin{bmatrix} \delta_{\sin} & -\delta_{\cos} & 0 \\ -\delta_{\cos} & \delta_{\sin} & 0 \\ 0 & 0 & \delta_{\sin} \end{bmatrix} \begin{bmatrix} -\sin \Phi_j \\ \cos \Phi_j \\ 0 \end{bmatrix} = \begin{bmatrix} 1 - \cos \Delta\phi \\ \sin(\Phi_1 + \Phi_2) - \sin 2\Phi_j \\ 0 \end{bmatrix}, \quad (6.65)$$

and

$$\begin{bmatrix} \delta_{\sin} & -\delta_{\cos} & 0 \\ -\delta_{\cos} & \delta_{\sin} & 0 \\ 0 & 0 & \delta_{\sin} \end{bmatrix} \begin{bmatrix} -\sin \Phi_i \\ \cos \Phi_i \\ 0 \end{bmatrix} = \begin{bmatrix} -1 + \cos \Delta\phi \\ -\sin(\Phi_1 + \Phi_2) + \sin 2\Phi_i \\ 0 \end{bmatrix}, \quad (6.66)$$

apply this result, Eq. 6.64 is finally simplified to

$$\begin{aligned} \mathbf{f}_i^{(2)} + \beta \mathbf{f}_j^{(2)} &= \frac{1}{2(1-\beta^2) \epsilon_h \ln^2 \epsilon_a} \left(\omega_j \begin{bmatrix} 1 - \cos \Delta\phi \\ \sin(\Phi_1 + \Phi_2) - \sin 2\Phi_j \\ 0 \end{bmatrix} \right. \\ &\quad \left. + \beta \omega_i \begin{bmatrix} 1 - \cos \Delta\phi \\ \sin(\Phi_1 + \Phi_2) - \sin 2\Phi_i \\ 0 \end{bmatrix} \right) \\ &\quad + \frac{\pi n}{2(1-\beta^2) \ln \epsilon_a} (\beta \cos \Delta\phi \omega_j - \omega_i) \mathbf{e}_z. \end{aligned} \quad (6.67)$$

We see that on the right hand side of this equation, first two terms are related to x, y -components while the last term is related to z -component, so we calculate separately. First we consider the system for z component which is

$$f_{1z}^{(2)} + \beta f_{2z}^{(2)} = \frac{\pi n}{2(1-\beta^2) \ln \epsilon_a} (\beta \cos \Delta\phi \omega_2 - \omega_1), \quad (6.68a)$$

$$f_{2z}^{(2)} + \beta f_{1z}^{(2)} = \frac{\pi n}{2(1-\beta^2) \ln \epsilon_a} (\beta \cos \Delta\phi \omega_1 - \omega_2). \quad (6.68b)$$

The solution of Eq. 6.68 is

$$f_{iz}^{(2)} = \frac{\pi n}{2(1-\beta^2)^2 \ln \varepsilon_a} [-(1+\beta^2 \cos \Delta\phi) \omega_i + \beta(\cos \Delta\phi + 1) \omega_j], \quad (6.69)$$

or in matrix form

$$\begin{bmatrix} f_{1z}^{(2)} \\ f_{2z}^{(2)} \end{bmatrix} = \frac{\pi n}{2(1-\beta^2)^2 \ln \varepsilon_a} \begin{bmatrix} -(1+\beta^2 \cos \Delta\phi) & \beta(\cos \Delta\phi + 1) \\ \beta(\cos \Delta\phi + 1) & -(1+\beta^2 \cos \Delta\phi) \end{bmatrix} \begin{bmatrix} \omega_1 \\ \omega_2 \end{bmatrix}. \quad (6.70)$$

Next we calculate x -component $f_{ix}^{(2)}$, according to Eq. 6.67, we have

$$f_{ix}^{(2)} + \beta f_{jx}^{(2)} = \frac{1 - \cos \Delta\phi}{2(1-\beta^2) \varepsilon_h \ln^2 \varepsilon_a} (\omega_j + \beta \omega_i), \quad (6.71)$$

the solution of which is

$$f_{ix}^{(2)} = \frac{1 - \cos \Delta\phi}{2(1-\beta^2) \varepsilon_h \ln^2 \varepsilon_a} \omega_j. \quad (6.72)$$

At last we consider y -direction, the equation is

$$\begin{aligned} f_{iy}^{(2)} + \beta f_{jy}^{(2)} &= \frac{1}{2(1-\beta^2) \varepsilon_h \ln^2 \varepsilon_a} \{ [\sin(\Phi_1 + \Phi_2) - \sin 2\Phi_j] \omega_j \\ &\quad + \beta [\sin(\Phi_1 + \Phi_2) - \sin 2\Phi_i] \omega_i \}. \end{aligned} \quad (6.73)$$

And it is solved as

$$f_{iy}^{(2)} = \frac{\sin(\Phi_1 + \Phi_2) - \sin 2\Phi_j}{2(1-\beta^2) \varepsilon_h \ln^2 \varepsilon_a} \omega_j. \quad (6.74)$$

We see that force is linear with the rotation rates. For x and y components, the forces only depend on the rotation rate of the other helix, while the force along z direction depends on both. If we choose constant rotation rate ω_i , we can take average by time of Eq. 6.69, 6.72 and 6.74 and obtain

$$\langle f_{ix}^{(2)} \rangle_t = \frac{\omega_j}{2(1-\beta^2) \varepsilon_h \ln^2 \varepsilon_a} \quad (6.75a)$$

$$\langle f_{iy}^{(2)} \rangle_t = 0 \quad (6.75b)$$

$$\langle f_{iz}^{(2)} \rangle_t = \frac{\pi n}{2(1-\beta^2)^2 \ln \varepsilon_a} (-\omega_i + \beta \omega_j). \quad (6.75c)$$

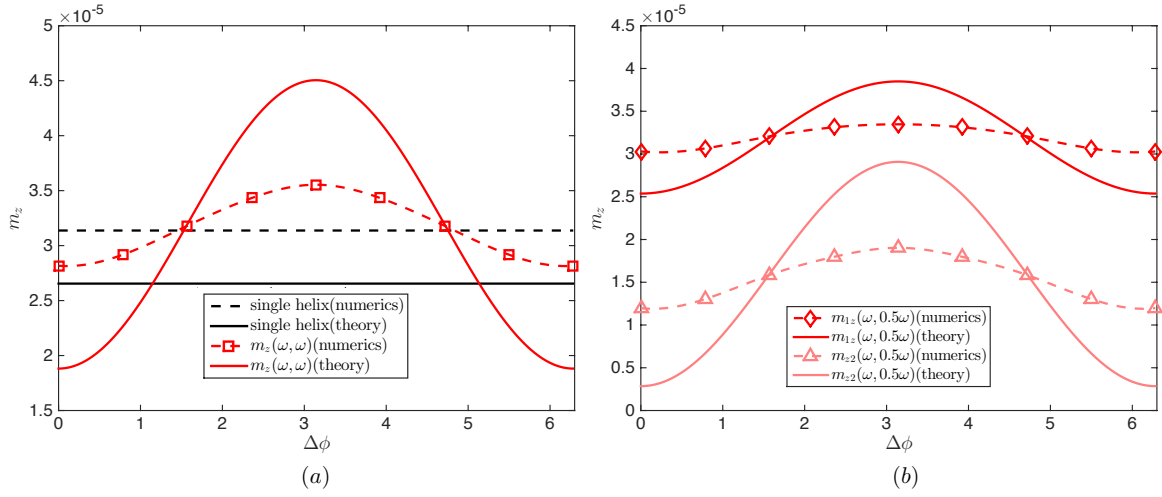


Fig. 6.3 Compare torque along z direction with the numerical result in Ref. [72].

Also, we can consider the net force along the helix. If the number of turns n is an integer, we see that the instantaneous force along y -direction is zero,

$$\langle f_{iy}^{(2)} \rangle_s = 0. \quad (6.76)$$

6.5 Compare with numerics

In Ref. [72], Kim and Powers numerically measured the torque and force along z direction. We compare our result with it in this section. They use two helices with four turns ($n=4$) with separation $h = 3b$. Using our notation, the three small parameters are approximately

$$\epsilon_a = 10^{-3}, \quad \epsilon_b = 0.02, \quad \epsilon_h = 0.06. \quad (6.77)$$

And the parameter β is approximately 0.4. Substitute these parameters into our results for torque in Eq. 6.54 and 6.69, and nondimensionalise the data in Ref. [72], we plot the z component of torque and time-averaged force in Fig. 6.3 and Fig. 6.4 respectively.

Kim and Powers inferred from numerical measurements that the torque only depends on the phase difference $\Delta\phi$ and it is largest when the phase difference is π . Both features have been captured by our result in Eq. 6.54. If we write the torque density in matrix as

$$\begin{bmatrix} m_1 \\ m_2 \end{bmatrix} = \mathbf{A} \begin{bmatrix} \omega_1 \\ \omega_2 \end{bmatrix}, \quad (6.78)$$

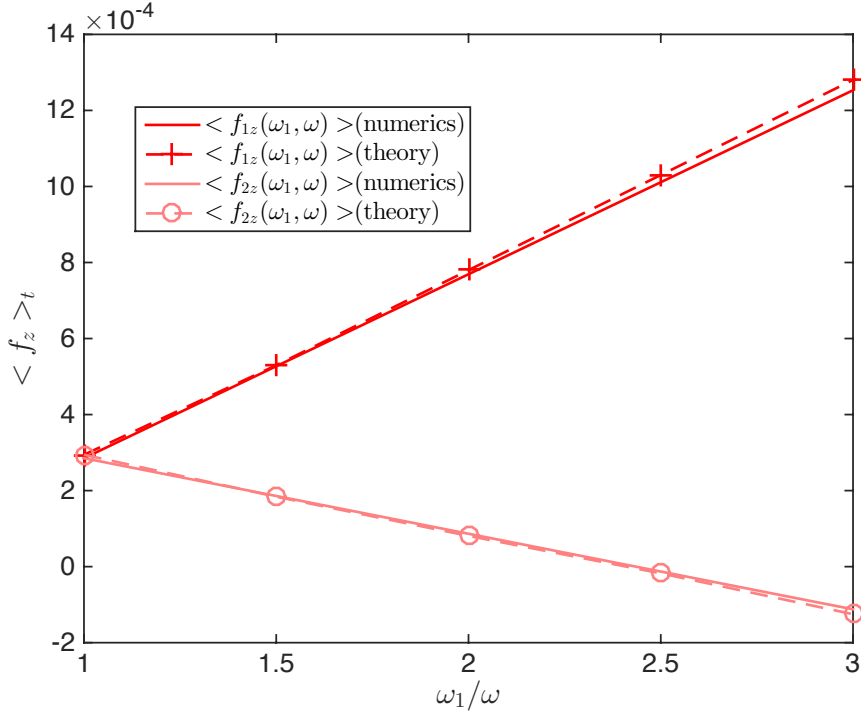


Fig. 6.4 Compare time-averaged force along z direction with the numerical result in Ref. [72].

according our theory, the matrix is calculated as

$$\mathbf{A} = 10^{-5} \times \begin{bmatrix} 3.19 & -1.31 \cos \Delta\phi \\ -1.31 \cos \Delta\phi & 3.19 \end{bmatrix}, \quad (6.79)$$

while the numerical measurement is approximately

$$\mathbf{A} = 10^{-5} \times \begin{bmatrix} 3.23 & -0.36 \cos \Delta\phi \\ -0.36 \cos \Delta\phi & 3.23 \end{bmatrix}. \quad (6.80)$$

We see that if we take average with time, the magnitude of the torque matches very well. And the force along z direction, which is called anchoring force, our result makes a good agreement with numerical measurements. According to Eq. 6.75c, the time-averaged force is linear with both ω_1 and ω_2 . In Fig. 6.4, we fix ω_2 , then the force changes linearly with ω_1 , with slope $\frac{\pi n}{2(1-\beta^2)^2 \ln(1/\varepsilon_a)}$ and $-\frac{\pi n \beta}{2(1-\beta^2)^2 \ln(1/\varepsilon_a)}$ for helix 1 and 2 respectively.

6.6 Synchronisation with recovery torque

In the last section, I propose a simple model with recovery torque. Just add a recovery torque linear with phase to represent the elastic effect, which is

$$m_r = -K\phi, \quad (6.81)$$

where K is a positive constant. Combine Eq. 6.54, we have the torque balance that

$$\frac{\varepsilon_b^2}{2(1-\beta^2)\ln\varepsilon_a} \begin{bmatrix} 1 & -\beta \cos \Delta\phi \\ -\beta \cos \Delta\phi & 1 \end{bmatrix} \begin{bmatrix} \omega_1 \\ \omega_2 \end{bmatrix} - K \begin{bmatrix} \phi_1 \\ \phi_2 \end{bmatrix} = \mathbf{0}. \quad (6.82)$$

Subtract two equations, and use

$$\omega_1 - \omega_2 = \frac{d\Delta\phi}{dt}, \quad (6.83)$$

we have a first order ODE of $\Delta\phi$,

$$\frac{\varepsilon_b^2}{2(1-\beta^2)\ln\varepsilon_a} (1 + \beta \cos \Delta\phi) \frac{d\Delta\phi}{dt} - K\Delta\phi = 0, \quad (6.84)$$

or

$$\frac{d\Delta\phi}{dt} = \frac{2K(1-\beta^2)\ln\varepsilon_a}{\varepsilon_b^2} \frac{\Delta\phi}{(1 + \beta \cos \Delta\phi)}. \quad (6.85)$$

We see that this equation has only one critical point which is

$$\Delta\phi = 0. \quad (6.86)$$

In order to check the stability at $\Delta\phi = 0$ we calculate

$$\left. \frac{\partial}{\partial \Delta\phi} \left[\frac{\Delta\phi}{(1 + \beta \cos \Delta\phi)} \right] \right|_{\Delta\phi=0} = \frac{1}{1 + \beta}. \quad (6.87)$$

Since

$$\beta < 1, \quad (6.88)$$

and then

$$\frac{2K(1-\beta^2)\ln\varepsilon_a}{\varepsilon_b^2(1+\beta)} < 0, \quad (6.89)$$

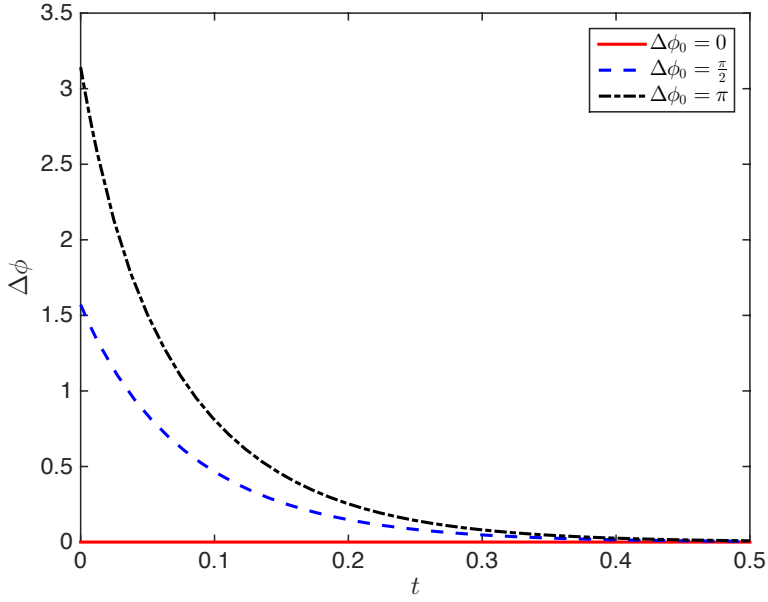


Fig. 6.5 Recovery torque model with initial phase difference of 0, $\pi/2$ and π , all the cases reach steady state that $\Delta\phi = 0$.

then $\Delta\phi = 0$ is a stable point, which leads to the conclusion that helices reach the status of synchronisation with any initial phase difference. We can plot several solutions with different initial phases in FIG. 6.5 to see. We claim that adding the recovery torque will always lead to synchronisation.

6.7 Discussion

In this chapter, using the similar idea of long-wavelength integration and separation of length scales, I have derived the leading order of non-zero torque and force induced by hydrodynamic interactions between two nearby helices. For fixed geometry, the interaction torque only depends on the phase difference between helices and reaches its maximum when the phase difference is π . This result perfectly matches previous numerical measurements [72].

In the last section, I apply the calculate results of torque and propose a simple mathematical model for synchronisation between helices. Since the elastic effect is considered indispensable during synchronisation, a recovery torque is added to balance with the hydrodynamic torque. The in-phase state is found to be the only stable state for the controlling equation, which leads to synchronisation for arbitrary initial phases.

Another result presented in this work is that the net force along y -direction, where two helices are aligned, is always zero. The similar feature is illustrated in Chapter. 5 for two rotating rods, although it is completely different physical origin. This feature of force might be able to trigger the attraction of helices, which is expected to be included to help to develop more sophisticated model for flagellar bundling.

Chapter 7

Conclusion

In this thesis, I use mathematical ways to answer two recently much-focused questions in swimming at low Reynolds number, why does the slip shown in complex fluids lead to swimming enhancement? And how does the hydrodynamic interactions affect bundling of flagellar filaments?

The answer to the first question is intuitively simple, slip can reduce friction. More specifically, the presence of the slip effect near the surface affects normal hydrodynamics weakly but leads to a reduction of tangential viscous drag, hence should always leads to a faster swimming. In order to seek for quantitative evidences for this argument, I undertake the problem by considering a classical simple model swimmer, Taylor swimming sheet, but with a Navier slip boundary condition. The speed in this two-dimensional setup can be increased by $1 + 2k\Lambda$ for the swimming with wave number k and slip length Λ . By considering more realistic three-dimensional waving cylinder and a phase-separation in fluid adjacent to surface, three more scenarios have been constructed and the speed of swimming is always increased with larger slip length or thinner slip layer. This model inspired by Taylor's swimming model claims the effect of slip a mechanism for swimming enhancement. However, to obtain a quantitative description of the problem, this model is still not realistic enough, for its constrain of small deformation and simple sinusoidal waveform assumption. Therefore a more generic slender body is considered, which is characterized by that the length L is much larger than the breadth a . The well-known slender-body theory describes the relation between the locomotion and the force on the body, and has been developed by many people in 1970's. By following the ideas of logarithmical expansions [31], and singularity construction in inner and outer region [88], I extend both Cox and Lighthill's slender-body theory with a Navier slip boundary. Furthermore the resistant coefficients can be derived

from both theories, which is approximately

$$\xi_{\parallel} = \frac{2\pi\mu}{\ln \frac{L}{a} - \frac{1}{2} + \frac{\Lambda}{a}}, \quad \xi_{\perp} = \frac{4\pi\mu}{\ln \frac{L}{a} + \frac{1}{2} + \frac{2\Lambda}{a+2\Lambda}}. \quad (7.1)$$

This result explicitly quantifies the argument that slip length raises a systematic decrease of tangential viscous drag, however has relatively weak influence in the direction perpendicular to the surface. The slip slender-body theory derived in this thesis is a very general conclusion and is expected to be applied in a wide range of contexts with physical similarities in slip, such as capillary flow [7], porous media [87], electroosmotic flow [76], etc.

The second question that addresses hydrodynamic interactions is considered more difficult since more than one filament are involved. Besides the reason of increased filaments, bundling itself is a rather complicated biological process, which is a result of combined actions of not only hydrodynamic interactions, but also elasticity and interplay between filament and head. As a result of its complexity, it is more straightforward to use numerical simulations in theoretical studies and leads to a lack of analytical model. In this thesis, I have developed an asymptotic framework to compute the hydrodynamic interactions between nearby filaments, and the key ingredient allowing the calculation to be carried out is the idea of separation of length scales. Again starting from a simple geometry of two naturally straight filaments separated by a distance h , together with another two length scales of radius a and length L , a separation in lengths $a \ll h \ll L$ has been considered. This set-up enables a representation of the flow as a superposition of fundamental singularities whose strengths vary only on long wavelengths, taking advantage of which, the flow field induced by hydrodynamic interactions can be integrated for arbitrary rotation with rate $\omega \mathbf{e}_z$ and translation, with a mathematical description of

$$\mathbf{v}_M^{(2) \rightarrow (1)} = \left(\frac{a}{h}\right)^2 \boldsymbol{\omega}^{(2)}(s) \mathbf{z} \times \mathbf{h}, \quad (7.2a)$$

$$\mathbf{v}_F^{(2) \rightarrow (1)} = \frac{1}{4\pi\mu} \ln \left[\frac{h}{L} \right] (\mathbf{I} + \mathbf{z}\mathbf{z}) \cdot \mathbf{f}^{(2)}. \quad (7.2b)$$

The viability and efficiency of separation of length scales have been further validated by a continuous study on helices. With this realistic but more complicated geometry, an additional length scale, the radius of helix b , is assumed to be small and a corresponding length separation is considered as $a \ll b \ll h \ll L$. Under this asymptotic limit, hydrodynamic torque and force have been evaluated linearly with rotation rates, and the resistance matrices are functions of only phase difference. This result makes a good agreement with previous numerical measurements, in both capturing the feature that the torque and anchoring force

reach largest magnitude when the phase difference is π . Building on the long-wavelength integrations derived for rods and helices, I have further proposed two models of flagellar bundling, which emphasizes two stages in bundling process, attraction and synchronisation, respectively. In the first the model of elastic rods, a partial differential equation governed by a dimensionless number Bu has been derived. Numerical studies have demonstrated instabilities with different Bu during both bundling and unbundling processes. In the second model of helices, the helices are not allowed to tilt but the elasticity represented by a recovery torque has been included. A simple first order ordinary differential equation has been derived and in-phase state has been discovered to be the only stable state of this governing equation. I would like to note that the length separation with $a \ll h \ll L$ or $a \ll b \ll h \ll L$ is widely existed in real biological world, as a result the framework I have constructed to develop long-wavelength hydrodynamic integrations is very general and is expected to be extended to any particular situations where two or more nearby filaments interacting through fluids, for example the conformation of cilia arrays [17] and microtubules [23].

References

- [1] (1961). *A treatise on Hydrodynamics*. Dover, New York.
- [2] (2007). *Advanced Transport Phenomena: Fluid Mechanics and Convective Transport Processes*. Cambridge, UK: Cambridge University Press.
- [3] Adhyapak, T. C. and Stark, H. (2015). Zipping and entanglement in flagellar bundle of *E. coli*: Role of motile cell body. *Phys. Rev. E*, 052701.
- [4] Alberts, B., Johnson, A., Lewis, J., Raff, M., Roberts, K., and Walter, P. (2007). *Molecular Biology of the Cell*. New York, NY: Garland Science, fifth edition edition.
- [5] Aral, B. and Kalyon, K. (1994). Effects of temperature and surface roughness on time-dependent development of wall slip in steady torsional flow of concentrated suspensions. *J. Rheol.*, 38(4):957.
- [6] B. Qian, H. J., Gagnon, D. A., Breuer, K. S., and Powers, T. R. (2009). Minimal model for synchronization induced by hydrodynamic interactions. *Phys. Rev. E*, 80.
- [7] Barnes, H. A. (1995). A review of the slip (wall depletion) of polymer solutions, emulsions and particle suspensions in viscometers: Its cause, character, and cure. *J. Non-Newtonian Fluid Mech.*, 56:221–231.
- [8] Batchelor, G. K. (1970). The stress system in a suspension of force-free particles. *J. Fluid Mech.*, 41:545–570.
- [9] Bennett, R. R. and Golestanian, R. (2013). Emergent run-and-tumble behavior in a simple model of chlamydomonas with intrinsic noise. *Phys. Rev. Lett.*, 110(148102).
- [10] Berg, H. C. (2003). The rotary motor of bacteria flagella. *Annu. Rev. Biochem.*, 72.
- [11] Berg, H. C. (2004). *E. coli in Motion*. Springer-Verlag, New York, NY.
- [12] Berg, H. C. and Anderson, R. A. (1973). Bacteria swim by rotating their flagellar filaments. *Nature*, 245:380.
- [13] Berg, H. C. and Turner, L. (1979). Movement of microorganisms in viscous environment. *Nature*, 278:349351.
- [14] Berke, A. P., Turner, L., Berg, H. C., and Lauga, E. (2008). Hydrodynamic attraction of swimming microorganisms by surfaces. *Phys. Rev. Lett.*, 101:038102.

- [15] Blake, J. R. and Sleigh, M. A. (1974). Mechanics of ciliary locomotion. *Biol. Rev. Camb. Phil. Soc.*, 49:85125.
- [16] Boal, D. (2002). *Mechanics of the cell*. Cambridge, UK: Cambridge University Press.
- [17] Bray, D. (2000). *Cell Movements*. Garland Publishing, New York, NY.
- [18] Brennen, C. and Winet, H. (1977a). Fluid mechanics of propulsion by cilia and flagella. *Ann. Rev. Fluid Mech.*, 9:339.
- [19] Brennen, C. and Winet, H. (1977b). Fluid mechanics of propulsion by cilia and flagella. *Ann. Rev. Fluid. Mech.*, 9:339.
- [20] Brown, M. T., Steel, B. C., Silverstrin, C., Wilkinson, D. A., Delalez, N. J., Lumb, C. N., Obara, B., Armitage, J. P., and Berry, R. M. (2012). Flagellar hook flexibility is essential for bundle formation in swimming escherichia coli cells. *J. Bacteriol.*, 194:3495–3501.
- [21] Brumley, D. R., Wan, K. Y., Polin, M., and Goldstein, R. E. (2014). Flagellar synchronization through direct hydrodynamic interactions. *eLife*, 3(e02750).
- [22] Calladine, C. R. (1975). Construction of bacterial flagella. *Nature*, 255.
- [23] Camalet, S., Julicher, F., and Prost, J. (1999). Self-organized beating and swimming of internally driven filaments. *Phys. Rev. Lett.*, 82(7):1590–1593.
- [24] Celli, J. P. and et al. (2009). Helicobacter pylori moves through mucus by reducing mucin viscoelasticity. *Proc. Natl. Acad. Sci.*, 106:14321–14326.
- [25] Chang, Y. C. and Keh, H. J. (2011). Theoretical study of the creeping motion of axially and fore-and-aft symmetric slip particles in an arbitrary direction. *European Journal of Mechanics B/Fluids*, 30(2):236–244.
- [26] Chang, Y. C. and Keh, H. J. (2012). Creeping-flow rotation of a slip spheroid about its axis of revolution. *Theor. Comput. Fluid Dyn.*, 26:173.
- [27] Childress, S. (1981). *Mechanics of Swimming and Flying*. Cambridge University Press, Cambridge U.K.
- [28] Chwang, A. T. and Wu, T. Y. (1971). Helical movement of micro-organisms. *Proc. Roy. Soc. Lond. B*, 178:327–346.
- [29] Cisneros, L. H., Cortez, R., Dombrowski, C., Goldstein, R. E., and Kessler, J. O. (2007). Fluid dynamics of self-propelled micro-organisms, from individuals to concentrated populations. *Exp. Fluids*, 43:737–753.
- [30] Cohen, Y. and Metzner, A. B. (1985). Apparent slip flow of polymer solutions. *J. Rheol.*, 29:67.
- [31] Cox, R. G. (1970). The motion of long slender bodies in a viscous fluid. Part 1. General theory. *J. Fluid Mech.*, 44:791–810.

- [32] Dasgupta, M., Liu, B., Fu, H. C., Berhanu, M., Breuer, K. S., Powers, T. R., and Kudrolli, A. (2013). Speed of a swimming sheet in newtonian and viscoelastic fluids. *Phys. Rev. E.*, 87:013015.
- [33] Datt, C., Zhu, L., Elfring, G., and Pak, O. (2015). Squirming through shear-thinning fluids. *J. Fluid Mech. Rapids*, 784:R1.
- [34] Di Leonardo, R., Dell'Arciprete, D., Angelani, L., and Iebba, V. (2011). Swimming with an image. *Phys. Rev. Lett.*, 106:038101.
- [35] D.Montenegro-Johnson, T., Smith, D. J., and Loghin, D. (2013). Physics of rheologically enhanced propulsion: Different strokes in generalized stokes. *Phys. Fluids*, 25(081903).
- [36] Drescher, K., Dunkel, J., Cisneros, L. H., Ganguly, S., and Goldstein, R. E. (2011). Fluid dynamics and noise in bacterial cell-cell and cell-surface scattering. *Proc. Natl. Acad. Sci. U.S.A.*, 108:10940–10945.
- [37] Elfring, G. and Goyal, G. (2016). The effect of gait on swimming in viscoelastic fluids. *J. Non-Newtonian Fluid Mech.*, 234(8-14).
- [38] Elfring, G. and Lauga, E. (2009). Hydrodynamic phase locking of swimming microorganisms. *Phys. Rev. Lett.*, 103:088101.
- [39] Espinosa-Garcia, J., Lauga, E., and Zenit, R. (2013). Fluid elasticity increases the locomotion of flexible swimmers. *Phys. Fluids*, 25:031701.
- [40] Fauci, L. J. and Dillon, R. (2006). Biofluidmechanics of reproduction. *Ann. Rev. Fluid Mech.*, 38:371.
- [41] Flores, H., Lobaton, E., Mendezdiez, S., Tlupova, S., and Cortez, R. (2005). A study of bacterial flagellar bundling. *Bull. Math. Biol.*, 67:137.
- [42] Friedrich, B. M. and Julicher, F. (2012). Flagellar synchronization independent of hydrodynamic interactions. *Phys. Rev. Lett.*, 109(138102).
- [43] Fu, H. C. and Charles W. Wolgemuth, T. R. P. (2009). Theory of swimming filaments in viscoelastic media. *Phys. Fluids*, 21:033102.
- [44] Fu, H. C., Powers, T. R., and Wolgemuth, C. W. (2007). Theory of swimming filaments in viscoelastic media. *Phys. Rev. Lett.*, 99:258101.
- [45] Gaffney, E. A., Gadêlha, H., Smith, D. J., Blake, J. R., and Kirkman-Brown, J. C. (2011). Mammalian sperm motility: observation and theory. *Annu. Rev. Fluid Mech.*, 43:501528.
- [46] Gagnon, D., Shen, X., and Arratia, P. E. (2013). Undulatory swimming in fluids with polymer networks. *Europhys. Lett.*, 104:14004.
- [47] Geer, J. (1976). Stokes flow past a slender body of revolution. *J. Fluid Mech.*, 78:577.
- [48] Giacch  , D., Ishikawa, T., and Yamaguchi, T. (2010). Hydrodynamic entrapment of bacteria swimming near a solid surface. *Phys. Rev. E*, 82:056309.

- [49] Goldman, D. I. (2014). Biophysical principles of undulatory self-propulsion in granular media. *Rev. Mod. Phys.*, 86:943.
- [50] Goldstein, R. E. (2014). *Volvox* as a model organism. *Annu. Rev. Fluid Mech.*, 47:343375.
- [51] Goldstein, R. E., Lauga, E., Pesci, A. I., and Proctor, M. R. E. (2016). Elastohydrodynamic synchronization of adjacent beating flagella. *Phys. Rev. Fluids*, 1:073201.
- [52] Golestanian, R., Yeomans, J. M., and Uchida, N. (2011). Hydrodynamic synchronization at low reynolds number. *Soft Matter*, 7:3074.
- [53] Gray, J. and Hancock, G. J. (1955). The propulsion of sea-urchin spermatozoa. *J. Exp. Biol.*, 32(802).
- [54] Guasto, J. S., Rusconi, R., and Stocker, R. (2012). Fluid mechanics of planktonic microorganisms. *Annu. Rev. Fluid Mech.*, 44:373400.
- [55] Guazzelli, E. and Morris, J. F. (2011). *A Physical Introduction to Suspension Dynamics*. Cambridge University Press.
- [56] Gueron, S., Levit-Gurevich, K., Liron, N., and Blum, J. J. (1997). Cilia internal mechanism and metachronal coordination as the result of hydrodynamical coupling. *Proc. Natl. Acad. Sci. USA*, 94(12):6001–6006.
- [57] Gueron, S. and Liron, N. (1993). Simulations of three-dimensional ciliary beats and cilia interactions. *Biophys. J.*, 65:499.
- [58] Guirao, B. and Joanny, J. F. (2007). Spontaneous creation of macroscopic flow and metachronal waves in an array of cilia. *Biophys. J.*, 92:1900.
- [59] Hancock, G. J. (1953). The self-propulsion of microscopic organisms through liquids. *Proc. R. Soc. Lond. A*, 217:96.
- [60] Hasegawa, K., Yamashita, I., and Namba, K. (1998). Quasi- and nonequivalence in the structure of bacterial flagellar filament. *Biophys. J.*, 74:569–575.
- [61] Hoshikawa, H. and kamaya, R. (1985). Elastic properties of bacterial flagellar filaments. ii. determination of the modulus of rigidity. *Biophys. Chem.*, 22:159–166.
- [62] Hu, C.-M. and Zwanzig, R. (1974). Rotational friction coefficients for spheroids with the slipping boundary condition. *J. Chem. Phys.*, 60:4354.
- [63] Ishikawa, T., Sekiya, G., Imai, Y., and Yamaguchi, T. (2007). Hydrodynamic interaction between two swimming bacteria. *Biophys. J.*, 93:2217–2225.
- [64] Janssen, P. J. A. and Graham, M. D. (2011). Coexistence of tight and loose bundled states in a model of bacterial flagellar dynamics. *Phys. Rev. E*, 84.
- [65] Johnson, R. E. (1980). An improved slender-body theory for stokes flow. *J. Fluid Mech.*, 99:411.

- [66] Kalyon, D. M. (2005). Apparent slip and viscoplasticity of concentrated suspensions. *J. Rheol.*, 49:621.
- [67] Kanehl, P. and Ishikawa, T. (2014). Fluid mechanics of swimming bacteria with multiple flagella. *Physical Review E*, 89.
- [68] Katz, D. F., Mills, R. N., and Pritchett, T. R. (1978). The movement of human spermatozoa in cervical mucus. *J. Reprod. Fert.*, 53:259265.
- [69] Keh, H. J. and Chang, Y. C. (2008). Slow motion of a slip spheroid along its axis of revolution. *International Journal of Multiphase Flow*, 34(8):713–722.
- [70] Keller, J. B. and Rubinow, S. I. (1976). Slender body theory for slow viscous flow. *J. Fluid Mech.*, 75(705-14).
- [71] Kim, M., Bird, J. C., Parys, A. J. V., K, and Powers, T. R. (2003). A macroscopic scale model of bacterial flagellar bundling. *Proc. Natl. Acad. Sci. USA*, 100:15481–15485.
- [72] Kim, M. and Powers, T. R. (2004). Hydrodynamic interactions between rotating helices. *Phys. Rev. E*, 69.
- [73] Kim, S. and Karrila, S. J. (2005). *Microhydrodynamics: Principles and Selected Applications*. Courier Corporation.
- [74] Koch, D. L. and Subramanian, G. (2011). Collective hydrodynamics of swimming microorganisms: Living fluids. *Annu. Rev. Fluid Mech.*, 43:637 – 659.
- [75] Kupper, J., Marwan, W., Typke, D., Grunberg, H., Uwer, U., Gluch, M., and Oesterhelt, D. (1994). The flagellar bundle of halobacterium salinarium is inserted into a distinct polar cap structure. *J. Bacteriol.*, 176:5184–5187.
- [76] Lauga, E. (2004). Apparent slip due to the motion of suspended particles in flows of electrolyte solutions. *Langmuir*, 20(20):8924.
- [77] Lauga, E. (2007). Propulsion in a viscoelastic fluid. *Phys. Fluids*, 19:083104.
- [78] Lauga, E. (2011). Life around the scallop theorem. *Soft Matter*, 7:3060.
- [79] Lauga, E. (2014). Locomotion in complex fluids: Integral theorems. *Phys. Fluids*, 26:081902.
- [80] Lauga, E. (2016). Bacterial hydrodynamics. *Annu. Rev. Fluid Mech.*, 48:105–130.
- [81] Lauga, E., DiLuzio, W. R., Whitesides, G. M., and Stone, H. A. (2006). Swimming in circles: Motion of bacteria near solid boundaries. *Biophys. J.*, 90:400–412.
- [82] Lauga, E. and Powers, T. R. (2009a). The hydrodynamics of swimming microorganisms. *Rep. Prog. Phys.*, 72:096601.
- [83] Lauga, E. and Powers, T. R. (2009b). The hydrodynamics of swimming microorganisms. *Rep. Prog. Phys.*, 72:096601.

- [84] Leal, L. G. (2007a). *Advanced Transport Phenomena: Fluid Mechanics and Convective Transport Processes*. Cambridge University Press, Cambridge, UK.
- [85] Leal, L. G. (2007b). *Advanced Transport Phenomena: Fluid Mechanics and Convective Transport Processes*. Cambridge University Press.
- [86] Lemelle, L., Palierne, J. F., Chatre, E., and Place, C. (2010). Counterclockwise circular motion of bacteria swimming at the air-liquid interface. *J. Bacteriol.*, 192:6307–6308.
- [87] Leshansky, A. M. (2009). Enhanced low-Reynolds-number propulsion in heterogeneous viscous environments. *Phys. Rev. E*, 80:051911.
- [88] Lighthill, J. (1975). *Mathematical Biofluidynamics*. Philadelphia: SIAM.
- [89] Lighthill, J. (1976). Flagellar hydrodynamics. *SIAM Rev.*, 18:161–230.
- [90] Lighthill, J. (1996a). Helical distributions of stokeslets. *J. Eng. Math.*, 30:35–78.
- [91] Lighthill, J. (1996b). Reinterpreting the basic theorem of flagellar hydrodynamics. *J. Eng. Math.*, 30:25–34.
- [92] Lim, S. and Peskin, C. S. (2012). Fluid-mechanical interaction of flesible baterial flagella by the immersed boundary method. *Phys. Rev. E*, 85.
- [93] Liu, B., Powers, T. R., and Breuer, K. S. (2011). Force-free swimming of a model helical flagellum in viscoelastic fluids. *Proc. Natl. Acad. Sci.*, 108(49):516520.
- [94] Lopez, D. and Lauga, E. (2014). Dynamics of swimming bacteria at complex interfaces. *Phys. Fluids*, 26:071902.
- [95] Macnab, R. M. (1977). Bacterial flagella rotating in bundles: A study in helical geometry. *Proc. Natl. Acad. Sci. USA*, 74:221–225.
- [96] Macnab, R. M. and Han, D. P. (1983). Asynchronous switching of flagellar motors on a single bacterial cell. *Cell*, 32:109–117.
- [97] Magariyama, Y. and Kudo, S. (2002). A mathematical explanation of an increase in bacterial swimming speed with viscosity in linear polymer solutions. *Biophys. J.*, 83:733–739.
- [98] Man, Y., Koens, L., and Lauga, E. (2016). Hydrodynamic interactions between nearby slender filaments. *Europhys. Lett.*, 116:24002.
- [99] Man, Y. and Lauga, E. (2015). Phase-separation models for swimming enhancement in complex fluids. *Phys. Rev. E*, 92(023004).
- [100] Marcos, Fu, H. C., Powers, T. R., and Stocker, R. (2012). Bacterial rheotaxis. *Proc. Natl. Acad. Sci. U.S.A.*, 109:4780–4785.
- [101] Mhetar, V. and Archer, L. A. (1998). Slip in entangled polymer solutions. *Macromolecules*, 31(19):6639–6649.

- [102] Navier, C.-L. (1823). Mémoire sur les lois du mouvement des fluides. *Mémoires de l'Académie Royale des Sciences de l'Institut de France*, VI:389440.
- [103] Niedernayer, T., Eckhardt, B., and Lenz, P. (2008). Synchronization, phase locking, and metachronal wave formation in ciliary chains. *Chaos*, 18(037128).
- [104] Oberbeck, A. J. (1876). Über stationäre fliissigkeitsbewegungen mit berücksichtigung der inneren reibung. *J. Reine Angew. Math.*, 81(62).
- [105] Peng, Z., Pak, O., and Elfring, G. E. (2016). Characteristics of undulatory locomotion in granular media. *Phys. Fluids*, 28(031901).
- [106] Powers, T. R. (2002). Role of body rotation in bacterial flagellar bundling. *Phys. Rev. E*, 65.
- [107] Powers, T. R. (2010). Dynamics of filaments and membranes in a viscous fluid. *Rev. Mod. Phys.*, 82:1607.
- [108] Purcell, E. M. (1977). Life at Low Reynolds Number. *Am. J. Phys.*, 45:3.
- [109] Reichert, M. and Stark, H. (2005). Synchronization of rotating helices by hydrodynamic interactions. *Eur. Phys. J. E*, 17:493–500.
- [110] Reigh, S. Y., Winkler, R. G., and Gompper, G. (2012a). Synchronization and bundling of anchored bacterial flagella. *Soft Matter*, 8:4363–4372.
- [111] Reigh, S. Y., Winkler, R. G., and Gompper, G. (2012b). Synchronization and bundling of anchored bacterial flagella. *Soft Matter*, 8:4363.
- [112] Reigh, S. Y., Winkler, R. G., and Gompper, G. (2013). synchronization, slippage and unbundling of driven helical flagella. *PLOS One*, 8.
- [113] Reynolds, A. J. (1965). The swimming of minute organisms. *J. Fluid Mech.*, 23:241–260.
- [114] Riley, E. E. and Lauga, E. (2014). Enhanced active swimming in viscoelastic fluids. *Europhys. Lett.*, 108:34003.
- [115] Rusconi, R., Guasto, J. S., and Stocker, R. (2014). Bacterial transport suppressed by fluid shear. *Nature Phys.*, 10:212–217.
- [116] Shen, X. N. and Arratia, P. E. (2011). Undulatory swimming in viscoelastic fluids. *Phys. Rev. Lett.*, 106:208101.
- [117] Sherwood, J. D. (2012). Resistance coefficients for stokes flow around a disk with a navier slip condition. *Phys. Fluids*, 24(093103).
- [118] Sleigh, M. A., Blake, J. R., and Liron, N. (1988). The propulsion of mucus by cilia. *Am. Rev. Respir. Dis.*, 137(16):726.
- [119] Sochi, T. (2011). Slip at fluid-solid interface. *Polymer Review*, 51:309344.

- [120] Sokolov, A. and Aranson, I. S. (2009). Reduction of viscosity in suspension of swimming bacteria. *Phys. Rev. Lett.*, 103:148101.
- [121] Sokolov, A. and Aranson, I. S. (2012). Physical properties of collective motion in suspensions of bacteria. *Phys. Rev. Lett.*, 109:248109.
- [122] Soltani, F. and Yilmazer, U. (1998). Slip velocity and slip layer thickness in flow of concentrated suspensions. *J. App. Polym. Sci.*, 70:515–522.
- [123] Spagnolie, S. E. and Lauga, E. (2011). Comparative hydrodynamics of bacterial polymorphism. *Phys. Rev. Lett.*, 106:58103.
- [124] Spagnolie, S. E. and Lauga, E. (2012). Hydrodynamics of self-propulsion near a boundary: predictions and accuracy of far-field approximations. *J. Fluid Mech.*, 700:105–147.
- [125] Spagnolie, S. E., Liu, B., and Powers, T. R. (2013). Locomotion of helical bodies in viscoelastic fluids: Enhanced swimming locomotion of helical bodies in viscoelastic fluids: Enhanced swimming at large helical amplitudes. *Phys. Rev. Lett.*, 111:068101.
- [126] Stokes, G. G. (1851). On the effect of the internal friction of fluids on the motion of pendulums. *Trans. Camb. Phil. Soc.*, 9:182–187.
- [127] Taylor, G. I. (1951). Analysis of the Swimming of Microscopic Organisms. *Proc. R. Soc. London Ser. A*, 209:447.
- [128] Taylor, G. I. (1952). The action of waving cylindrical tails in propelling microscopic organism. *Proc. R. Soc. Lond. A*, 211:225239.
- [129] Teran, J., Fauci, L., and Shelley, M. (2010). Viscoelastic fluid response can increase the speed and efficiency of a free swimmer. *Phys. Rev. Lett.*, 104:038101.
- [130] Thomases, B. and Guy, R. D. (2014). Mechanisms of elastic enhancement and hindrance for finite-length undulatory swimmers in viscoelastic fluids. *Phys. Rev. Lett.*, 113:098102.
- [131] Tillett, J. P. K. (1970). Axial and transverse stokes flow past slender asixymmetric bodies. *J. Fluid Mech.*, 44(401-17).
- [132] Tornberg, A. K. and Shelley, M. J. (2004). Simulating the dynamics and interactions of flexible fibers in stokes flows. *J. Comput. Phys.*, 196(8).
- [133] Turner, L., Ryu, W. S., and Berg, H. C. (2000). Real-time imaging of fluorescent flagellar filaments. *J. Bacteriol.*, 182:2793–2801.
- [134] Uchida, N. and Golestanian, R. (2010). Synchronization and collective dynamics in a carpet of microfluidic rotors. *Phys. Rev. Lett.*, 104(178103).
- [135] Vilfan, A. and Julicher, F. (2006). Hydrodynamic flow patterns and synchronization of beating cilia. *Phys. Rev. Lett.*, 96(058102).
- [136] Watari, N. and Larson, R. G. (2010). The hydrodynamics of a run and tumble bacterium propelled by polymorphic helical flagella. *Biophys. J.*, 98:12–17.

- [137] Wiggins, C. H. and Goldstein, R. E. (1998). Flexive and propulsive dynamics of elastica at low Reynolds number. *Phys. Rev. Lett.*, 80:3879–3882.
- [138] Wolgemuth, C. W., Powers, T. R., and Goldstein, R. E. (2000). Twirling and whirling: Viscous dynamics of rotating elastic filaments. *Phys. Rev. Lett.*, 84.
- [139] Yang, X., Dillon, R. H., and Fauci, L. J. (2008). An integrative computational model of multiciliary beating. *Bull. Math. Biol.*, 70:1192.
- [140] Yang, Y., Marceau, V., and Gompper, G. (2010). Swarm behavior of self-propelled rods and swimming flagella. *Phys. Rev. E*, 82(031904).
- [141] Yilmazer, U. and Kalyon, D. (1991). Dilatancy of concentrated suspensions with newtonian matrices. *Polym. Comp.*, 12:226232.
- [142] Youngren, G. K. and Acrivos, A. (1975). Rotational friction coefficients for ellipsoids and chemical molecules with the slip boundary condition. *J. Chem. Phys.*, 63:3846.
- [143] Zhou, S., Sokolov, S., Lavrentovich, O. D., and Aranson, I. S. (2014). Living liquid crystals. *Proc. Natl. Acad. Sci. U.S.A.*, 111:1265–1270.

